TECHNISCHE UNIVERSITÄT MÜNCHEN

Lehrstuhl für Hochfrequenztechnik

Systematic Topological Design of Metamaterials: Scalar and Vectorial 3D Metamaterials and their Realisation

Michael Zedler

Vollständiger Abdruck der von der Fakultät für Elektrotechnik und Informationstechnik der Technischen Universität München zur Erlangung des akademischen Grades eines

Doktor-Ingenieurs (Dr.-Ing.)

genehmigten Dissertation.

Vorsitzender: Univ.-Prof. P. Lugli, Ph. D.
Prüfer der Dissertation: 1. Univ.-Prof. Dr. P. Russer
                          2. Prof. Dr. W. J. R. Hoefer, em.
                             University of Victoria / Kanada

Kurzfassung

Metamaterialien sind Verbundwerkstoffe, die in der Natur nicht vorkommende elektromagnetische Eigenschaften aufweisen. Darauf basierende neuartige Antennen, Koppler, Abbildungssysteme und Methoden zur Minimierung des Radarrückstreuquerschnitts wurden in der Literatur vorgeschlagen. In dieser Arbeit wird ein systematischer Ansatz zur Synthese von Metamaterialien vorgestellt. Dieser beruht darauf, dass Metamaterialien aus Einheitszellen bestehen, die klein im Verhältnis zur Wellenlänge sind. Die Topologie der Netzwerkbeschreibung einer Einheitszelle lässt sich aus Diskretisierungsschemata des ein-, zwei-, bzw. dreidimensionalen Raums ableiten. Mit dieser Methodik werden zwei isotrope dreidimensionale Metamaterialien entworfen, für die maximal-symmetrische und planare physikalische Realisierungen vorgestellt und durch Vollwellensimulationen bzw. Experimente verifiziert werden.

Abstract

Metamaterials are compound materials exhibiting electromagnetic properties not readily found in nature. Novel antennas, couplers, imaging systems and methods for the reduction of the radar cross-section based on these properties have been proposed in literature. In this thesis a systematic synthesis technique for metamaterials is presented. The foundation of this approach is that metamaterials consist of unit cells that are small compared to the wavelength. The topology of the unit cell's network representation can be derived from space-discretising schemes in 1D, 2D, and 3D. Using this technique two novel isotropic 3D metamaterials are synthesised. Maximally-symmetric and planar physical realisations are proposed and verified by full-wave simulation and experiment, respectively.

Danksagung

Diese Arbeit entstand während meiner Tätigkeit als wissenschaftlicher Mitarbeiter am Lehrstuhl für Hochfrequenztechnik der Technischen Universität München. Mein erster Dank gilt Prof. Dr. Peter Russer, der mir die Anfertigung dieser Arbeit ermöglichte und mich mit dieser an der Schnittstelle zwischen Elektrotechnik und Physik beheimateten Themenstellung betraute. Seine Impulse sowie die Ermöglichung eines Forschungsaufenthalts in Montréal, Kanada, waren für meine Arbeit ein großer Gewinn. Prof. Dr. Christophe Caloz gilt mein Dank für die viermonatige Aufnahme an seinem Lehrstuhl und der daraus entstandenen fruchtbaren Zusammenarbeit, insbesondere der ersten Prototypenfertigung der RTLM Metamaterialzelle. Prof. Dr. Wolfgang J. R. Hoefer danke ich für Einblicke in seine unveröffentlichten Arbeiten auf dem Gebiet der Expanded-Node-TLM Metamaterialien. Prof. Dr. Karl F. Warnick danke ich für die Erklärung einiger moderner Ansätze bei Integralgleichungsmethoden. Prof. Dr. Christophe Craeye danke ich für die Erlaubnis, sein Method-of-Moment Programm benutzen zu dürfen. Wertvollen Denkanstöße zur Verallgemeinerung der topologischen Betrachtung von Metamaterialien verdanke ich Prof. Dr. Igor Tsukerman.

Bei meinen Kollegen am Lehrstuhl möchte ich mich für ihre stete Hilfsbereitschaft bedanken. Besonders hervorheben möchte ich Dr. Uwe Siart für viele produktive Diskussionen und wertvoller Literaturhinweise, sowie Dr. Robert Wanner für Hilfestellungen bei Fragen der Schaltungstechnik und seine kompetente Einführung in alpine Aktivitäten. Pascal Hofmann danke ich für die Vielzahl fachlicher Telefonate, die vorerst zu einer gemeinsamen Veröffentlichung geführt haben. Diese Arbeit haben Dr. Axel Reichert und Pascal Hofmann in Windeseile akribisch korrekturgelesen und durch ihre Anmerkungen die Lesbarkeit deutlich verbessert.

Zu guter Letzt gebührt herzlicher Dank meinen Eltern. Beide haben mich fortwährend unterstützt, ich konnte immer auf sie zählen. Sie gaben mir Neugier, ein analytisches Grundgerüst und Standfestigkeit mit auf den Weg.

Contents

1 Introduction

Many breakthroughs in technology are related to newly available materials; from the Stone Age to Iron Age, from bronze and concrete to today's composite materials. Here, the discovery, understanding and *synthesis* of new materials with respect to *mechanical* properties led to new eras.

Within this decade some well known phenomena, observed for wave propagation in periodic structures and analysed since the early 1950s [Brillouin, 1953, Felsen and Marcuvitz, 1994, Munk, 2000], were interpreted as a means to the synthesis of *electromagnetic* properties like dispersion. These materials, at that time termed 'photonic bandgap material' and 'photonic crystal', are nowadays called *electromagnetic bandgap structures*.

Starting in the beginning of the 2000s, the idea of synthesising the electromagnetic behaviour of materials was extended to *metamaterials*, seizing a hypothesis published in [Mandelshtam, 1947] and [Veselago, 1968] about wave propagation in media with negative relative permittivity ϵ_r and permeability μ_r: In this case the electric field E, the magnetic field H, and the wave vector k form a left-handed trihedron, as opposed to the right-handed trihedron for normal materials. Terminology of this research branch is not settled yet, an overview of suggested terms can be found in the next section 2.1.

Metamaterial structures synthesising arbitrary *effective material properties* were invented, possible applications in the field of communication and sensing system were proposed, and, some of them, already experimentally verified. The great potential of these metamaterials is primarily due to the control of the amplitudes, frequencies and wavenumbers of propagating and evanescent electromagnetic modes, which is not possible with normal materials.

In this thesis a systematic approach to the synthesis of metamaterials is presented. Group theory cannot be used for the synthesis of metamaterials, as it solely adresses the level of symmetry of a structure, but it does not determine the structure's constituents. This information can be obtained from *topological analysis*: A metamaterial is composed of cells that are small compared to the wavelength which are usually periodically continued. In general, any structure of arbitrary electrical size can be represented by a network, hence also a metamaterial unit cell.

It will be shown that the topologies of network representations of metamaterials can be derived from discretisations of one-, two-, and three-dimensional space. While space-discretising numerical schemes *approximate* space by using discrete cells that are small compared to the wavelength, metamaterials *physically realise* space with special properties using cells that are small compared to the wavelength. With the network topology thus being determined the network elements are chosen such that the desired dispersion of the metamaterial is obtained. Physical realisations of the metamaterial network description can be designed by considering symmetry of the sought unit cell and fabrication technology requirements.

By applying this systematic approach, on one hand metamaterials presented in literature are compactly explained. On the other hand two novel three-dimensional metamaterials are synthesised. Maximally-symmetric and planar physical realisations are proposed, analysed and verified by full-wave simulation and experiment, respectively. The organisation of this thesis is as follows:

Chapter 2 gives the fundamentals of the field of metamaterials. Terminology is defined and wave propagation in the presence of media with unusual effective material parameters, i. e., metamaterials, is discussed. Effects due to metamaterials and applications based upon these effects are presented. A selection of publications on this field of research concludes this chapter.

Chapter 3 presents the topological description of metamaterials, yielding a framework for the systematic design of metamaterials. This framework is applied to several structures presented in literature. This approach was first published in [Zedler et al., 2008b].

Within this derivation several concepts common to the analysis of periodic structures are extensively used. Appendix A contains an introduction to these theoretical prerequisites. This includes the formulation as an eigenvalue problem, the concepts of the Brillouin zone, dispersion diagrams, structure functions, and algebraic analysis approaches.

Chapter 4 discusses two-dimensional metamaterial structures using the topological description presented in Chapter 3. Topologies are derived from symmetry, effectively yielding structures well-known in computational electromagnetics, namely the 2D transmission line matrix method (TLM).

Chapter 5 presents a three-dimensional metamaterial that supports one polarisation which is derived using the topological analysis of Chapter 3. It has a highly symmetric physical realisation which therefore enables isotropic metamaterial behaviour. Full-wave simulations verify the topological considerations. This metamaterial was first published in [Zedler et al., 2008a].

Chapter 6 discusses an isotropic three-dimensional metamaterial structure that supports two polarisations. Like in the preceding chapters it is also derived from a topological point of view. Essentially, the computational method 'symmetric condensed node' TLM (SCN-TLM) and its variant, the rotated TLM method (RTLM) are re-derived by using symmetry inspection. A metamaterial is deduced from the RTLM discretisation of space and its electromagnetic behaviour studied using algebraic analysis, circuit simulation, full-wave simulation and measurements. This RTLM metamaterial was first published in [Zedler and Russer, 2006].

Chapter 7 treats fabrication aspects of three-dimensional metamaterials. Maximally symmetric physical realisations of unit cell topologies can be decomposed into polyhedra [Zedler and Russer, 2008] allowing for mass production with techniques like, e. g., injection moulding. Alternatively, it is possible to physically realise 3D unit cell topologies with planar fabrication techniques common in microwave engineering. Planarisations of the metamaterials presented in chapters 5 and 6 are discussed.

Chapter 8 summarises the present thesis and gives an outlook to future directions of research based on topological structure descriptions.

The nomenclature used in this thesis is as follows: *Scalars* and *vectors* are denoted by italic letters. Both are either distinguishable from the context or otherwise defined in the text. *Matrices* are written in bold upright letters. All quantities are complex by default.

2 Fundamentals of Metamaterials

2.1 Definition and Terminology

Both electromagnetic bandgap structures as well as metamaterials are compound structures that aim for modifying electromagnetic wave propagation. The former can be considered a standing wave phenomenon where attention is directed to diffraction and to the question *if* a wave is able to propagate through the periodic structure. This results in typical unit cell sizes of half a guided wavelength for the synthesised material to exhibit the sought properties – the unit cell is *electrically large*.

Metamaterials, on the other hand, do not require a periodic arrangement, periodicity merely simplifies synthesis and analysis. The unit cell of a metamaterial is *electrically small*, hence electromagnetic waves probe a uniform, homogeneous environment, a compound material, which can be described by *effective material properties*. This difference was summarised in [Caloz and Itoh, 2006] as

> *[Diffraction/Scattering] properties of photonic crystals are essentially determined by the lattice, while the (refractive) properties of metamaterials are determined by the nature of the unit cell.*

The effective material properties of a metamaterial are the effective relative permeability $\mu_{\text{eff}}(\omega)$ and the effective relative permittivity $\epsilon_{\text{eff}}(\omega)$. Depending on the combination of signs of $\epsilon_{\text{eff}}(\omega)$ and $\mu_{\text{eff}}(\omega)$ at a certain angular frequency ω, waves propagate or are evanescent as shown in Fig. 2.1: The first and third quadrants allow for wave propagation, with the first quadrant being the common case of positive permeabilities and positive permittivities, which results in the positive refractive index $n = \sqrt{\mu_{\text{eff}} \cdot \epsilon_{\text{eff}}}$ and positive characteristic wave impedance $Z_F = Z_{F0}\sqrt{\mu_{\text{eff}}/\epsilon_{\text{eff}}}$. The second and fourth quadrant describe evanescent waves, with both the refractive index and the characteristic wave impedance being imaginary. The second quadrant is well known from wave propagation within plasmas, including metal below the plasmon resonance.

The third quadrant is the combination of negative permeability and negative permittivity, allowing for propagating waves. In this case E, H, and k form a
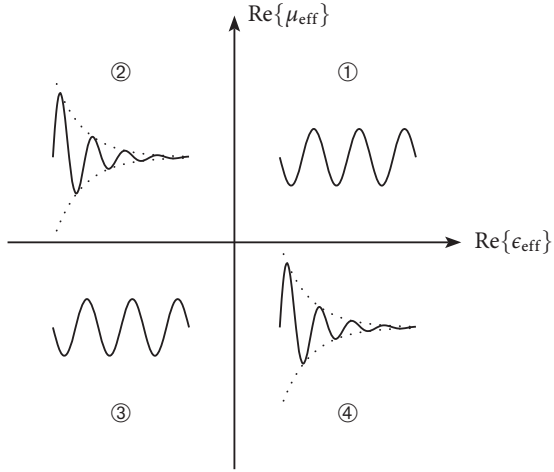
Figure 2.1: Description of propagation in metamaterials using positive and negative permittivity ϵ_{eff} and permeability μ_{eff}.

left-handed trihedron, group velocity and phase velocity are anti-parallel, the effective refractive index is *negative*, $n = -\sqrt{\mu_{\text{eff}} \cdot \epsilon_{\text{eff}}}$, and the characteristic wave impedance positive, $Z_F = Z_{F0}\sqrt{\mu_{\text{eff}}/\epsilon_{\text{eff}}}$ [Ziolkowski and Heyman, 2001]. Terminology for structures operating in this third quadrant is not settled yet, a selection of terms is

Left-handed (LH) Due to the property that the electric field, the magnetic field, and the phase velocity form a left-handed trihedron

Double negative (DNG) Due to the negative permittivity and permeability

Negative refractive index (NRI) Due to the resulting negative refractive index

Backward wave material Due to the anti-parallel phase velocity and group velocity

Veselago medium In honour of Victor Veselago whose article [Veselago, 1968] first considered what effects could be achieved with such effective material properties

Artificial dielectric Due to the compound nature of metamaterials

In this work the terminology *left-handed* will be used. A wealth of applications have been proposed in literature, a selection is listed in Sect. 2.9. While a combination of effective material parameters described by the first and third quadrant in Fig. 2.1 permits wave propagation, this picture solely gives information on the *sign* of the negative refractive index. In addition to the sign, the magnitude of the refractive index is of interest, too. Particularly values $0 \leq n < 1$ and $|n| \ll 1$ are useful both for antenna applications as well as for so-called geometry transformation structures, see Sect. 2.8. These metamaterials are referred to in literature by several authors as *μ near zero, ϵ near zero* metamaterials.

2.2 Dispersion

The description of metamaterials using effective permeabilities and permittivities requires *dispersion* in order for the structure to fulfill causality [Landau et al., 1984, Caloz and Itoh, 2006, Eleftheriades and Balmain, 2005, Engheta and Ziolkowski, 2006]. This can be seen by examining the energy density function $\bar{W}$

$$\bar{W} = \frac{1}{4}\left(\frac{\mathrm{d}(\omega\epsilon_0\epsilon_{\text{eff}})}{\mathrm{d}\omega}\bar{E}^2 + \frac{\mathrm{d}(\omega\epsilon_0\epsilon_{\text{eff}})}{\mathrm{d}\omega}\bar{H}^2\right) \tag{2.1}$$

which needs to be greater than zero independently for the electric field E and magnetic field H. Therefore

$$\frac{\mathrm{d}}{\mathrm{d}\omega}\omega\epsilon_{\text{eff}} > 0 \qquad\qquad \frac{\mathrm{d}}{\mathrm{d}\omega}\omega\mu_{\text{eff}} > 0 \tag{2.2}$$

both need to be fulfilled, implying that negative material properties require dispersion. Chapter 3 gives a systematic study of metamaterials and their dispersion properties. Using this approach physical behaviour is ensured, including the causality aspect.

2.3 Boundary Conditions, Fermat's Principle

Left-handed metamaterials reverse several laws in physics that are to be examined in this section. Two effects that experience this reversal are the reversed Doppler effect and reversed Vavilov-Čerencov radiation. These are not discussed here further, instead the reader is referred to, e. g., [Caloz and Itoh, 2006, Engheta and Ziolkowski, 2006, Eleftheriades and Balmain, 2005].

This section presents effects that can be considered being due to boundary conditions to Maxwell's equations. The tangential boundary conditions for the electric field E and the magnetic field H are

$$E_{\text{tan}}^{(2)} - E_{\text{tan}}^{(1)} = \quad - j\omega M_{m,A} \tag{2.3a}$$

$$H_{\text{tan}}^{(2)} - H_{\text{tan}}^{(1)} = J_A = - j\omega M_{e,A} \tag{2.3b}$$

with the superscript denoting the field in the respective medium and the subscript denoting tangential components. J_A is a surface current, $M_{e,A}$ and $M_{m,A}$ are electric and magnetic surface polarisations, respectively. The normal boundary conditions of the electric flux density D and the magnetic flux density B are

$$D_n^{(2)} - D_n^{(1)} = \rho_A \tag{2.3c}$$

$$B_n^{(2)} - B_n^{(1)} = 0 \tag{2.3d}$$

with the subscript n denoting the normal components, and ρ_A being a surface charge density.

The occurrence of a negative refractive index in the light of Fermat's principle used to cause confusion among the metamaterial community in the beginning of this field of research. Fermat's principle [Born et al., 1999] in its original variational formulation states that the path taken by rays of light *minimises* the integral

$$\int n(s) \, \mathrm{d}s \tag{2.4}$$

This formulation obviously fails for $n < 0$. In [Schurig and Smith, 2004] an extension to Fermat's principle valid for arbitrary n is derived: In the case of a system containing materials with negative index of refraction the functional of (2.4) needs to be *extremal*, i.e., either minimal or maximal. It thus becomes

$$\delta \int n(s) \, \mathrm{d}s = 0 \qquad \text{with } n = \begin{cases} +\sqrt{\mu_{\text{eff}} \cdot \epsilon_{\text{eff}}} & \mu_{\text{eff}}, \epsilon_{\text{eff}} \geq 0 \\ -\sqrt{\mu_{\text{eff}} \cdot \epsilon_{\text{eff}}} & \mu_{\text{eff}}, \epsilon_{\text{eff}} \leq 0 \end{cases} \tag{2.5}$$

It shall further be noted that also in the metamaterial case the variational formulation of Fermat's principle based on *time* still needs to find minimal values.

2.4 Reversed Snell's Law

Using the tangential boundary conditions of (2.3) let us consider a plane wave incident on an interface between two media, which is situated at $z = 0$. This
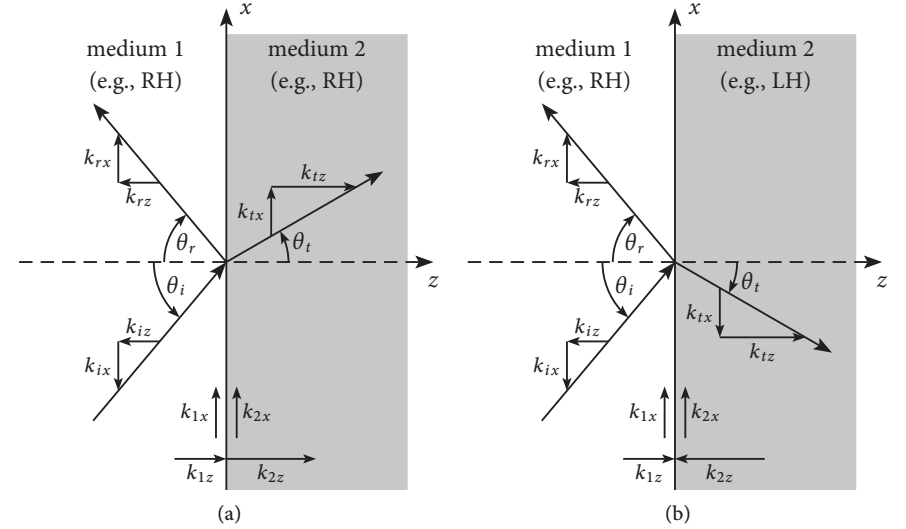
Figure 2.2: Reflection and refraction of plane waves at the interface between two media. (a) the refractive index of both media has the same sign, i.e., $n_1/n_2 > 0$ (b) interface between a right-handed and left-handed medium, i.e., $n_1/n_2 < 0$.

two-dimensional problem is shown in Fig. 2.2, with the angle of incidence $\theta_i = \arctan \frac{k_{1x}}{k_{1z}}$. The boundary condition (2.3a) reads

$$E_{i,\text{tan}} \, e^{-jk_{ix}x} + E_{r,\text{tan}} \, e^{-jk_{rx}x} = E_{t,\text{tan}} \, e^{-jk_{tx}x} \tag{2.6}$$

with the subscript i denoting the incident wave, r the reflected wave, and t the transmitted wave. This can be only fulfilled for all x if

$$k_{ix} = k_{rx} = k_{tx} \tag{2.7}$$

This is known as the *phase matching condition*. Assuming isotropic materials this results with

$$k_{1x} = k_1 \sin \theta_i \qquad\qquad k_{2x} = k_2 \sin \theta_t \tag{2.8}$$

in

$$\theta_i = \theta_r \qquad\qquad k_1 \sin \theta_i = k_2 \sin \theta_t \tag{2.9}$$

Using $k_i = n_i k_0$ this yields *Snell's law*

$$n_1 \sin \theta_i = n_2 \sin \theta_t \tag{2.10}$$

In the derivation of Snell's law no assumptions on the signs of the refractive indices of either medium was made. For this reason it describes apart from the well-known case of ordinary refraction $n_1/n_2 > 0$ as depicted in Fig. 2.2(a) also the case $n_1/n_2 < 0$. This yields the case of *negative refraction* as shown in Fig. 2.2(b).

As the sign of the *ratio* of the refractive indices determines if ordinary or negative refraction occurs, one can conclude that only the interface between a right-handed and a left-handed material yields special behaviour.

In the case of anisotropic materials the phase matching condition still holds as it is a direct consequence of the boundary conditions. What changes, though, is the angle of the transmitted wave. Assuming medium 1 to be isotropic and medium 2 to be anisotropic it can be computed using

$$k_1 \sin \theta_i = k_{2x} \tag{2.11}$$

and, following the derivation in [Ishimaru, 1991], by setting the determinant of

$$\begin{pmatrix} k_{2x} \\ 0 \\ k_{2z} \end{pmatrix} \cdot \begin{pmatrix} k_{2x} & 0 & k_{2z} \end{pmatrix} - (k_{2x}^2 + k_{2z}^2) \cdot \begin{pmatrix} 1 & 0 & 0 \\ 0 & 1 & 0 \\ 0 & 0 & 1 \end{pmatrix} + k_0^2 \boldsymbol{\mu_r \epsilon_r} \tag{2.12}$$

to zero. Here $\boldsymbol{\mu_r}$ and $\boldsymbol{\epsilon_r}$ denote the permeability and permittivity tensors, respectively. Eq. (2.11) determines k_{2x}, (2.12) relates k_{2z} to k_{2x}. Then the angle of transmission is given by

$$\tan \theta_t = \frac{k_{2x}}{k_{2z}} \tag{2.13}$$

2.5 Planar Lens

Two interfaces between right-handed and left-handed materials form a metamaterial slab and can be considered a lens [Veselago, 1968] as shown in Fig. 2.3. A point source is focussed twice, with one focus point inside the metamaterial slab and one outside. The two focal points are

$$f_1 = s_1 \frac{\tan \theta_R}{\tan |\theta_L|} \qquad\qquad f_2 = d - s_1 \tag{2.14}$$
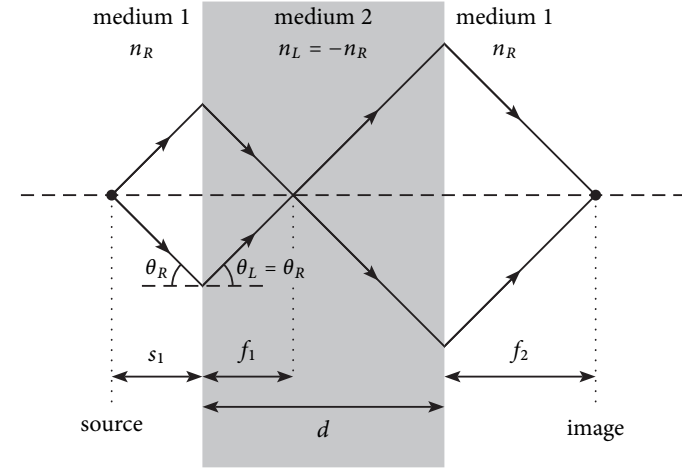
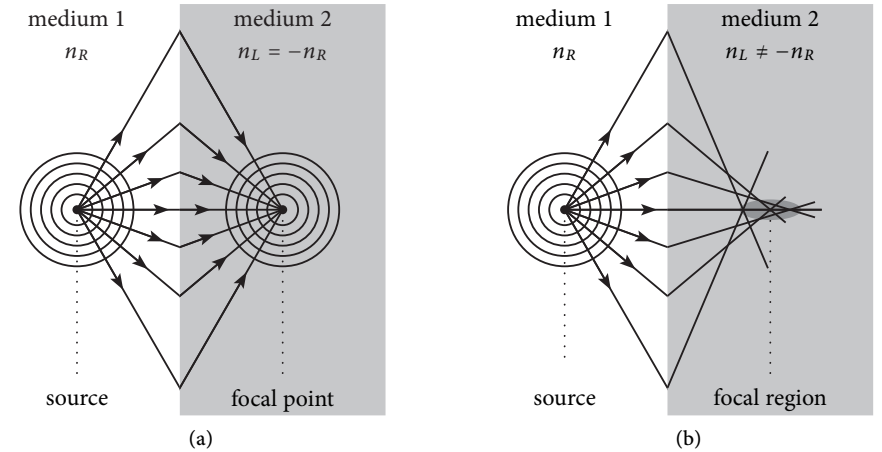Figure 2.3: Planar metamaterial lens focussing a point source inside and outside the slab.

Figure 2.4: Aberrations due to unmatched phase velocities: (a) a pure focal point for $n_L = -n_R$ and (b) a focal region for $n_L \neq -n_R$.
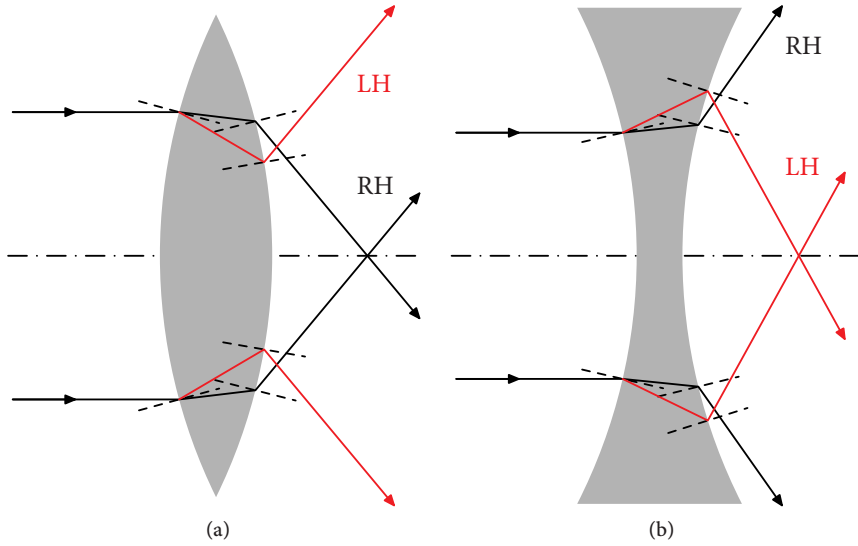
Figure 2.5: Reversal of lens behaviour. Red line: left-handed material with $n = -1$, black line: right-handed material with $n = 1.8$. Normal vectors to the surface denoted by dashed lines.

This means that for rays incident from infinity the focus is also at infinity. For this reason the structure is not a lens in the usual sense of the word, since it will not focus a bundle of rays coming from infinity at a point.

One of the advantages of this type of lens is that it is planar and thus there is no optical axis and no spherical aberration. On the other hand a new type of aberrations exists in case the metamaterial slab phase velocity is not matched, i. e., $n_L \neq -n_R$ as shown in Fig. 2.4.

In order to focus rays incident from infinity one has to resort to a curved surface [Engheta and Ziolkowski, 2006]. As shown in Fig. 2.5, a lens made of a metamaterial the convex and concave lenses have 'changed places', since the convex lens has a diverging effect and the concave lens a converging effect [Veselago, 1968]. Curved metamaterial lens behaviour for Gaussian beams are treated in detail in [Eleftheriades and Balmain, 2005], including an analysis of magnification, multiple surface behaviour, as well as with respect to aberrations: coma, spherical aberrations, astigmatism, field curvature and distortion.
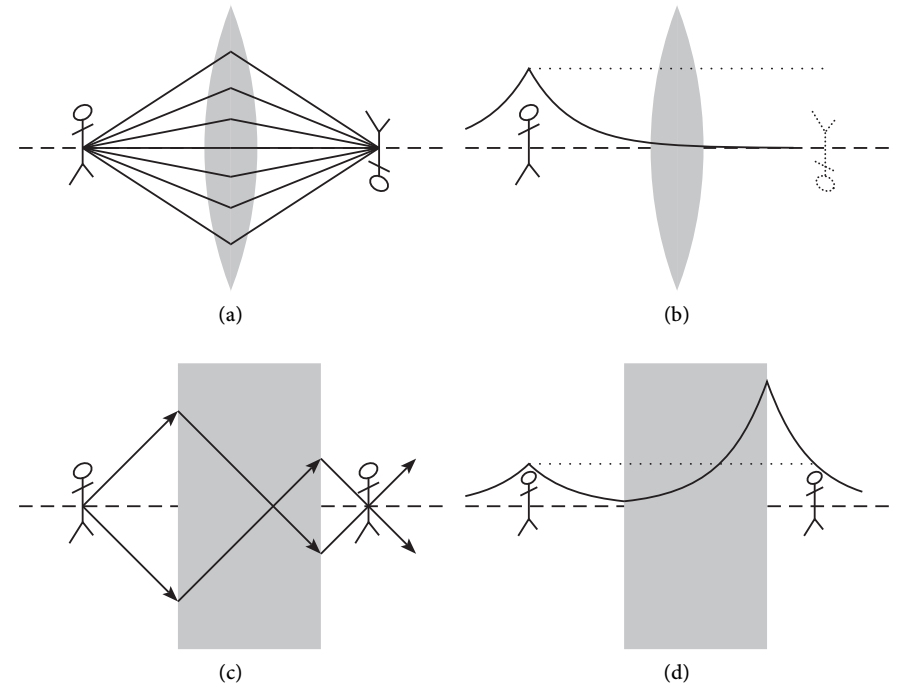
Figure 2.6: Principle of super-resolution: (a) propagating waves are imaged by the lens while (b) the evanescent wave vector spectrum is not, leading to finite resolution. Imaging of a planar lens for the (c) propagating wave vector spectrum and (d) evanescent wave vector spectrum. The latter is the cause of the super-resolution phenomenon.

2.6 Super-Resolution of Planar Lenses

The resolution of common lenses is bound by the maximum transverse wave number $k_{x,\mathrm{max}}$ contributing to the image, and according to Fourier optics one obtains for the minimum feature size

$$\Delta x \propto \frac{2\pi}{k_{x,\mathrm{max}}} = \lambda_{\mathrm{min}} \tag{2.15}$$

In addition the resolution can be limited due to diffraction at the aperture, which means that not all *propagating* wave numbers are captured by the lens. In this

case the optimum resolution is determined by the diameter of the first Airy disc [Born et al., 1999]: the Fraunhofer diffraction pattern, i. e., the far-field of a circular aperture with homogeneous field distribution of radius a is given by

$$E(\theta) \propto \frac{J_1(ka \sin\theta)}{ka \sin\theta} \tag{2.16}$$

where $J_1(x)$ denotes the Bessel function of the first kind and order one. The first minimum of $|E|^2$ yields the imaging resolution

$$\sin\theta = \frac{3.832}{ka} = 1.22\frac{\lambda}{2a} \tag{2.17}$$

As stated above, the resolution is limited by both (2.15) and (2.17). For this reason one can not obtain infinite resolution for $a \to \infty$, the hard resolution limit for a conventional lens is determined by (2.15).

While a planar lens was already proposed in [Veselago, 1968], it was shown much later in [Pendry, 2000] that a planar metamaterial lens can overcome the resolution limit of (2.15): An ideal metamaterial slab with $n_L = -n_R$ amplifies the evanescent wave vector spectrum within the slab in a resonant manner, so that also the near-field of the source is reconstructed in the imaging plane. The reconstruction of both the near-field and the far-field of the source leads to an infinitesimal focus region, that is, a focus *point* is obtained as the solution to the Helmholtz wave equation, as shown in Fig. 2.6.

This *perfect lens* or super-resolution phenomenon has stirred very high interest among physicists and engineers, both in light of possible imaging applications as well as with respect to correctly interpreting the phenomenon of amplification of the evanescent wave number spectrum and resolution limiting effects.

A concise interpretation of the super-resolution phenomenon was given in [Tretyakov, 2003] and shall be repeated here:

> *It is interesting that for the amplification of evanescent modes it is not critical that the medium inside the slab be a backward-wave medium in the sense that the evanescent modes decay in this medium in exactly the same way as in a usual material. What is critical is that the two interfaces are resonant and support surface waves with large wavenumbers. If it would be possible to realize such surfaces by other means, at least for one or several fixed wavenumbers, the system would amplify evanescent waves with these propagation constants even if there would be free*

space between the two surfaces. Actually, the mechanism of this amplification is the same as the excitation of high-amplitude oscillations in a high-quality resonator by a weak but resonant source.

This observation was then further analysed theoretically and experimentally in [Maslovski et al., 2004, Alitalo et al., 2006b]: A super-resolution lens not based on metamaterial was presented, which instead consists of two sheets supporting surface waves with a large wave number spectrum.

While in the ideal case of a metamaterial slab with $n_L = -n_R$ one obtains infinite resolution, the following limits for the resolution exist:

- Deviation from the condition $n_L = -n_R$, also due to inevitable dispersion [Smith et al., 2002b, Grbic and Eleftheriades, 2005b, Eleftheriades and Balmain, 2005, French et al., 2006]

- Losses [Grbic and Eleftheriades, 2005b, Tretyakov, 2003]

- Discrete translational symmetry, i. e., finite periodicity [Smith et al., 2002b]

- Finite slab size and hence finite lens aperture [Tretyakov, 2003, Culhaoglu et al., 2008]

An overview over publications demonstrating super-resolution is given in Sect. 2.9.

2.7 Goos-Hänchen Effect

In Sect. 2.4 *refraction* at interfaces between normal media and metamaterials was analysed. In this section *reflection* is considered. The Fresnel reflection coefficients for TE and TM polarised incident waves at a plane interface between two media are [Born et al., 1999, Russer, 2006]

$$R^{\text{TE}} = \frac{n_1 \cos\theta_1 - \sqrt{n_2^2 - n_1^2 \sin\theta_1^2}}{n_1 \cos\theta_1 + \sqrt{n_2^2 - n_1^2 \sin\theta_1^2}} = \frac{1 - (\epsilon_1/\epsilon_2)(k_{1z}/k_{2z})}{1 + (\epsilon_1/\epsilon_2)(k_{1z}/k_{2z})} \tag{2.18a}$$

$$R^{\text{TM}} = -\frac{n_2^2 \cos\theta_1 - n_1\sqrt{n_2^2 - n_1^2 \sin\theta_1^2}}{n_2^2 \cos\theta_1 + n_1\sqrt{n_2^2 - n_1^2 \sin\theta_1^2}} = -\frac{1 - (\mu_1/\mu_2)(k_{1z}/k_{2z})}{1 + (\mu_1/\mu_2)(k_{1z}/k_{2z})} \tag{2.18b}$$

with

$$k_{1z} = \sqrt{n_1 k_0^2 - k_x^2} \triangleq p_1 \qquad k_{2z} = -\text{j}\sqrt{k_x^2 - n_2 k_0^2} \triangleq -\text{j}q_2 \tag{2.19}$$
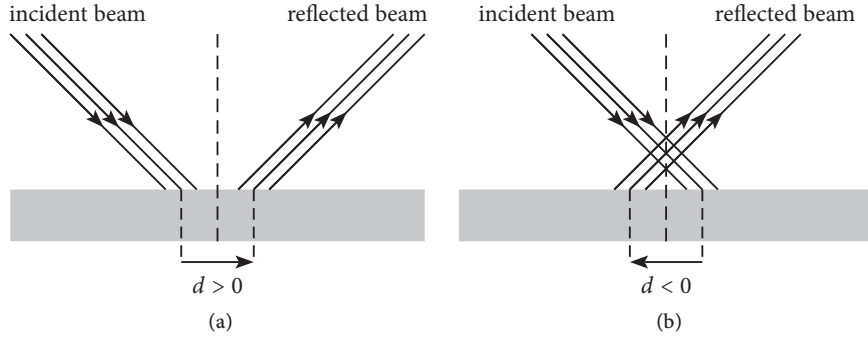
Figure 2.7: Goos-Hänchen effect: An incident beam onto an interface between two media experiences total reflection at an offset d. (a) Conventional case: $\epsilon_1/\epsilon_2 > 0$ for the TE case, $\mu_1/\mu_2 > 0$ for the TM case. (b) Reversed effect: $\epsilon_1/\epsilon_2 < 0$ for the TE case, $\mu_1/\mu_2 < 0$ for the TM case.
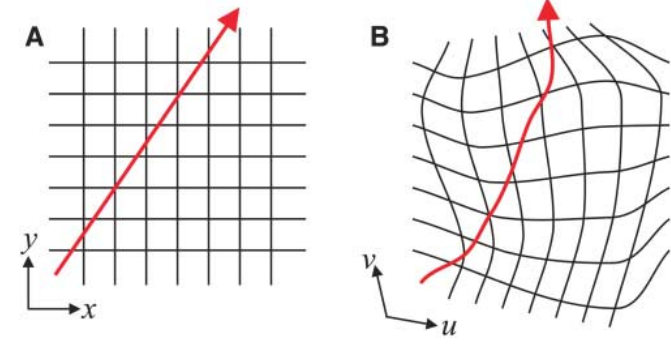

Figure 2.8: Principle of geometry transformation: (a) A field line in free space with the background Cartesian coordinate grid shown. (b) The distorted field line with the background coordinates distorted in the same fashion. The field in question may be either E, H, or the Poynting vector S. Figures taken from [Pendry et al., 2006] with permission.

Let us consider the case of total reflection, i. e., $|\sin\theta_i| > |n_2/n_1| \geq 1$. In this case the magnitudes of the reflection coefficients are equal to one, i. e., the energy is completely reflected. The phases of the reflection coefficients are

$$\arg\{R^{\mathrm{TE}}\} = 2\tan^{-1}\frac{\sqrt{n_1^2\sin^2\theta_1 - n_2^2}}{n_2\cos\theta_1} = -2\arctan\left(\frac{\epsilon_2 p_1}{\epsilon_1 q_2}\right) \tag{2.20a}$$

$$\arg\{R^{\mathrm{TM}}\} = 2\tan^{-1}\frac{\sqrt{n_1^2\sin^2\theta_1 - n_2^2}}{n_1\cos\theta_1} = \pi - 2\arctan\left(\frac{\mu_2 p_1}{\mu_1 q_2}\right) \tag{2.20b}$$

These phases of the reflection coefficients are called *Goos-Hänchen* phase shifts. The Goos-Hänchen shift in (2.20a) depends on the sign of ϵ_1/ϵ_2 while the Goos-Hänchen shift in (2.20b) depends on the sign of μ_1/μ_2. Therefore metamaterials with negative effective material parameters reverse these Goos-Hänchen shifts.

These shifts can be shown to lead to offsets d between incident and reflected *beams* [Caloz and Itoh, 2006]. This arrangement is depicted in Fig. 2.7. Like for the Goos-Hänchen shifts, if the fraction of the effective material parameters is positive one obtains $d > 0$, otherwise $d < 0$.

2.8 Electromagnetic Cloak

Two metamaterial-based approaches have been published to decrease the radar cross-section of objects, theoretically down to zero. Therefore these approaches are referred to as electromagnetic cloaks by several authors. In [Alù and Engheta, 2005] a homogeneous metamaterial coating with negative refractive index was proposed, where the electric and magnetic dipole of the object which is to be coated is compensated by the negative dipole contributions of the metamaterial coating. The cancelled dipole contribution of the coated object results in a drastic reduction of the radar cross-section. The disadvantage of this approach is that the required coating depends on the object which is to be hidden, i. e., modifying the object requires changing the coating. This severely limits the versatility of this approach.

An advanced cloaking approach was theoretically proposed in [Pendry et al., 2006] and first experimentally verified in [Schurig et al., 2006]. Here, the cloaked object remains field-free, and therefore the cloak is independent of the object that is to be hidden. The technique is referred to as *geometry transformation approach* and leads to the requirement of non-homogeneous, anisotropic permeabilities and permittivities that each vary between zero and one. This geometry transformation approach is depicted in Fig. 2.8, illustrating the correspondence of anisotropic material parameters and distorted wave propagation.
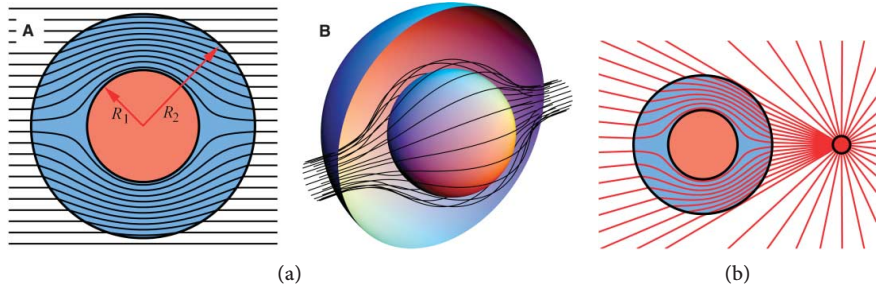
(a)   (b)

Figure 2.9: Power flow through a spherical electromagnetic cloak based on the geometry transformation approach. Figures taken from [Pendry et al., 2006] with permission.
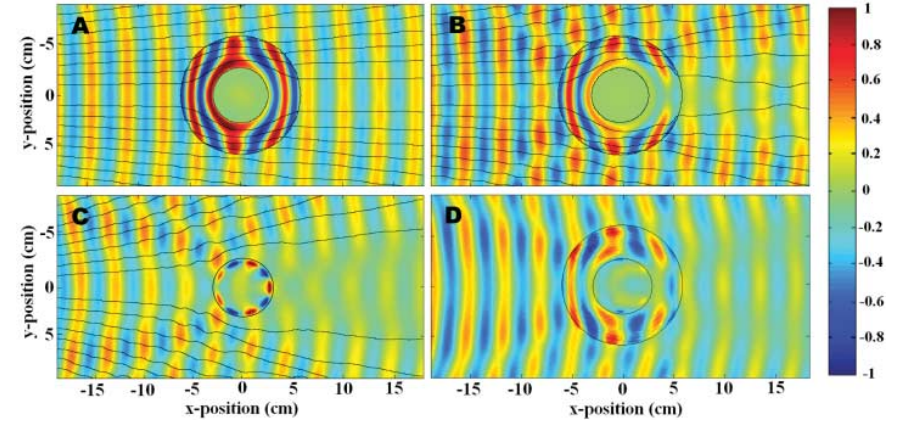

Figure 2.10: Simulation and experimental verification of an electromagnetic cloak based on the geometry transformation approach, taken from [Schurig et al., 2006] with permission. Snapshots of the time-dependent, steady-state electric field pattern, black lines indicate the Poynting vector. (a) simulation of the setup, (b) simulation of the setup with reduced material properties, (c) experimental measurement of a conducting cylinder without cloak, (d) experimental measurement of a cloaked conducting cylinder.

This technique has an analogon to mesh deformations in computational electromagnetics, e. g., parametric geometry variations in the finite element method (FEM) or conformal meshes in the finite difference time domain method (FDTD) [Ward and Pendry, 1996, Ward and Pendry, 1998, Russer et al., 2007, Armenta and Sarris, 2008]. Taking the FEM example, a parametric sweep of geometry parameters is to be calculated. Keeping the initial mesh one accounts for the modified geometry by anisotropic material parameters. One can consider an electromagnetic cloak based on geometry transformation as being the numerical approach moulded into physical realisation. As will be shown in Chapter 3, further analogies between computational techniques and metamaterials can be drawn.

The authors of [Pendry et al., 2006] give the example of a cloak for a sphere of radius R_1 and a spherical metamaterial shell radius $R_1 \leq r \leq R_2$ that acts as a cloak with

$$\epsilon_r^r(r) = \mu_r^r(r) = \frac{R_2}{R_2 - R_1} \frac{(r' - R_1)^2}{r'} \qquad r' = R_1 + r\frac{R_2 - R_1}{R_2} \qquad (2.21a)$$

$$\epsilon_r^\theta = \mu_r^\theta = \epsilon_r^\phi = \mu_r^\phi = \frac{R_2}{R_2 - R_1} \qquad (2.21b)$$

where the superscript r, θ, ϕ denotes the respective component in a spherical coordinate system. The subscript r denotes that the relative permeability and permittivity is referred to, respectively. The resulting flux of the Poynting vector is shown in Fig. 2.9. The inner sphere remains field free, the flux is guided in a laminar manner. Both the cases of illumination by a plane wave and by a point source are depicted.

Fig. 2.10 shows simulation and measurement results of this approach. (a) de-

picts the simulation of a conducting cylinder covered with cloaking shell; (b) shows a tolerance analysis simulation with values of the permittivity and permeability not exactly ranging from zero to one. The measurement of the electric field for the coated and uncoated cases are shown in (c) and (d), respectively. The coated case has strongly reduced both the back-scattering and the shadowing effect of the conducting cylinder. This proves the general feasibility of this approach.

In the experimental verification presented in [Schurig et al., 2006] the authors had to resort to a two-dimensional experiment using a cylindric object and a cylindric coating. The three-dimensional, polarisation independent metamaterial proposed in Chapter 6 may give a solution to three-dimensional cloaks.

2.9 Selection of Publications

As an exhaustive overview of publications treating metamaterials would go beyond the scope of this thesis, here only a selection of published results is recapitulated. A more complete overview can be found in [Caloz and Itoh, 2006, Eleftheriades and Balmain, 2005, Engheta and Ziolkowski, 2006, Zedler and Russer, 2008, Marqués et al., 2008]

1. seminal papers
   - first speculation on negative refractive index materials [Veselago, 1968]
   - proposal of the perfect lens [Pendry, 2000]
   - experimental verification of the reversed Snell's law [Shelby et al., 2001]
   - proposal of transmission-line derived metamaterial structures [Caloz and Itoh, 2002, Iyer and Eleftheriades, 2002, Oliner, 2002]
   - proposal and first experimental verification of an electromagnetic cloak [Pendry et al., 2006, Schurig et al., 2006]

2. approaches to three-dimensional metamaterials
   - 3D extension of the wire/split-ring approach [Mercure et al., 2005, Koschny et al., 2005]
   - dielectric spheres in a face-centred-cubic configuration yielding left-handed behaviour through Mie-resonances [Vendik and Gashinova, 2004]
   - scalar three-dimensional metamaterials [Alitalo et al., 2006c, Alitalo et al., 2006a, Zedler et al., 2008a]
   - Kron cell derived structure [Grbic and Eleftheriades, 2005a], expanded node TLM derived structure [Hoefer et al., 2005]
   - RTLM derived structure [Zedler and Russer, 2006, Zedler et al., 2007c, Zedler et al., 2007b, Zedler and Russer, 2008]

3. guided wave applications
   - zeroth-order resonators [Sanada et al., 2003]
   - directional coupler [Caloz et al., 2003]
   - branchline coupler [Islam and Eleftheriades, 2004]
   - phase compensation [Engheta and Ziolkowski, 2005]
   - transmission line transformer for matching purposes [Damm et al., 2007]

   - anisotropic metamaterials, e. g., spatial spectrum analyser, diplexer [Balmain et al., 2003, Eleftheriades and Siddiqui, 2005, Siddiqui and Eleftheriades, 2006]

4. radiated wave applications
   - reflectors [Sievenpiper et al., 2003]
   - leaky-wave antenna [Lim et al., 2005]
   - compact antennas [Schüßler et al., 2004]
   - radar cross-section reduction [Cummer et al., 2006, Cai et al., 2007, Kildal et al., 2007]
   - acoustic cloaking [Cummer and Schurig, 2006, Chen and Chan, 2007]

5. imaging
   - sub-diffraction imaging [Fang et al., 2005, Wang et al., 2007, Smith et al., 2002b, Grbic and Eleftheriades, 2005b, Veselago et al., 2006]
   - far-field sub-diffraction optical microscopy using metamaterial crystals [Salandrino and Engheta, 2006, Smolyaninov et al., 2007]

6. further work on metamaterial synthesis
   - one-dimensional split-ring resonators [Marqués et al., 2008], scaled to yield a negative index of refraction at 780 nm [Dollinger et al., 2007]
   - chiral route to metamaterials [Tretyakov et al., 2003, Pendry, 2004]
   - two-dimensional metamaterials [Sievenpiper et al., 1999, Iyer and Eleftheriades, 2006, Shelby et al., 2001]

3 Topological Formulation of Discrete Electrodynamics

In Sect. 2.1 metamaterials were defined as *compound* artificial materials tailored to achieve a particular type of *dispersion* for their effective material parameters. This chapter presents a systematic approach of how metamaterials can be *synthesised*. Group theory allows for *analysing* the unit cell of metamaterial compounds, yielding information about isotropy. But it cannot be used as a tool to synthesise unit cells, as it only commands the level of symmetry within a unit cell, not its contents.

In the following we show that due to the properties of metamaterials of being compound materials implementing dispersion, a systematic synthesis can be performed by dividing the synthesis task into four parts: First a suitable network topology is derived using symmetry considerations [Zedler et al., 2008b], leading in several cases to topologies used in computational electromagnetics. Next, the desired type of dispersive behaviour is chosen, determining the network elements. The network topology together with the network elements form a network, which is then physically realised in order to yield a metamaterial. Finally the physical realisation is characterised using group-theoretical considerations for determining bi- or anisotropy [Padilla, 2007, Baena et al., 2007].

Using this approach known structures can be explained in a compact manner, e. g., [Smith et al., 2000, Oliner, 2002, Sievenpiper et al., 1999, Iyer and Eleftheriades, 2006]. In addition this approach can be used to synthesise new structures, as will be shown in Chapters 5 and 6.

3.1 One-Dimensional Metamaterials

In order to deduce a *topological* analysis of metamaterials let us first examine Maxwell's equations describing wave propagation in a homogeneous medium

$$\partial_z E_x(z) = -\mathrm{j}\omega\mu_0\mu_r H_y(z) \qquad \partial_z H_y(z) = -\mathrm{j}\omega\epsilon_0\epsilon_r E_x(z) \qquad (3.1)$$
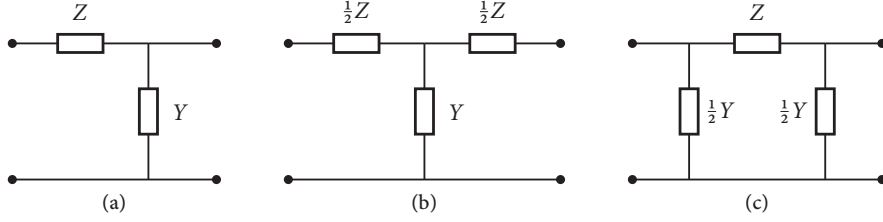
Figure 3.1: Equivalent circuits modelling transmission lines (a) unit cell due to the first order discretisation to the telegrapher's equation, (b) symmetrised unit cell in 'T'-configuration, and (c) symmetrised unit cell in 'Π'-configuration.

The transmission-line analogon to (3.1) is

$$\partial_z V(z) = -Z' \cdot I(z) \qquad\qquad \partial_z I(z) = -Y' \cdot V(z) \qquad (3.2)$$

which is the step to a topological description and is considered a formal substitution within the scope of this chapter. A rigorous analysis of the relation between the field description and the network description can be performed using *structure functions* with their accompanying *generalised voltages and currents*[1]. Obviously the network theory analogon does not reduce the manifold of solutions to the wave equation. Both equations (3.1) and (3.2) have continuous translation symmetry as they describe wave propagation in a homogeneous, uniform medium. Using generalised voltages and currents then the impedance per unit length Z' and the admittance per unit length Y' are

$$Z' = \mathrm{j}\omega\mu_0\mu_r \qquad\qquad Y' = \mathrm{j}\omega\epsilon_0\epsilon_r \qquad (3.3)$$

Hence Z', Y' directly relate to the – possibly dispersive – material parameters. A first order space-discretising numerical scheme to (3.2) resulting in *discrete* translational symmetry is

$$V(z+\Delta z) - V(z) = -Z \cdot I(z) \qquad I(z+\Delta z) - I(z) = -Y \cdot V(z) \qquad (3.4)$$

with $Z = Z'\Delta z$ and $Y = Y'\Delta z$. The corresponding network to (3.4) is depicted in Fig. 3.1(a). For structures with continuous translational symmetry (3.4) is an approximation. For metamaterials, however, these equations are exact because metamaterials are composite artificial structures of finite size and hence with inherent

---

1 Appendix A.4 contains an introduction to structure functions.

discrete translation symmetry. It shall be emphasised that Fig. 3.1(a) is an equivalent circuit which will be used for modelling metamaterials. It does *not* enforce the usage of lumped elements.

Using the chain matrix based algebraic analysis technique for periodic structures presented in Appendix A.5.1 one obtains the dispersion relation to (3.4)

$$\sinh^2\left(\tfrac{1}{2}\gamma\Delta z\right) = \tfrac{1}{4}ZY \overset{\mathrm{Re}\{\gamma\}=0}{=} -\sin^2\tfrac{1}{2}\chi \qquad (3.5)$$

with the complex propagation constant γ and the phase shift across a unit cell $\chi = \mathrm{Im}\{\gamma\}\Delta z = 2\pi\Delta z/\lambda$. In the loss-less case, i. e., $\mathrm{Re}\{Z\} = \mathrm{Re}\{Y\} = 0$, one obtains a pass-band for $-1 \le \tfrac{1}{4}ZY \le 0$ and a stop-band otherwise. In the stop-band case the attenuation per unit cell is $2\,\mathrm{arsinh}\left(\tfrac{1}{2}\sqrt{ZY}\right)$.

As stated in Sect. 2.1, a periodic structure operates like a metamaterial if the unit cell size is small compared to the wavelength. In terminology of the *reciprocal lattice*[1] this corresponds to the vicinity of the Γ-point, which for the one-dimensional case is $\chi = 2\pi\Delta z/\lambda \ll 1$. In this case the dispersion relation (3.5) reads

$$-\tfrac{1}{4}ZY = \sin^2\tfrac{1}{2}\chi \approx \tfrac{1}{4}\chi_\Gamma^2 \qquad \rightarrow \qquad \chi_\Gamma = \sqrt{-ZY} \qquad (3.6)$$

with the subscript Γ denoting that (3.6) is only valid in the vicinity of the Γ-point.

Apart from the dispersion relation, the second quantity characterising a periodic structure is the Bloch impedance. It is defined as the ratio of the transverse electric and magnetic fields (or the related ratio of the voltage wave amplitude and current wave amplitude) at a certain reference plane within the unit cell. It is the analogon to the characteristic impedance, which is used for the description of structures with continuous translational symmetry.

Because the Bloch impedance depends on the choice of the reference plane, it has different values for the unit cells with asymmetric, 'T'-, and 'Π'-configuration shown in Fig. 3.1. Using the chain matrix based analysis approach presented in Appendix A.5.1 one obtains for the symmetric unit cells

$$Z_{\mathrm{Bloch,T}} = \sqrt{Z/Y} \cdot \sqrt{1 + \tfrac{1}{4}ZY} = \sqrt{Z/Y} \cdot \cosh\left(\tfrac{1}{2}\gamma\Delta z\right) \qquad (3.7a)$$

$$Z_{\mathrm{Bloch,\Pi}} = \sqrt{Z/Y} \,/\, \sqrt{1 + \tfrac{1}{4}ZY} = \sqrt{Z/Y} \,/\, \cosh\left(\tfrac{1}{2}\gamma\Delta z\right) \qquad (3.7b)$$

The Bloch impedance for the asymmetric unit cell is different for waves travelling

---

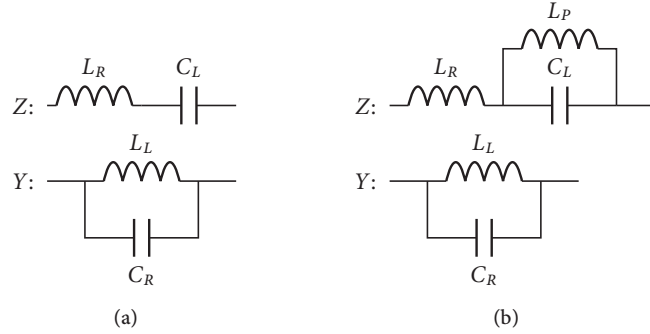1 Appendix A.2 contains an introduction to the concept of the reciprocal lattice.

Figure 3.2: Unit cell elements for Fig. 3.1. (a) unit cell elements modelling Drude dispersion for both μ_r and ϵ_r, (b) unit cell elements modelling μ_r following Lorentz dispersion, and ϵ_r following Drude dispersion.
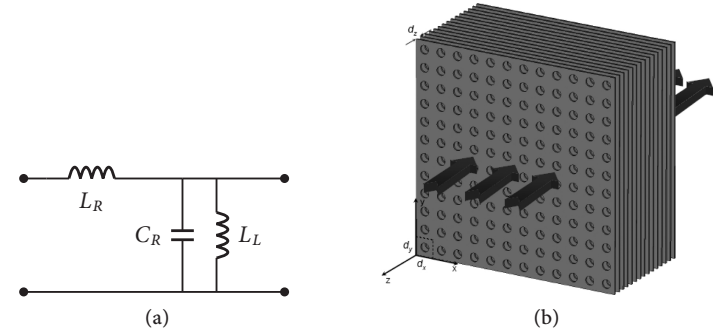

Figure 3.3: (a) Equivalent circuit of a waveguide segment of length Δz operating in TE mode with cut-off frequency ω_c having $L_R = \mu\Delta z$, $C_R = \epsilon\Delta z$, and $\omega_c^2 L_L C_R = 1$. (b) Stacked periodically perforated thick metallic screens. © 2007 IEEE, taken from [Beruete et al., 2007].

in the $+z$ and $-z$-direction:

$$Z_{\text{Bloch}}^{(+)} = \frac{2Z}{\sqrt{ZY(4+ZY)} - ZY} = Z_{\text{Bloch,T}} + \tfrac{1}{2}Z \tag{3.7c}$$

$$Z_{\text{Bloch}}^{(-)} = \frac{2Z}{\sqrt{ZY(4+ZY)} + ZY} = \left(Z_{\text{Bloch,}\Pi}^{-1} + \tfrac{1}{2}Y\right)^{-1} \tag{3.7d}$$

where the superscript denotes the direction of propagation. As stated above, the Bloch impedance is the analogon to the characteristic impedance and thus it determines the level of matching between the metamaterial and a surrounding medium or structure. Inspecting (3.7), in addition to the design of the elements of the unit cell (Z, Y), also the choice of the unit cell reference plane interfacing the other medium can be used as a means to control matching.

3.1.1 Implementation of Dispersion

The choice of the series element Z and shunt element Y determines the type of dispersion, Drude dispersion or Lorentz dispersion being the two most common types. This is shown in Fig. 3.2: Using series resonators for Z and parallel resonators for Y results in the composite right/left-handed (CRLH) approach [Oliner, 2002, Eleftheriades and Balmain, 2005, Caloz and Itoh, 2006] yielding Drude dispersion for both the effective permeability and permittivity [Zedler et al., 2007a]

$$Z = \text{j}\omega\mu_0\mu_{\text{eff}}\Delta z = \text{j}\omega\mu_0\mu_\infty\Delta z\left(1 - \omega_{0,\mu}^2/\omega^2\right) \tag{3.8a}$$

$$Y = \text{j}\omega\epsilon_0\epsilon_{\text{eff}}\Delta z = \text{j}\omega\epsilon_0\epsilon_\infty\Delta z\left(1 - \omega_{0,\epsilon}^2/\omega^2\right) \tag{3.8b}$$

where $\mu_\infty, \epsilon_\infty$ are the relative permeability and permittivity for $\omega \to \infty$, respectively. $\omega_{0,\mu}$ and $\omega_{0,\epsilon}$ denote the magnetic and electric plasmon resonance frequencies, respectively. The correspondence between (3.8) and Fig. 3.2(a) is

$$\mu_0\mu_\infty\Delta z = L_R \qquad \epsilon_0\epsilon_\infty\Delta z = C_R \qquad \omega_{0,\mu}^2 L_R C_L = 1 \qquad \omega_{0,\epsilon}^2 L_L C_R = 1 \tag{3.9}$$

The motivation to use the terminology of (3.8) is that dispersion of effective *material* parameters is treated within this chapter.

For the synthesis of physical structures it is possible and common to directly incorporate the network as of Fig. 3.1 and Fig. 3.2(a) using lumped elements, i. e., series capacitors connected to shunt inductors. These elements together with their unavoidable parasitics then physically realise double Drude dispersion. It shall be emphasised that incident free space waves can interact also with this type of structure. In the case of a free space wave setup it needs to be ensured that at the operational frequency the metamaterial structure is mono-modal [Iyer and Eleftheriades, 2008], see also Sect. 6.7.
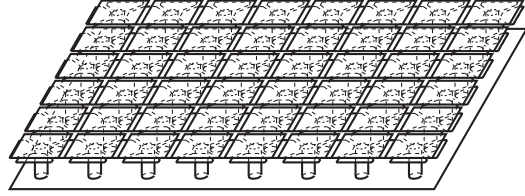
Figure 3.4: Mushroom structure. Taken from [Russer, 2006] with permission.

Apart from these lumped elements physical realisations, structures that are based solely on distributed elements have been proposed. An example of a one-dimensional structure is a setup of periodically perforated thick metallic screens stacked at a small distance as shown in Fig. 3.3 [Beruete et al., 2007]. The perforated thick screen can be regarded as periodically arranged hollow waveguides. As derived in Appendix A.4 the equivalent circuit of a hollow waveguide segment in TE modes is a series inductance connected to a parallel resonator. Inspecting Fig. 3.2(a) one notes that the perforated thick screen therefore realises Drude dispersion for the permittivity. In order to obtain Drude dispersion also for the permeability, according to Fig. 3.2(a) an additional series capacitance is needed. Within the stacked screens setup the physical realisation is achieved via capacitive coupling of adjacent screens. Further approaches based on TE mode propagation and series capacitances have been proposed in, e.g., substrate integrated waveguide technology [Weitsch and Eibert, 2007].

An example of a two-dimensional distributed double Drude metamaterial is the mushroom structure [Sievenpiper et al., 1999] depicted in Fig. 3.4. Inductive posts implement a shunt inductance while the gap between the top plates of the mushrooms provides a series capacitance. The distance between the gap and the post is a short piece of transmission line yielding a series inductance and a shunt capacitance. In total one obtains a series resonator and a shunt resonator, i.e., double Drude dispersion. Details of wave propagation in double Drude metamaterials are given in the next Sect. 3.1.2.

Lorentz dispersion for the permeability and Drude dispersion for the permittivity result in

$$Z = \mathrm{j}\omega\mu_0\mu_{\mathrm{eff}}\Delta z = \mathrm{j}\omega\mu_0\mu_\infty\Delta z \left(1 - \frac{\omega_{0,\mu}^2}{\omega^2 - \omega_{\infty,\mu}^2}\right) \tag{3.10a}$$

$$Y = \mathrm{j}\omega\epsilon_0\epsilon_{\mathrm{eff}}\Delta z = \mathrm{j}\omega\epsilon_0\epsilon_\infty\Delta z \ \left(1 - \omega_{0,\epsilon}^2/\omega^2\right) \tag{3.10b}$$

The network elements to Fig. 3.1 modelling this type of dispersion are shown in Fig. 3.2(b). Their relation to (3.10a) is

$$\mu_0\mu_\infty\Delta z = L_R \qquad \omega_{0,\mu}^2 L_R C_L = 1 \qquad \omega_{\infty,\mu}^2 L_P C_L = 1 \tag{3.11}$$

As expected, Lorentz dispersion passes into Drude dispersion for $\omega_{\infty,\mu} \to 0$ and hence in the equivalent circuit of Fig. 3.2(b) for $L_P \to \infty$.

Physical realisations of Lorentz/Drude dispersion are for example the split-ring resonator (SRR)/wire grid configuration shown in Fig. 3.5 as well as Mie resonant dielectric resonators [Vendik and Gashinova, 2004, Ueda et al., 2007, Gaillot et al., 2008].

An illustration showing the correspondences between the contents of the SRR/wire grid unit cell and the related equivalent circuit is shown in Fig. 3.5(d–e). It shall be emphasised that this equivalent circuit is only valid in the quasi-static approximation, i. e., the unit cell is small compared to the wavelength. The electric field of an incident wave is parallel to the wire grid, which loads the effective permittivity inductively with L_L. The SRR is modelled by C_L', L_P'. This resonator is probed by the magnetic field which is parallel to the SRR plane normal vector. Due to the coupling of the magnetic field with the resonator the effective permeability is modified. Last, the free space between split rings is modelled by a ladder network with the elements L_R, C_R. The equivalent circuit of Fig. 3.5(e) shows the direct correspondence to Fig. 3.5(d). The coupling of the magnetic field to the resonator is modelled by an ideal transformer. Simplifying and re-arranging the network in Fig. 3.5(e) yields Fig. 3.5(f). Here the elements C_L', L_P' are transformed into the elements C_L, L_P by virtue of the transformer ratio. The resulting network is of the type shown in Fig. 3.2, which describes mixed Lorentz/Drude dispersion.

Re-examining (3.10a) it is desirable to reduce $\omega_{\infty,\mu}$ while keeping $\omega_{0,\mu}$ and the unit cell size constant in order to improve the bandwidth of left-handed operation. This translates into the requirement to solely enlarge L_P, which can unfortunately only be achieved to a small degree with the SRR approach. Further, the resonance within the SRR is particularly prone to losses.

If SRR are combined with cut-wires this yields Lorentz dispersion for the permittivity and the permeability. This can be seen from Fig. 3.5(d) by substituting the inductance L_L with a series resonator, where the series capacitance is modelling the capacitive gap between the cut wires. The corresponding equivalent circuit is shown in Fig. 3.6.

Figure 3.6: Equivalent circuit of a metamaterial where the dispersion of both the permittivity and the permeability are of Lorentz-type.

Similar to the above discussion, one obtains Drude dispersion for the permeability and Lorentz dispersion for the permittivity with the complementary SRR configuration [Baena et al., 2005]. In this configuration the SRR geometry is etched periodically into a ground plane and forms together with a microstrip line with periodic series gap capacitors the metamaterial.

A further topology-derived metamaterial was presented in [Shamonina et al., 2002]. This magneto-inductive unit cell consists of resonant loops inter-coupled by their mutual inductance, leading to dispersion different from the Drude and Lorentz type.

Arbitrary types of dispersion can be obtained by performing the canonical fractional expansion representation of the one-ports Z, Y. These *Foster representations* of Z and Y are given by [Cauer, 1954, Belevitch, 1968, Russer, 2006]

$$Z(\omega) = \frac{1}{j\omega C_{p0}} + \sum_{n=1}^{\infty} \frac{1}{j\left(\omega C_{pn} - \frac{1}{\omega L_{pn}}\right)} + j\omega L_{p\infty} \tag{3.12a}$$

$$Y(\omega) = \frac{1}{j\omega L_{s0}} + \sum_{n=1}^{\infty} \frac{1}{j\left(\omega L_{sn} - \frac{1}{\omega C_{sn}}\right)} + j\omega C_{s\infty}, \tag{3.12b}$$

The lumped element equivalent circuits of Foster impedance and admittance representations are shown in Fig. 3.7. The advantages of this topology based dispersion engineering approach presented in this section are that this abstract point of view simplifies the synthesis and analysis of structures while at the same time causality is unconditionally preserved. The latter may pose a problem in other formulations [Engheta and Ziolkowski, 2006, Caloz and Itoh, 2006, Zedler and Russer, 2007], see also Sect. 2.1.

Because the emphasis of this chapter lies in a topological synthesis approach
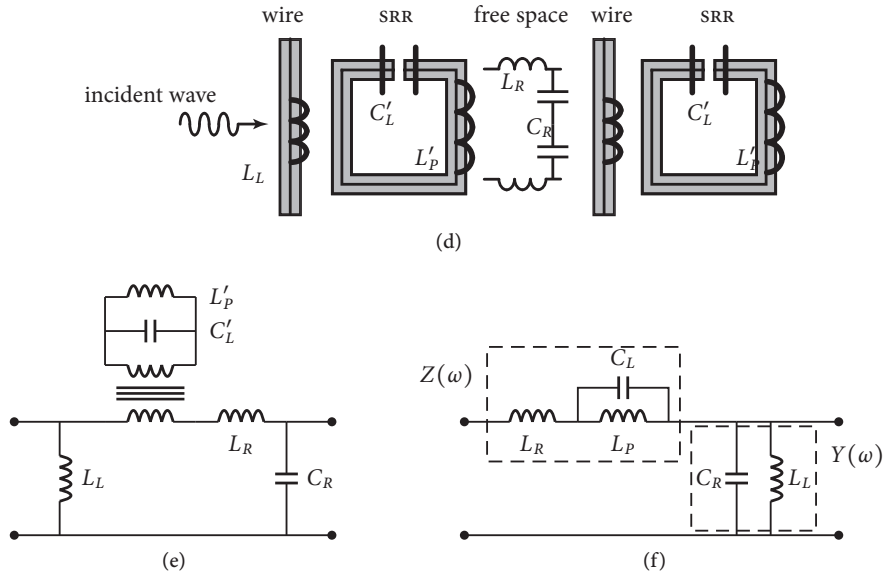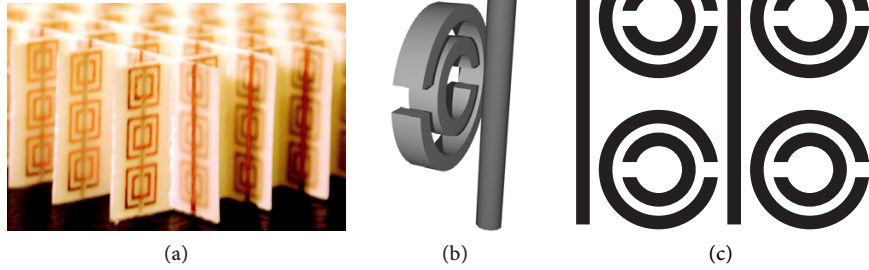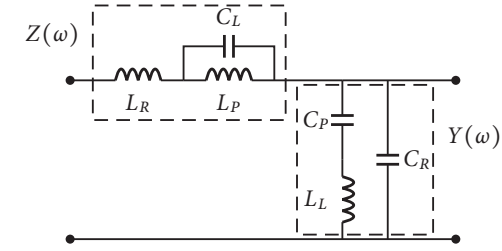

(a)　(b)　(c)

(d)

(e)　(f)

Figure 3.5: (a) Two-dimensional SRR/wire grid arrangement, taken from [Shelby et al., 2001], (b) visualisation of single SRR/wire grid unit cell, taken from [Casse et al., 2006], (c) planar SRR/wire grid arrangement, (d) wave travelling through a SRR/wire grid metamaterial. (e) correspondence of unit cell contents with network elements. (f) simplified equivalent circuit.
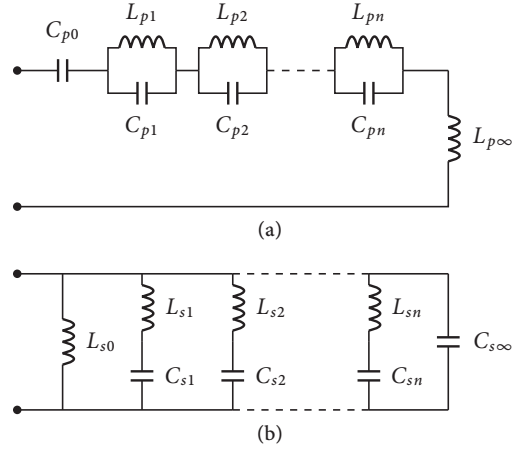
Figure 3.7: Canonical Foster equivalent circuits of one-ports: (a) Foster impedance representation, (b) Foster admittance representation.

to metamaterials, losses are not specifically treated. Losses can be added to the models by taking the left-handed elements C_L, L_L as being lossy. As examples referring to Fig. 3.2, a lossy Drude dispersive permittivity $\epsilon_{\text{eff}} \propto 1 - \frac{\omega_{0,\epsilon}^2}{\omega^2 - j\gamma\omega}$ can be modelled by a lossy inductance L_L. A Lorentz dispersive permeability $\mu_{\text{eff}} \propto 1 - \frac{\omega_{0,\mu}^2}{\omega^2 - j\gamma\omega - \omega_{\infty,\mu}}$ can be modelled by a lossy capacitance C_L.

3.1.2 Double Drude Metamaterials

If both the permittivity and permeability follow Drude dispersion, the equivalent one-port elements of the network are given by (3.8). As mentioned in the previous section, this case is often referred to in literature as *composite right/left handed* (CRLH) or *transmission-line metamaterial*.

The proposal of double Drude metamaterials in 2002 [Oliner, 2002, Eleftheriades et al., 2002, Caloz and Itoh, 2002] led to the discussion about the relation of this type of metamaterial to filter theory, because in the one-dimensional case the double Drude metamaterial equals the band-pass elementary cell prototype. Several reasons were given why it makes sense also in the one-dimensional case to use the terminology of metamaterials: New applications were invented which are more easily described using this terminology, e. g., new types of leaky wave antennas, new types of couplers. Further, a one-dimensional metamaterial

can be considered being a special case of an isotropic multi-dimensional metamaterial.

The purpose of the previous Sect. 3.1 was indeed to relate dispersion of *arbitrary* (not only CRLH) metamaterials to filter theory. While filter theory is one part of the framework for the analysis and synthesis of metamaterials, the other part is network topology. Chapters 4, 5, and 6 discuss extensions of the topology to the multi-dimensional isotropic case. Considering a certain direction of propagation in an isotropic multi-dimensional metamaterial yields the special case of one-dimensional propagation. The present section's aim is to give an overview of the properties of double Drude metamaterials for this case.

For a double Drude metamaterial the equivalent circuit elements were given in (3.8). Using these elements the frequency dependent term of the dispersion relation (3.5) is

$$Z \cdot Y = -\omega^2 \mu_0 \mu_\infty \epsilon_0 \epsilon_\infty \Delta z^2 \left(1 - \omega_{0,\mu}^2/\omega^2\right) \left(1 - \omega_{0,\epsilon}^2/\omega^2\right)$$
$$= -\Omega^2 \cdot \qquad\qquad \left(1 - \Omega_{0,\mu}^2/\Omega^2\right)\left(1 - \Omega_{0,\epsilon}^2/\Omega^2\right) \qquad (3.13)$$

with the normalised frequencies

$$\Omega^2 = \omega^2 \quad \cdot \mu_0\mu_\infty\epsilon_0\epsilon_\infty\Delta z^2 \qquad\qquad\qquad (3.14a)$$
$$\Omega_{0,\mu}^2 = \omega_{0,\mu}^2 \quad \cdot \mu_0\mu_\infty\epsilon_0\epsilon_\infty\Delta z^2 \qquad\qquad (3.14b)$$
$$\Omega_{0,\epsilon}^2 = \omega_{0,\epsilon}^2 \quad \cdot \mu_0\mu_\infty\epsilon_0\epsilon_\infty\Delta z^2 \qquad\qquad (3.14c)$$

Using (3.13) the dispersion relation (3.5) reads

$$\sin^2 \tfrac{1}{2}\chi = \tfrac{1}{4}\Omega^2 \left(1 - \Omega_{0,\mu}^2/\Omega^2\right)\left(1 - \Omega_{0,\epsilon}^2/\Omega^2\right) \qquad (3.15)$$

Solving (3.15) for Ω yields the two frequency bands

$$\Omega^2 = 2\sin^2 \tfrac{1}{2}\chi + \tfrac{1}{2}\left(\Omega_{0,\epsilon}^2 + \Omega_{0,\mu}^2\right) \pm \sqrt{\left(2\sin^2 \tfrac{1}{2}\chi + \tfrac{1}{2}\left(\Omega_{0,\epsilon}^2 + \Omega_{0,\mu}^2\right)\right)^2 - \Omega_{0,\epsilon}^2\Omega_{0,\mu}^2}$$
$$(3.16)$$

Two cases need to be considered: If the plasmon resonance frequencies of the permeability and permittivity match, $\Omega_{0,\mu} = \Omega_{0,\epsilon} \triangleq \Omega_0$, the structure is called *resonance-balanced*, otherwise *resonance-unbalanced*. These two cases are shown in the dispersion diagram[1] of Fig. 3.8: In the unbalanced case one obtains a stop-band between the lower band and the upper band at the Γ-point. Re-inspecting (3.8), this stop-band can be interpreted as being due to opposite signs of the permeability and permittivity. This stop-band vanishes in the case of matching plasmon resonance frequencies.

---

[1] Appendix A.3 contains an introduction to the concept of dispersion diagrams.
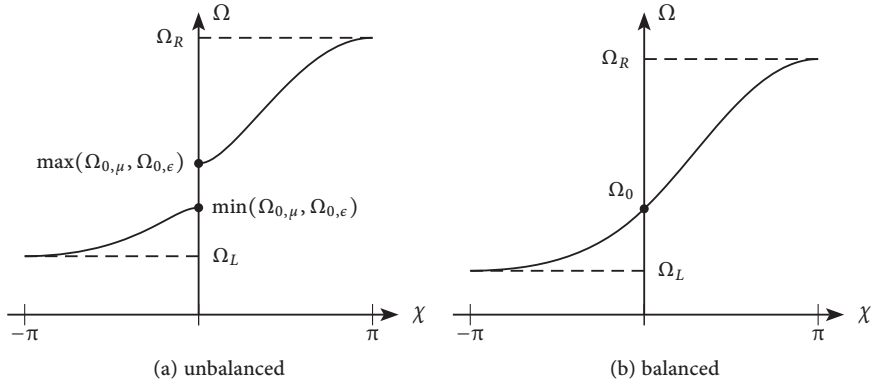
(a) unbalanced

(b) balanced

Figure 3.8: Dispersion diagram of a double Drude metamaterial.

The lower cut-off frequency Ω_L and the upper cut-off frequency Ω_R are determined by setting $\sin\frac{1}{2}\chi = 1$ in (3.16). The resulting cut-off frequencies are

$$\Omega_L^2, \Omega_R^2 = 2 + \frac{1}{2}\left(\Omega_{0,\epsilon}^2 + \Omega_{0,\mu}^2\right) \mp \sqrt{\left(2 + \frac{1}{2}\left(\Omega_{0,\epsilon}^2 + \Omega_{0,\mu}^2\right)\right)^2 - \Omega_{0,\epsilon}^2 \Omega_{0,\mu}^2} \quad (3.17)$$

which simplifies in the resonance-balanced case to

$$\Omega_L, \Omega_R = \mp 1 + \sqrt{\Omega_0^2 + 1} \quad (3.18)$$

The phase velocity c_{phase} and group velocity c_{group} are obtained from the dispersion relation (3.5) yielding

$$c_{\text{phase}} \propto \frac{\Omega}{\chi} = \frac{\Omega}{2\arcsin(\frac{1}{2}\sqrt{-ZY})} \quad (3.19a)$$

$$c_{\text{group}} \propto \frac{1}{\partial_\Omega \chi} = \frac{1}{2\,\partial_\Omega \arcsin(\frac{1}{2}\sqrt{-ZY})} \quad (3.19b)$$

The effective refractive index n_{eff} is related to the phase velocity by

$$n_{\text{eff}} \propto c_{\text{phase}}^{-1} \qquad \text{for} \quad \chi \ll 1 \quad (3.20)$$

The restriction $\chi \ll 1$ in (3.20) is due to the fact that the effective refractive index is only defined if the metamaterial unit cell is small compared to the wavelength. Eqs. (3.19a), (3.19b), and (3.20) are plotted for the resonance-balanced and

(a) unbalanced-resonance case
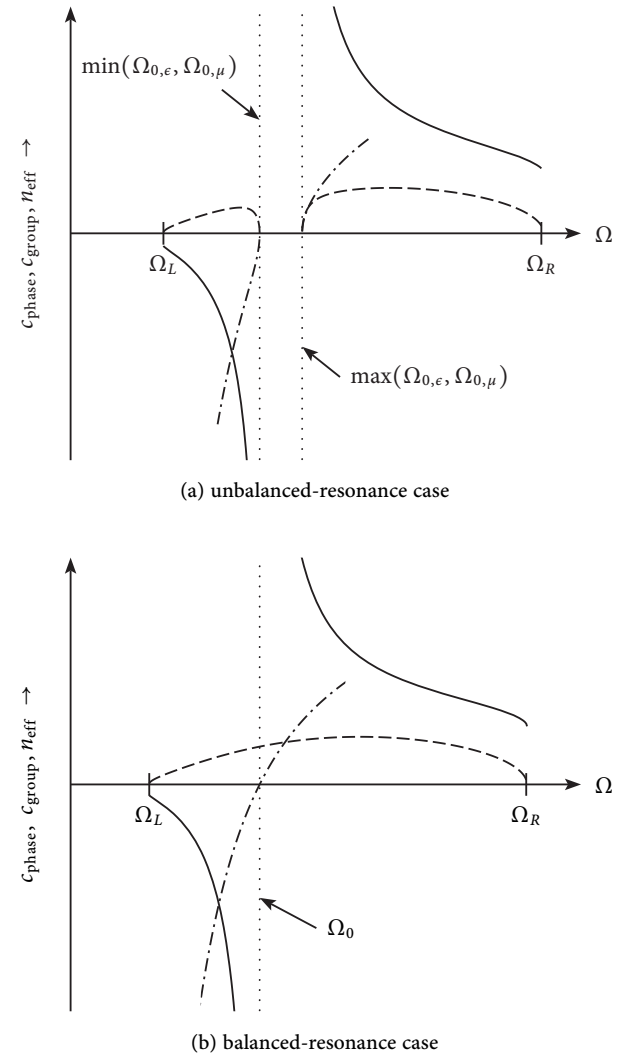

(b) balanced-resonance case

Figure 3.9: Phase velocity c_{phase} (solid line), group velocity c_{group} (dashed line), and effective refractive index n_{eff} (dash dotted line) of a double Drude metamaterial. n_{eff} is only defined if the unit cell is small compared to the wavelength, here $\chi \leq \frac{1}{4}\pi$ is used.

resonance-unbalanced case in Fig 3.9. For low frequencies $\Omega < \min(\Omega_{0,\mu}, \Omega_{0,\epsilon})$ left-handed behaviour with $n_{\text{eff}} < 0$ is obtained. On the other hand for high frequencies $\Omega > \max(\Omega_{0,\mu}, \Omega_{0,\epsilon})$ one gets right-handed behaviour with $n_{\text{eff}} > 0$.

Of particular interest in the resonance-balanced case is operation in the vicinity of the Γ-point, i. e., close to the resonance frequency Ω_0. Here, the phase velocity diverges, and the effective refractive index, the effective permeability and effective permittivity are zero. At the same time the group velocity is finite, allowing energy transfer. This interesting property can be used in various applications, Sect. 2.9 lists a selection of publications.

Another property of the resonance-balanced condition is that for operation in the vicinity of the Γ-point, i. e., $\chi \ll 1$, the dispersion relation (3.6) decouples into two summands:

$$\chi_\Gamma = \sqrt{-ZY} = \Omega - \frac{\Omega_0^2}{\Omega} \hat{=} \chi_{\Gamma,R} + \chi_{\Gamma,L} \tag{3.21}$$

$\chi_{\Gamma,R}$ is a purely right-handed contribution, whereas $\chi_{\Gamma,L}$ is purely left-handed. This property can be useful, e. g., for soliton propagation in structures enriched by nonlinearities [Gupta and Caloz, 2007].

The frequency dependence of the Bloch impedances in 'T'-configuration (3.7a) and 'Π'-configuration (3.7b) are

$$Z_{\text{Bloch,T}} = \sqrt{\frac{\mu_0 \mu_\infty}{\epsilon_0 \epsilon_\infty}} \sqrt{\frac{1 - \Omega_{0,\mu}^2/\Omega^2}{1 - \Omega_{0,\epsilon}^2/\Omega^2}} \cdot \cos\tfrac{1}{2}\chi \tag{3.22a}$$

$$Z_{\text{Bloch,Π}} = \sqrt{\frac{\mu_0 \mu_\infty}{\epsilon_0 \epsilon_\infty}} \sqrt{\frac{1 - \Omega_{0,\mu}^2/\Omega^2}{1 - \Omega_{0,\epsilon}^2/\Omega^2}} / \cos\tfrac{1}{2}\chi \tag{3.22b}$$

In the resonant-balanced case the second square root cancels, leading to

$$Z_{\text{Bloch,bal,T}} = \sqrt{\frac{\mu_0 \mu_\infty}{\epsilon_0 \epsilon_\infty}} \cdot \cos\tfrac{1}{2}\chi \tag{3.23a}$$

$$Z_{\text{Bloch,bal,Π}} = \sqrt{\frac{\mu_0 \mu_\infty}{\epsilon_0 \epsilon_\infty}} / \cos\tfrac{1}{2}\chi \tag{3.23b}$$

As the term $\cos\tfrac{1}{2}\chi$ is constant to first order for small arguments, the Bloch impedance is constant in the vicinity of the Γ-point for the resonance-balanced case.

The frequency dependence of the Bloch impedance for the resonance-unbalanced case (3.22) and resonance-balanced case (3.23) is shown in Fig. 3.10(a) for
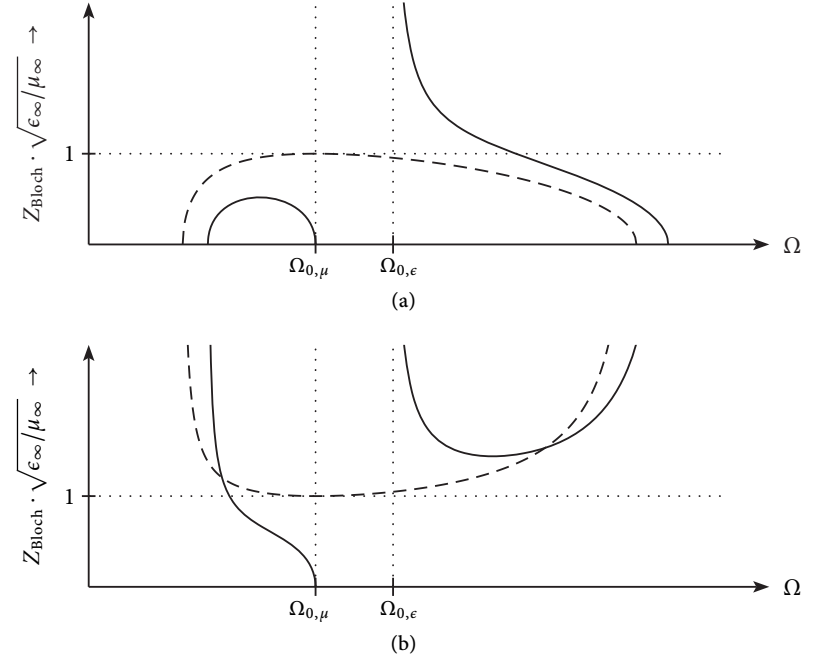
Figure 3.10: Frequency dependence of the Bloch impedance of a double Drude metamaterial. Solid line: resonance-unbalanced case with $\Omega_{0,\mu} < \Omega_{0,\epsilon}$. Dashed line: resonance-balanced case. (a) 'T'-configuration, (b) 'Π'-configuration.

the 'T'-configuration and in Fig. 3.10(b) for the 'Π'-configuration. As mentioned, for the resonance-balanced case the Bloch impedance is flat in the vicinity of the Γ-point. This allows broadband matching and was exploited in several applications.

In summary, the advantages of the resonance-balanced condition are a) broadband matching, b) zero refractive index, and c) finite group velocity. For these reasons the majority of publications treating double Drude metamaterials usually aim for this condition, see Sect. 2.9 for details. For imaging applications, where an effective refractive index $n_{\text{eff}} \approx -1$ is sought, the resonance-balance condition is of less interest, because one needs to operate further away from the Γ-point.

3.1.3 Lorentz/Drude Metamaterials

For a Lorentz/Drude metamaterial the equivalent circuit elements were given in (3.10). Using these elements the frequency dependent term of the dispersion relation (3.5) is

$$Z \cdot Y = -\omega^2 \mu_0 \mu_\infty \epsilon_0 \epsilon_\infty \Delta z^2 \left(1 - \frac{\omega_{0,\mu}^2}{\omega^2 - \omega_{\infty,\mu}^2}\right)\left(1 - \frac{\omega_{0,\epsilon}^2}{\omega^2}\right)$$

$$= -\Omega^2 \cdot \qquad \left(1 - \frac{\Omega_{0,\mu}^2}{\Omega^2 - \Omega_{\infty,\mu}^2}\right)\left(1 - \frac{\Omega_{0,\epsilon}^2}{\Omega^2}\right) \qquad (3.24)$$

with

$$\Omega^2 = \omega^2 \qquad \cdot \mu_0 \mu_\infty \epsilon_0 \epsilon_\infty \Delta z^2 \qquad (3.25a)$$

$$\Omega_{0,\mu}^2 = \omega_{0,\mu}^2 \quad \cdot \mu_0 \mu_\infty \epsilon_0 \epsilon_\infty \Delta z^2 \qquad (3.25b)$$

$$\Omega_{\infty,\mu}^2 = \omega_{\infty,\mu}^2 \quad \cdot \mu_0 \mu_\infty \epsilon_0 \epsilon_\infty \Delta z^2 \qquad (3.25c)$$

$$\Omega_{0,\epsilon}^2 = \omega_{0,\epsilon}^2 \quad \cdot \mu_0 \mu_\infty \epsilon_0 \epsilon_\infty \Delta z^2 \qquad (3.25d)$$

In physical realisations of Lorentz/Drude metamaterials the pole $\Omega_{\infty,\mu}$ is affected by the mutual coupling of adjacent resonators [Eleftheriades and Balmain, 2005] and in the limit for infinitely strong coupling degenerates into double Drude dispersion. This behaviour can be observed as (3.24) equals (3.13) in the limit $\Omega_{\infty,\mu} \to 0$.

Inserting (3.24) into the dispersion relation (3.5) one obtains for $\Omega_{\infty,\mu} > \Omega_{0,\epsilon}$ solely one right-handed band, for $\Omega_{\infty,\mu} < \Omega_{0,\epsilon}$ one obtains in addition to a right-handed band also a left-handed band. In the latter case the frequencies at the Γ-point are obtained by setting $\sin^2 \frac{1}{2}\chi = 0 = -\frac{1}{4}ZY$ and solving for the frequencies, yielding $\Omega_\Gamma = \{\Omega_{0,\epsilon}, \sqrt{\Omega_{\infty,\mu}^2 + \Omega_{0,\mu}^2}\}$. Setting these two frequencies equal one obtains a transition from the left-handed band to the right-handed band without an intermediate stop-band, resulting in the resonance-balance condition for a Lorentz/Drude metamaterial

$$\Omega_{0,\epsilon}^2 = \Omega_{\infty,\mu}^2 + \Omega_{0,\mu}^2 \stackrel{!}{=} \Omega_0^2 \qquad (3.26)$$

which can be expressed by $C_L C_R^{-1} = L_L(L_R^{-1} + L_P^{-1})$ using (3.9) and (3.11) and thus the equivalent circuit elements shown in Fig. 3.2. In the resonance-balanced case (3.24) simplifies to

$$Z \cdot Y = -\Omega^2 \left(1 - \frac{\Omega_0^2 - \Omega_{\infty,\mu}^2}{\Omega^2 - \Omega_{\infty,\mu}^2}\right)\left(1 - \frac{\Omega_0^2}{\Omega^2}\right) = -\frac{\left(\Omega^2 - \Omega_0^2\right)^2}{\Omega^2 - \Omega_{\infty,\mu}^2} \qquad (3.27)$$
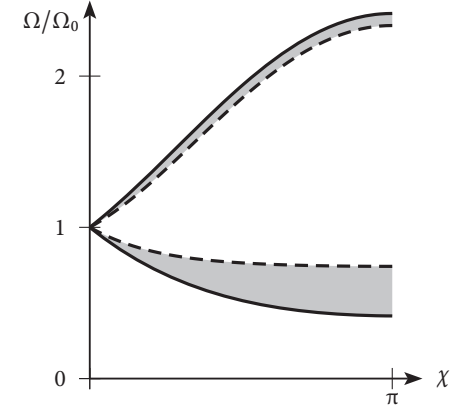

Figure 3.11: Dispersion diagram of a resonance-balanced Lorentz/Drude metamaterial. Solid line: $\alpha = 0$, i. e., the limiting case of the double Drude dispersion case, dashed line: limiting case $\alpha = 1$. Intermediate values $0 < \alpha < 1$ shown shaded grey.

The dispersion relation (3.5) for (3.27) is shown in Fig. 3.11 for different values of $\alpha = \Omega_{\infty,\mu}^2/\Omega_0^2$. Double Drude dispersion is the limiting case $\alpha = 0$ with $\Omega_{\infty,\mu} = 0$, and due to (3.26) the case $\alpha = 1$ describes the other limiting case $\Omega_{0,\mu} = 0$.

In the vicinity of the Γ-point the Bloch impedance of a 'T'-configuration is given by

$$Z_{\text{Bloch,bal},\Gamma} = \sqrt{Z/Y} \cdot \cos \frac{1}{2}\chi = \sqrt{\frac{\mu_0 \mu_\infty}{\epsilon_0 \epsilon_\infty}} \frac{\Omega}{\sqrt{\Omega^2 - \Omega_{\infty,\mu}^2}} \cdot \cos \frac{1}{2}\chi \qquad (3.28)$$

which is not constant to first order around $\Omega = \Omega_0$. As impedance matching is determined by the Bloch impedance, the pole $\Omega_{\infty,\mu}$ determines the bandwidth over which matching can be obtained.

In summary, also with Lorentz/Drude metamaterials resonance-balanced designs can be obtained. The position of the pole of the Lorentz dispersive element determines the bandwidth of operation as well as the bandwidth of matching. The limiting case of Drude dispersion is both favourable with respect to bandwidth of eigenmodes as well as with respect to impedance matching. This limit is approached for tight coupling of adjacent resonant elements of the metamaterial. In comparison with a double Drude metamaterial physical implementations, the

mixed Lorentz/Drude metamaterial case is more challenging to design, because the impedance matching condition and the resonance-balance condition require the tuning of an additional resonance.

3.2 Scattering Matrix Representation of Metamaterial Cells

While in Sect. 3.1 the discretisation by means of a *finite-difference* scheme to the wave equation was performed in order to derive the foundation of metamaterials, now a *scattering matrix* based approach is presented. This approach will prove useful for the extension to multi-dimensional metamaterials in Chapters 4, 5, and 6.

The scattering matrix of a transmission line segment of length Δz normalised to its characteristic impedance Z_0 is

$$\mathbf{S} = \exp(-\mathrm{j}\phi) \begin{pmatrix} 0 & 1 \\ 1 & 0 \end{pmatrix} = \exp(-\mathrm{j}\phi)\ (\mathbf{1} - \mathbf{I}) \qquad (3.29)$$

where ϕ is the phase shift across a segment, $\mathbf{I}$ denotes the identity matrix, and $\mathbf{1}$ is a matrix with all elements equal to 1, all matrices having dimension $\langle 2 \times 2 \rangle$. Converting $\mathbf{S}$ into impedance matrix representation yields

$$\mathbf{Z} = -\mathrm{j}Z_0 \begin{pmatrix} \frac{1}{\tan\phi} & \frac{1}{\sin\phi} \\ \frac{1}{\sin\phi} & \frac{1}{\tan\phi} \end{pmatrix} \qquad (3.30)$$

The aim is to find network circuits realising (3.30). The circuits depicted in Fig. 3.1 model a segment of a one-dimensional material. We note that such a one-dimensional material is equivalent to a transmission line. The symmetrised unit cells in 'T'- and 'Π'-configuration shown in Fig. 3.1(b,c) have the impedance matrix representation and admittance matrix representation, respectively

$$\mathbf{Z} = \tfrac{1}{2}Z \cdot \mathbf{I} + \frac{1}{Y} \cdot \mathbf{1} \qquad (3.31a)$$

$$\mathbf{Y} = \tfrac{1}{2}Y \cdot \mathbf{I} + \frac{1}{Z} \cdot \mathbf{1} \qquad (3.31b)$$

Equating (3.31a) and (3.30) yields

$$Z/Z_0 = \mathrm{j}2\tan\tfrac{1}{2}\phi \qquad\qquad Y \cdot Z_0 = \mathrm{j}\sin\phi \qquad (3.32)$$

Equating (3.31b) with the inverse of (3.30) yields the same result as (3.32). The reason for this is that periodic continuations of Fig. 3.1(b) and (c) match. In the
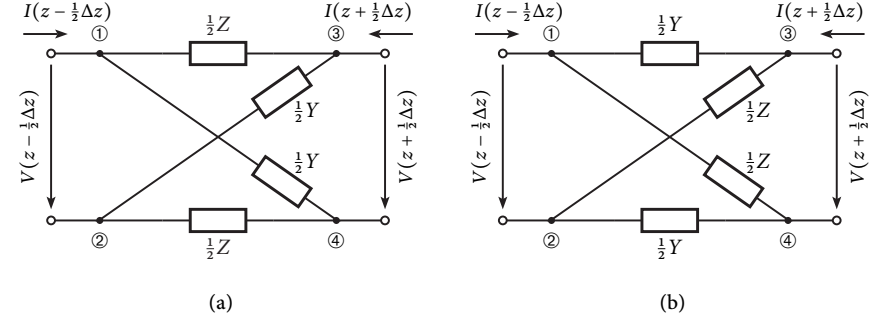

Figure 3.12: (a) All-pass equivalent circuit for a loss-less TEM transmission line of length Δz. (b) Unit cell with exchanged elements $\tfrac{1}{2}Z$ and $\tfrac{1}{2}Y$.

following Chapters 4 and 5 it will be seen that in the multi-dimensional cases the impedance and admittance representations yield independent network topologies.

A first order Taylor expansion in $\phi \propto \omega$ of (3.32) yields the expected result of a series inductance and a shunt capacitance. This is the well-known ladder-network approximation of a short piece of transmission line. Certain types of dispersion, which for example yield metamaterial behaviour, can then be implemented as discussed in Sect. 3.1.1. In summary, a scattering matrix based approach enables an abstract view on network topologies for metamaterial cells.

3.2.1 Higher Order Discretisation

In the last section it was shown that using a scattering matrix based approach the ladder network approximation to transmission lines can be explained. In this section the scattering matrix based approach is used to analyse further discretisation schemes.

The right hand side of the discretisation scheme in (3.4) is asymmetric because it only depends on the position z, but not the position $z + \Delta z$. Symmetrising this scheme yields

$$V(z + \tfrac{1}{2}\Delta z) - V(z - \tfrac{1}{2}\Delta z) = -Z \cdot \tfrac{1}{2}\big[I(z + \tfrac{1}{2}\Delta z) + I(z - \tfrac{1}{2}\Delta z)\big] \qquad (3.33a)$$

$$I(z + \tfrac{1}{2}\Delta z) - I(z - \tfrac{1}{2}\Delta z) = -Y \cdot \tfrac{1}{2}\big[V(z + \tfrac{1}{2}\Delta z) + V(z - \tfrac{1}{2}\Delta z)\big] \qquad (3.33b)$$

The network circuit describing this discretisation scheme is shown in Fig. 3.12(a),

and the impedance matrix representation is

$$\mathbf{Z} = \frac{1}{Y} \begin{pmatrix} 1 & 1 \\ 1 & 1 \end{pmatrix} + \frac{1}{4} Z \begin{pmatrix} 1 & -1 \\ -1 & 1 \end{pmatrix} \tag{3.34}$$

Comparing (3.34) and (3.30) yields

$$Z \cdot Z_0^{-1} = Y \cdot Z_0 = j2 \tan \tfrac{1}{2}\phi \tag{3.35}$$

A continuous fraction expansion of the tangent in (3.35) yields that – different from (3.32) – higher order approximations to a transmission line can be implemented using physical lumped elements.

Let us discuss the suitability of this topology for metamaterials. The dispersion relation and Bloch impedance are obtained by applying the chain matrix approach of Appendix A.5.1. One obtains

$$\cos \chi = \frac{4 + ZY}{4 - ZY} \qquad \to \qquad \tan^2 \tfrac{1}{2}\chi = -\tfrac{1}{4}ZY \tag{3.36a}$$

$$Z_{\text{Bloch}} = \sqrt{Z/Y} \tag{3.36b}$$

A pass-band exists for

$$\arg\{Z\} = \arg\{Y\} = \pm\tfrac{1}{2}\pi \tag{3.37}$$

yielding a positive, real Bloch impedance and a real phase shift χ. Thus Z and Y are purely imaginary and have the same sign, i.e., if one element behaves inductively, the other needs to behave capacitively. All-pass behaviour is achieved if in addition the Bloch impedance is frequency independent, hence if

$$\partial_\omega(Z/Y) = 0 \tag{3.38}$$

is fulfilled. Contrary to (3.7) this is possible because the Bloch impedance in (3.36b) is independent of χ. As an example, take Z as being an inductor and Y a capacitor, or, more generally, for a loss-less element and its dual [Russer, 2006]. Inserting $Z = j\omega L$ and $Y = j\omega C$ into (3.36a) and defining the normalised frequency $\Omega^2 = \omega^2 LC$ we obtain

$$\chi = 2 \arctan\left(\tfrac{1}{2}\Omega\right) \tag{3.39}$$

A low-pass to high-pass transformation $j\Omega \to (j\Omega)^{-1}$ yields

$$\chi = -2 \arctan\left(2\Omega^{-1}\right) = 2 \arctan\left(\tfrac{1}{2}\Omega\right) \pm \pi \tag{3.40}$$

Comparing (3.39) and the right-hand side of (3.40) one notes that the phases only differ by the frequency independent constant π. This is due to the topology of the circuit shown in Fig. 3.12, upon low-pass to high-pass transformation it transforms into the same circuit with the port terminals on one side flipped, see node ③ and ④ in Fig. 3.12(b). This flip does not impact the dispersion behaviour, from network theory point of view it is just a transformer with $1 : -1$ ratio. However, a transformer connected to a right-handed transmission line cannot be expected to yield a left-handed line.

Let us focus now on the general properties of all-pass circuits without port flips and their suitability for the synthesis of left-handed metamaterials. The phase of an all-pass with zeros at $(\sigma_\mu + j\omega_\mu)$ is given by [Schüßler, 1990] as

$$\chi = \pm\pi + 2 \sum_\mu \arctan\left(\frac{\omega - \omega_\mu}{\sigma_\mu}\right) + \pi \sum_\mu \text{sign}(\omega - \omega_\mu) \tag{3.41}$$

which is a monotonically increasing function of ω with $\phi(\omega = 0) = 0$. This enforces all-pass circuits to behave in a right-handed way and rules out all-pass circuits as the basis to left-handed metamaterials.

4 Two-Dimensional Metamaterials

In Sect. 3.2 we showed that a scattering matrix based representation of a metamaterial cell can be used to describe metamaterial structures. In this chapter the two-dimensional case is considered. A scattering matrix $\mathbf{S}$ is sought which describes a fully symmetric, reciprocal and loss-less four-port, a pair of ports for each direction of space. The non-trivial solution is

$$\mathbf{S} = \tfrac{1}{2}\exp(-\mathrm{j}\phi)\,(\mathbf{1} - 2\cdot\mathbf{I}) \qquad (4.1)$$

using the definition of ϕ, $\mathbf{I}$, and $\mathbf{1}$ given in Sect. 3.2, all matrices having dimension $\langle 4 \times 4 \rangle$. In fact, (4.1) is the foundation of the two-dimensional space-discretising numerical scheme TLM [Itoh, 1989]. Like in Sect. 3.2, a lumped element representation can be obtained by converting to impedance or admittance matrix representation and doing a first-order expansion of ϕ. This yields

$$\mathbf{Z}_{\text{shunt}} = \tfrac{1}{2}Z\cdot\mathbf{I} + \frac{1}{Y}\cdot\mathbf{1} \qquad (4.2a)$$

$$\mathbf{Y}_{\text{series}} = \tfrac{1}{2}Y\cdot\mathbf{I} + \frac{1}{Z}\cdot\mathbf{1} \qquad (4.2b)$$

The network topologies described by (4.2a) and (4.2b) are shown in Fig. 4.1: The *shunt node configuration* describes the TM polarisation in 2D space, the *series node configuration* describes the TE polarisation [Itoh, 1989].

Performing a dispersion analysis by applying Floquet boundary conditions as outlined in Appendix A.5.3, one obtains for both types of configurations

$$\sin^2\tfrac{1}{2}\chi + \sin^2\tfrac{1}{2}\eta = -\tfrac{1}{4}ZY \qquad (4.3)$$

with χ and η being the phase shifts observed by a wave traversing the cell along the x- and y-axis, respectively. The dispersion diagram[1] to (4.3) is shown in Fig. 4.2 for the resonance-balanced case and resonance-unbalanced case. In particular in the vicinity of the Γ-point the difference between both cases is apparent. There, the

---

1 Appendix A.2 contains an introduction to the concept of the Brillouin zone, appendix A.3 an introduction on dispersion diagrams describing multi-dimensional structures.
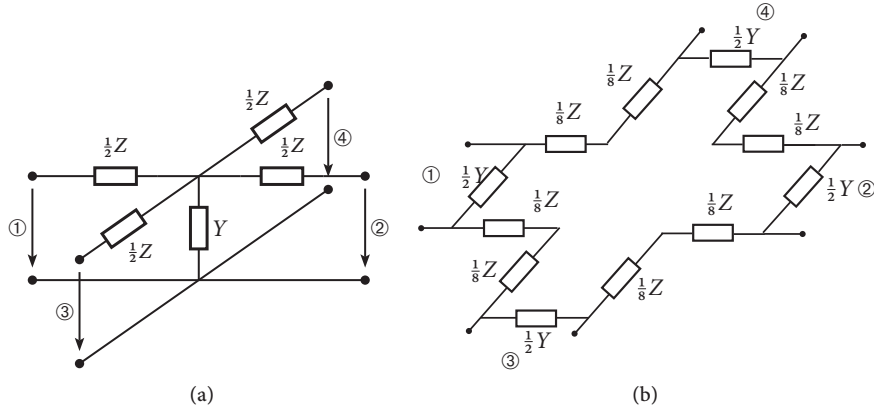
Figure 4.1: Lumped element implementations of the 2D TLM scattering matrix. (a) shunt node configuration, (b) series node configuration.

unit cell behaviour matches the one-dimensional double Drude one-dimensional metamaterial discussed in Sect. 3.1.2. If the unit cell is small compared to the wavelength, a Taylor expansion of the dispersion relation in χ, η can be performed, in analogy to the one-dimensional case discussed in (3.6):

$$\chi^2 + \eta^2 = -ZY \tag{4.4}$$

The symmetry of (4.4) in χ, η shows that the network permits physical realisations with isotropic effective material parameters. Physical realisations of the shunt-node structure yielding Drude dispersion are, e.g., mushroom structures [Sievenpiper et al., 1999, Stickel et al., 2007] and their derivatives, including anisotropic variations [Balmain et al., 2003]. The series-node structure was analysed in [Iyer and Eleftheriades, 2006]. Both types of structures can be stacked to yield so-called 'volumetric' metamaterials [Iyer and Eleftheriades, 2008, Stickel et al., 2007]. Two-dimensional arrangements of split-ring/wire grid setups [Shelby et al., 2001] are physical realisations of Lorentz dispersion for the permeability within the shunt node configuration.

In summary, the two-dimensional materials proposed in literature can be considered physical realisations of a scattering matrix based discretisation scheme.
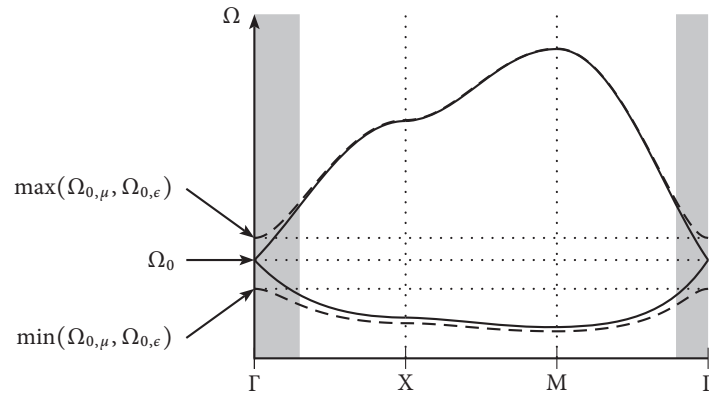

Figure 4.2: Dispersion diagram to Eq. (4.3) for double Drude elements. Solid line: resonance-balanced case, dashed line: resonance-unbalanced case. The vicinity of the Γ-point, i.e., the metamaterial range shaded grey.

5 Three-Dimensional Scalar Metamaterials

In analogy to the derivations in the two-dimensional case presented in chapter 4, now three-dimensional scalar (i. e., supporting one polarisation) metamaterials are analysed: A scattering matrix $\mathbf{S}$ is sought that represents a symmetric, reciprocal and loss-less six-port, a pair of ports for each direction of space. Due to the fact that for each direction of space only a pair of ports exists, this structure is of scalar nature, i. e., only one polarisation experiences metamaterial behaviour. The non-trivial solution for $\mathbf{S}$ is

$$\mathbf{S} = \tfrac{1}{3}\exp(-\mathrm{j}\phi)\,(\mathbf{1} - 3\cdot\mathbf{I}) \tag{5.1}$$

Conversion to impedance and admittance matrices yields

$$\mathbf{Z}_{\mathrm{shunt}} = \tfrac{1}{2}Z\cdot\mathbf{I} + \frac{1}{Y}\cdot\mathbf{1} \tag{5.2a}$$

$$\mathbf{Y}_{\mathrm{series}} = \tfrac{1}{2}Y\cdot\mathbf{I} + \frac{1}{Z}\cdot\mathbf{1} \tag{5.2b}$$

Performing a dispersion analysis by applying Floquet boundary conditions as outlined in Appendix A.5.3, one obtains for both (5.2a) and (5.2b)

$$\sin^2 \tfrac{1}{2}\chi + \sin^2 \tfrac{1}{2}\eta + \sin^2 \tfrac{1}{2}\xi = -\tfrac{1}{4}ZY \tag{5.3}$$

with χ, η, and ξ being the phase shifts observed by a wave traversing the cell along the x-, y-, and z-axis, respectively. The dispersion diagram[1] to (5.3) is shown in Fig. 5.1 for the resonance-balanced case and the resonance-unbalanced case. For in-plane propagation, i. e., $\xi = 0$ the behaviour equals that of the two-dimensional structure in chapter 4. The vicinity of the R-point shows no modes that interfere with the two modes in the vicinity of the Γ-point. In analogy to (3.6) and (4.4), performing a second order Taylor expansion of χ, η, and ξ in (5.3) yields

$$\chi^2 + \eta^2 + \xi^2 = -ZY \tag{5.4}$$

The symmetry of (4.4) in χ, η, and ξ shows that the network permits physical realisations with isotropic effective material parameters.
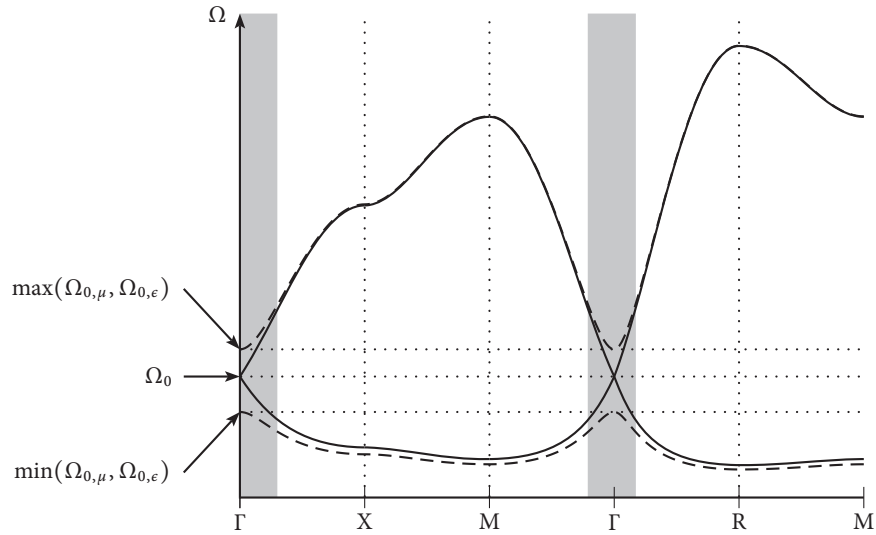
Figure 5.1: Dispersion diagram to Eq. (5.3) for double Drude elements. Solid line: resonance-balanced case, dashed line: resonance-unbalanced case. The vicinity of the Γ-point, i. e., the metamaterial range shaded grey.
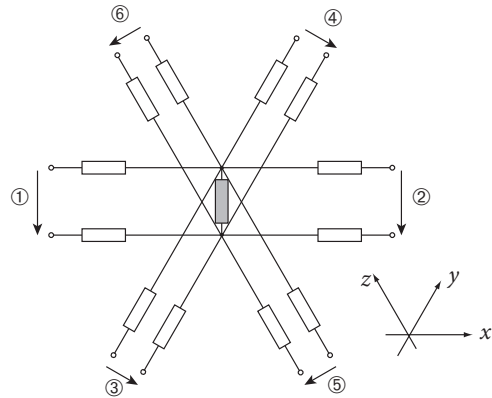

Figure 5.2: Shunt node configuration of the scalar three-dimensional metamaterial. Shunt element Y shown filled in gray, series elements $\frac{1}{2}Z$ shown unfilled.
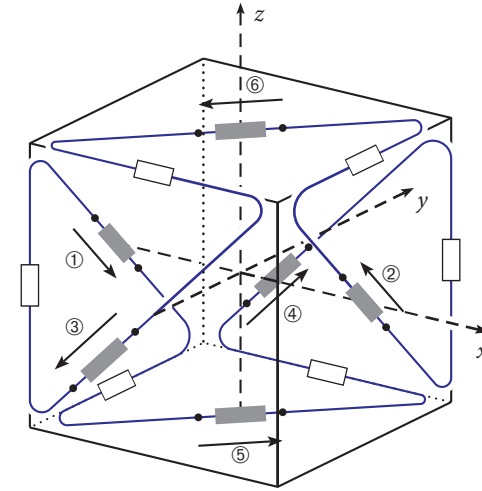

Figure 5.3: Series node configuration of the scalar three-dimensional metamaterial implementing (5.2b). Shunt elements $\frac{1}{2}Y$ shaded in grey, series elements $\frac{1}{6}Z$ interconnecting shunt elements unfilled. Two adjacent cells are connected at the ports spanning over the shunt elements, denoted by circled figures.

A metamaterial based on the topology described by (5.2a) is shown in Fig. 5.2 and was first proposed in [Alitalo et al., 2006c], yielding the three-dimensional *shunt configuration*. A physical realisation yielding Drude dispersion for $\epsilon_{\text{r,eff}}$ and $\mu_{\text{r,eff}}$ was experimentally verified in [Alitalo et al., 2006a]. Yet, physical realisations of this configuration cannot fulfill cubic or tetrahedral point group symmetries, making isotropic designs challenging.

A network representation of (5.2b) is depicted in Fig. 5.3 and in a graphically flattened representation in Fig. 5.4. It is a *series configuration* of shunt elements $\frac{1}{2}Y$ and series elements $\frac{1}{6}Z$ along a closed loop. Ports ① to ⑥ span across shunt elements. This loop of elements is wrapped around a cube symmetrically, exposing the ports at the faces of the unit cell. Coupling to adjacent cells is accomplished through these ports.

---

1 Appendix A.2 contains an introduction to the concept of the Brillouin zone, Appendix A.3 an introduction on dispersion diagrams describing multi-dimensional structures.
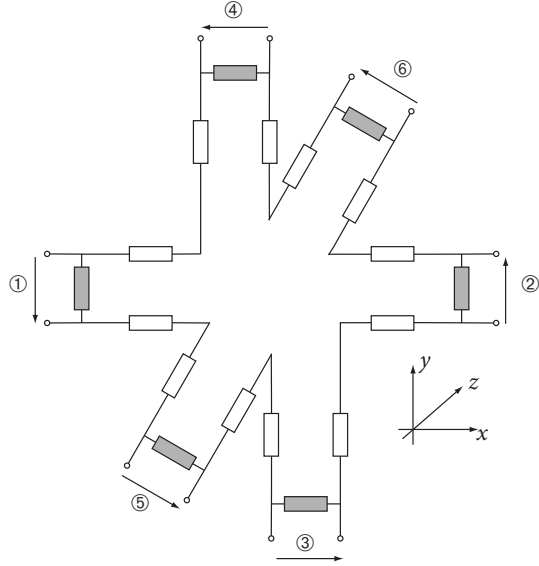
Figure 5.4: Graphically flattened representation of Fig. 5.3.

5.1 Physical Realisation of the Series Configuration

A physical realisation using solely distributed elements and yielding Drude dispersion for $\epsilon_{\text{r,eff}}$ and $\mu_{\text{r,eff}}$ is shown in Fig. 5.5. The cube is decomposed into six partially metallised pyramids, each having a thin strip running diagonally along a pyramid's base (realising $\frac{1}{2}Y$), and two plates separated by a gap. Each plate forms with the neighbouring pyramid's plate a parallel plate capacitor, realising $\frac{1}{6}Z$. Neighbouring cells are directly connected so that inductive strips are shared between cells. The structure's geometry fulfills the symmetry of the point group T_h [Ashcroft, 1988], following Schönflies notation. This point group is defined as having inversion symmetry and $4_x \cdot 4_y$ symmetry, where n_p is the n-fold rotation around the p-axis, describing rotations along diagonals of the cube. The T_h symmetry ensures isotropic behaviour of the cell in the vicinity of the Γ-point [Padilla, 2007, Baena et al., 2007].
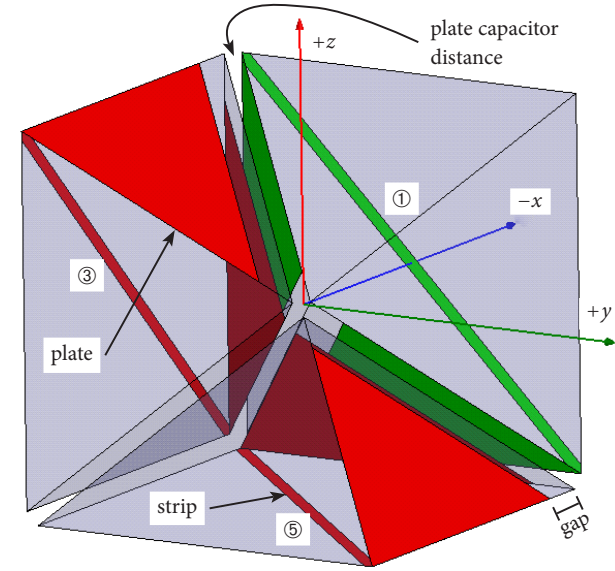

Figure 5.5: Realisation of a scalar three-dimensional metamaterial in series configuration, three of six partially surface-metallised pyramids shown, the remaining three pyramids are determined by inversion symmetry. Port labels and axis definitions correspond to Fig. 5.3. For better visibility, two pyramid's metallisations shown in red, one pyramid's metallisation in green.

5.2 Full-Wave Simulation

Full-wave simulations were carried out using the commercial FEM package Ansoft HFSS. The geometry parameters used in the simulation are: unit cell size 20 mm, plate capacitor distance 280 µm, separation gap between capacitor plates 2 mm, inductor strip width 270 µm. No dielectric was included in the simulation, conductors had copper conductivity $5.8 \cdot 10^7 \, (\Omega\text{m})^{-1}$.

The complete irreducible Brillouin zone of a structure fulfilling the T_h point group is shown in Fig. 5.6[1]. Full-wave eigenmode results for the Γ–X part of the Brillouin zone are shown in Fig. 5.7. The lowest two eigenmodes correspond to perturbed plane wave modes [Tsukerman, 2008], which have their origin at

---

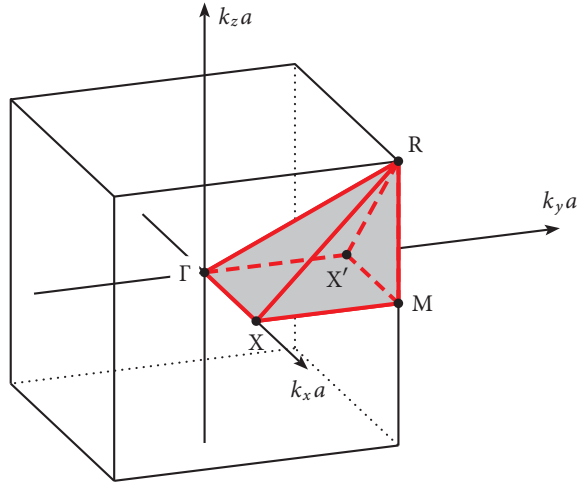1   Appendix A.2 contains an introduction to the concept of the Brillouin zone.

Figure 5.6: Irreducible Brillouin zone of a lattice with tetrahedral symmetry (T_h point group in Schönflies notation).
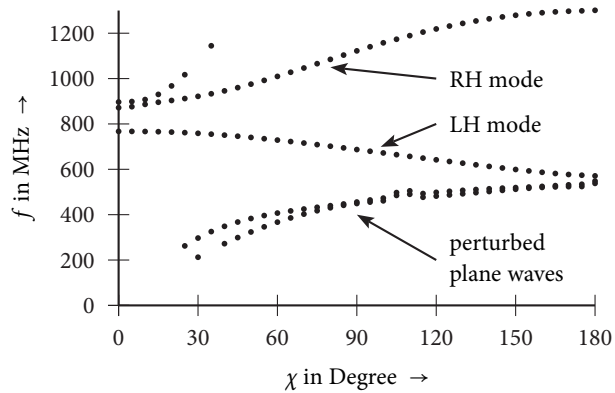

Figure 5.7: Dispersion diagram obtained by full-wave eigenmode simulation using the commercial FEM package Ansoft HFSS. Each dot represents a numerical solution.

($k = 0, f = 0$). A left-handed band extends from 570 MHz up to the electric plasmon resonance frequency 767 MHz, yielding a 30 % relative bandwidth of left-handed operation. At the magnetic plasmon resonance frequency 872 MHz a right-handed band starts, extending up to 1301 MHz. An additional mode not predicted by network theory spans the right-handed mode, but the frequency range of left-handed operation is mono-modal. Quality factors of the left-handed eigenmodes are $\approx$ 80. For the frequency range of left-handed operation the unit cell size is smaller than $\lambda/20$, fulfilling the common metamaterial definitions [Eleftheriades and Balmain, 2005, Engheta and Ziolkowski, 2006, Caloz and Itoh, 2006].

It is important to note that this three-dimensional isotropic metamaterial only supports one polarisation, as can be seen both from the derivation as well as the full-wave simulations, in which the left-handed and right-handed modes are not degenerated. Anisotropy of the structure can easily be achieved by varying the strips and plates of each of the six pyramids making up a unit cell, or by compressing the unit cell unevenly along different principal axes.

A discussion of fabrication techniques suitable for this type of unit cell can be found in Sect. 7.1.3.

Concluding this chapter, an attempt to possible further investigations shall be made. Comparing (3.29), (4.1), and (5.1), all scattering matrices follow

$$\mathbf{S} = \exp(-\mathrm{j}\phi)\left(n^{-1}\,\mathbf{1}^{\langle 2n \times 2n \rangle} - \mathbf{I}^{\langle 2n \times 2n \rangle}\right) \tag{5.5}$$

with n being the dimension of space. Eq. (5.5) is symmetric, reciprocal and unitary for arbitrary n, possibly allowing for further metamaterial structure synthesis.

6 Three-Dimensional Vectorial Metamaterial based on the RTLM Method

While in the previous Chapter 5 scalar three-dimensional metamaterial structures were discussed, this section treats a vectorial structure, i. e., a structure that supports propagation of two polarisations. Foundation to this structure is the symmetric condensed node (SCN) TLM representation of discrete electrodynamics, which contains all the information of the discretised Maxwell's equations [Hoefer, 1989, Russer, 2006, Kron, 1943, Krumpholz and Russer, 1994].

6.1 Derivation of the RTLM Computational Method by Symmetry Analysis

In the SCN-TLM computational method space is discretised into cubes. At the centre of each cube face the tangential electromagnetic field is sampled, as shown in Fig. 6.1(a). This yields 12 electric and 12 magnetic field components which may be represented by 12 incident waves with amplitudes $a_1, \ldots, a_{12}$ and 12 scattered waves with amplitudes $b_1, \ldots, b_{12}$ [Krumpholz and Russer, 1994, Russer, 1996], depicted in Fig. 6.1(b). The circuit representation of the TLM cell may be depicted by a 12-port as shown in Fig. 6.1(c). It is represented by a scattering matrix $\mathbf{S}$ which was first proposed in [Johns, 1987]. A method-of-moments based derivation of the SCN-TLM cell from Maxwell's equation was presented in [Krumpholz and Russer, 1994]. Here a derivation solely based on symmetry considerations is performed, in analogy to the discussion in Chapters 4 and 5.

A scattering matrix $\mathbf{S} \in \mathbb{C}^{\langle 12 \times 12 \rangle}$ describing a general 12-port has 144 coefficients s_{ij}. The particular 12-port shown in Fig. 6.1(c) fulfills rotation and mirror symmetries with respect to the x-, y-, and z-axes, which inter-relates the coefficients s_{ij}. The matrix fulfilling these symmetries has the form

$$\mathbf{S} = \exp(-j\phi) \begin{pmatrix} \mathbf{S}_A & \mathbf{S}_B & \mathbf{S}_B^T \\ \mathbf{S}_B^T & \mathbf{S}_A & \mathbf{S}_B \\ \mathbf{S}_B & \mathbf{S}_B^T & \mathbf{S}_A \end{pmatrix} \qquad (6.1a)$$
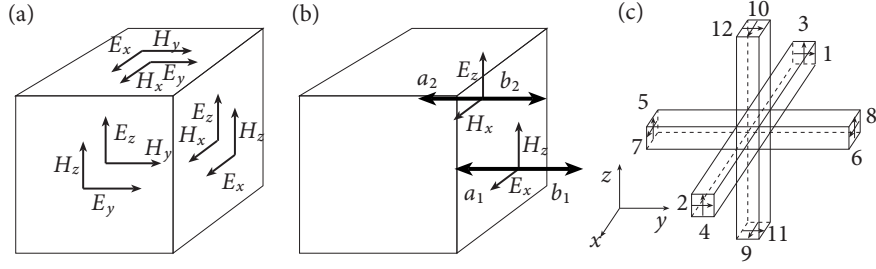
Figure 6.1: (a) TLM cell, tangential electromagnetic fields are sampled at the centre of each cube face, (b) corresponding wave amplitudes, and (c) symmetric condensed node.

with

$$
\mathbf{S}_A = \begin{pmatrix} \rho & \tau_1 & 0 & 0 \\ \tau_1 & \rho & 0 & 0 \\ 0 & 0 & \rho & \tau_1 \\ 0 & 0 & \tau_1 & \rho \end{pmatrix} \qquad \mathbf{S}_B = \begin{pmatrix} 0 & 0 & \tau_2 & -\tau_2 \\ 0 & 0 & -\tau_2 & \tau_2 \\ \tau_3 & \tau_3 & 0 & 0 \\ \tau_3 & \tau_3 & 0 & 0 \end{pmatrix} \tag{6.1b}
$$

Assuming matched ports ($\rho = 0$), a loss-less node ($\mathbf{S}^\dagger = \mathbf{S}^{-1}$), and equal phase delay in all branches ($\arg \tau_1 = \arg \tau_2 = \arg \tau_3$, $\mathbf{S}_A, \mathbf{S}_B \in \mathbb{R}^{\langle 4 \times 4 \rangle}$) one obtains the two solutions

$$
\tau_1 = 0 \qquad\qquad \tau_2 = \tau_3 = \tfrac{1}{2} \tag{6.2a}
$$

$$
\tau_1 = 1 \qquad\qquad \tau_2 = \tau_3 = 0 \tag{6.2b}
$$

Eq. (6.2b) describes a trivial node not connected to off-axis adjacent nodes and is thus not of further interest. Eq. (6.2a) describes a general space-discretising cell, the SCN-TLM node. Inspecting (6.1) and (6.2b) one notes that ports on opposite faces of Fig. 6.1 are uncoupled. The expression $\exp(-\mathrm{j}\phi)$ in (6.1) can be interpreted as being the phase delay across the unit cell.

In order to be able to synthesise a metamaterial, i. e., a physical realisation of the computing scheme, a transformation of the symmetric condensed node TLM scheme needs to be applied. The 12-port cell can be decomposed into two independent six-ports $\tilde{\mathbf{S}}$ and $-\tilde{\mathbf{S}}$ by the following coordinate transformation [Wlodarczyk, 1992, Russer, 1996]

$$
\mathbf{Q}^T \cdot \mathbf{S} \cdot \mathbf{Q} = \begin{pmatrix} \tilde{\mathbf{S}} & 0 \\ 0 & -\tilde{\mathbf{S}} \end{pmatrix} \tag{6.3a}
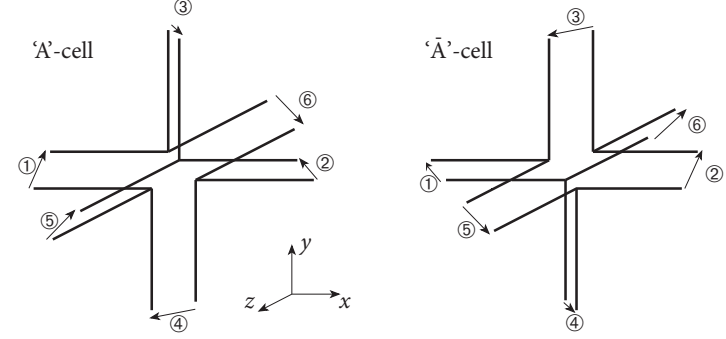$$

Figure 6.2: RTLM half unit cells 'A' and 'Ā' implementing $\tilde{\mathbf{S}}$. The complete unit cell is constituted by both half cells merged together.

with the matrix $\mathbf{Q}$ describing the change of bases

$$
\mathbf{Q} = \frac{1}{\sqrt{2}}
\begin{bmatrix}
+1 & 0 & +1 & 0 & 0 & 0 & 0 & 0 & 0 & 0 & 0 & 0 \\
0 & +1 & 0 & -1 & 0 & 0 & 0 & 0 & 0 & 0 & 0 & 0 \\
0 & 0 & 0 & 0 & +1 & 0 & +1 & 0 & 0 & 0 & 0 & 0 \\
0 & 0 & 0 & 0 & 0 & +1 & 0 & -1 & 0 & 0 & 0 & 0 \\
0 & 0 & 0 & 0 & 0 & 0 & 0 & 0 & +1 & 0 & +1 & 0 \\
0 & 0 & 0 & 0 & 0 & 0 & 0 & 0 & 0 & +1 & 0 & -1 \\
+1 & 0 & -1 & 0 & 0 & 0 & 0 & 0 & 0 & 0 & 0 & 0 \\
0 & +1 & 0 & +1 & 0 & 0 & 0 & 0 & 0 & 0 & 0 & 0 \\
0 & 0 & 0 & 0 & +1 & 0 & -1 & 0 & 0 & 0 & 0 & 0 \\
0 & 0 & 0 & 0 & 0 & +1 & 0 & +1 & 0 & 0 & 0 & 0 \\
0 & 0 & 0 & 0 & 0 & 0 & 0 & 0 & +1 & 0 & -1 & 0 \\
0 & 0 & 0 & 0 & 0 & 0 & 0 & 0 & 0 & +1 & 0 & +1
\end{bmatrix}
\tag{6.3b}
$$

This corresponds to a rotation of the polarisations by 45° at each face of the discretisation cube, as shown in Fig. 6.2. The transformed scattering matrix $\tilde{\mathbf{S}}$ is

$$
\tilde{\mathbf{S}} = \exp(-\mathrm{j}\phi) \begin{pmatrix} \mathbf{0} & \tilde{\mathbf{S}}_0 & \tilde{\mathbf{S}}_0^T \\ \tilde{\mathbf{S}}_0^T & \mathbf{0} & \tilde{\mathbf{S}}_0 \\ \tilde{\mathbf{S}}_0 & \tilde{\mathbf{S}}_0^T & \mathbf{0} \end{pmatrix} \qquad \tilde{\mathbf{S}}_0 = \tfrac{1}{2} \begin{pmatrix} -1 & -1 \\ 1 & 1 \end{pmatrix} \tag{6.4}
$$

The space discretisation expressed in (6.3) and (6.4) is called *rotated* TLM method (RTLM) in literature [Russer, 1996]. In this contribution the two independent half cell six-ports described by $\tilde{\mathbf{S}}$ and $-\tilde{\mathbf{S}}$ are called 'A' and 'Ā' cells, respectively. A cell that represents both polarisations at each surface can be established by either nesting the six-port structures of the 'A' and 'Ā' half cells or by a cluster of eight half cells with alternating 'A' and 'Ā' cells.
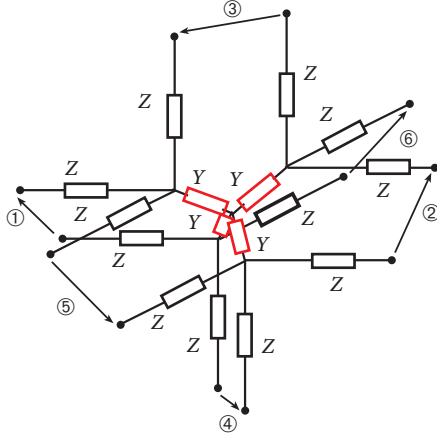
Figure 6.3: Lumped element model of a RTLM half unit cell implementing the structure shown in Fig. 6.2. Shunt elements Y shown in red, series elements denoted by Z.

6.2 The RTLM Metamaterial Unit Cell

An elementary metamaterial cell can be perceived based on RTLM cells, by inserting reactances Z in series to the six cell ports and four admittances Y connecting the series reactances at a central node which forms a *virtual ground*. The resulting network is shown in Fig. 6.3 as well as in Fig. 6.5(a) in a graphically flattened representation. The equivalence between the network of Fig. 6.3 and the six-port scattering matrix of (6.4) can be proved by calculating the impedance matrix representation of each. Indeed, both impedance matrix representations match,

$$\tilde{\mathbf{Z}}^{\langle 6\times 6\rangle} = \left(2Z + \frac{2}{Y}\right) \cdot \mathbf{I} + \frac{2}{Y} \cdot \mathbf{P} \tag{6.5}$$

with the identity matrix $\mathbf{I}$ and

$$\mathbf{P} = \begin{pmatrix} \mathbf{0} & \mathbf{P}_0 & \mathbf{P}_0^T \\ \mathbf{P}_0^T & \mathbf{0} & \mathbf{P}_0 \\ \mathbf{P}_0 & \mathbf{P}_0^T & \mathbf{0} \end{pmatrix} \qquad \mathbf{P}_0 = -\tfrac{1}{2}\begin{pmatrix} -1 & -1 \\ 1 & 1 \end{pmatrix} \tag{6.6}$$

Comparing (6.4) with (6.5), (6.6) one notes that the high level of symmetry of the scattering matrix representation of the RTLM metamaterial unit cell is preserved in
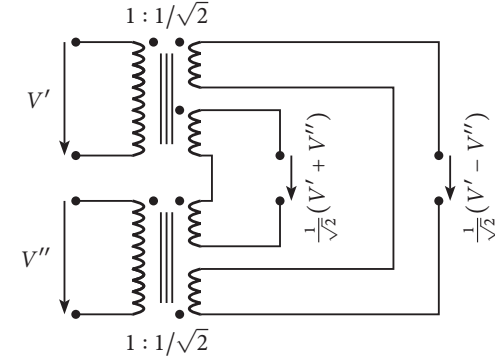
Figure 6.4: Representation of a 45° rotation of polarisation by a transformer network.

the impedance matrix representation.

As an aside it shall be noted that the rotation of polarisation by 45° at each face of the space discretising cube performed in Eq. (6.3a) can be explained using a network point of view, i.e., by means of ideal transformers, as shown in Fig. 6.4: Two unrotated ports with polarisations/port voltages V', V'' are transformed into the superposition $(V' \pm V'')/\sqrt{2}$ which describes the rotated port polarisations/voltages. Thus from a circuit theoretical point of view the SCN-TLM node can be transformed into the RTLM node by means of transformer networks.

A complete RTLM unit cell consists of two half cells which may be connected at their virtual grounds. The 'A'-cell scattering is described by $\tilde{\mathbf{S}}$ whereas the 'Ā'-cell is scattered by $-\tilde{\mathbf{S}}$, as denoted by (6.3a). This sign inversion may be interpreted as a frequency-independent phase shifter of 90° attached to each port, which is impractical for any physical realisation. For this reason we consider a metamaterial structure containing solely 'A'-cells. In this case, referring to Fig. 6.1(c), a wave incident at port 1 is scattered into ports 5, 6, 9, and 10 instead of 7, 8, 11, and 12. This means the polarisation is changed from vertical to horizontal after traversing the cell. If 'A' together with 'Ā' cells are used, then ports 2, 3, and 4 are uncoupled from port 1, as expressed by (6.1) and (6.2b). This behaviour is maintained also for the simplified cell containing solely 'A' cells.

6.3 Dispersion Behaviour

The dispersion relation of a RTLM metamaterial consisting solely of 'A'-cells is obtained by the algebraic procedure described in Appendix A.5.3 which yields

$$
\begin{aligned}
(1 + ZY)^2 &= \tfrac{1}{4}\big(3 - \cos\chi\cos\eta - \cos\chi\cos\xi - \cos\eta\cos\xi \big) \\
&= \tfrac{1}{4}\Big[\sin^2(\tfrac{1}{2}\chi + \tfrac{1}{2}\eta) + \sin^2(\tfrac{1}{2}\chi + \tfrac{1}{2}\xi) + \sin^2(\tfrac{1}{2}\eta + \tfrac{1}{2}\xi) \\
&\quad + \sin^2(\tfrac{1}{2}\chi - \tfrac{1}{2}\eta) + \sin^2(\tfrac{1}{2}\chi - \tfrac{1}{2}\xi) + \sin^2(\tfrac{1}{2}\eta - \tfrac{1}{2}\xi)\Big]
\end{aligned}
\tag{6.7}
$$

with χ, η, and ξ being the phase shifts observed by a wave traversing the cell along the x-, y-, and z-axis, respectively. Eq. (6.7) simplifies in the case of propagation along a principal axis, i. e., $\eta = \xi = 0$, to

$$
(1 + ZY)^2 = \sin^2 \tfrac{1}{2}\chi
\tag{6.8}
$$

In analogy to (3.6), (4.4), and (5.4), performing a second order Taylor expansion of (6.7) in χ, η, and ξ yields

$$
\left(\tfrac{1}{2}\chi\right)^2 + \left(\tfrac{1}{2}\eta\right)^2 + \left(\tfrac{1}{2}\xi\right)^2 = (1 + ZY)^2
\tag{6.9}
$$

The symmetry of (6.9) in χ, η, and ξ shows that this network permits physical realisations with isotropic effective material parameters.

Comparing the dispersion relation of (6.7) with that of the one-, two-, and three-dimensional scalar cases (3.5), (4.3), and (5.3), respectively, one notes that the frequency-dependent term of the RTLM metamaterial case is quadratic in ZY. This square is the cause for twice the number of frequency bands compared to (3.5), (4.3), and (5.3).

The Bloch impedance of the RTLM cell has the same structure as the Bloch impedance of the one-dimensional case in 'T'-configuration (3.7a) and reads

$$
Z_{\mathrm{Bloch}} = 2\sqrt{Z/Y}\sqrt{2 + ZY}
\tag{6.10}
$$

This indicates that there is no angular dispersion, since (6.10) is independent of χ, η, and ξ.

6.4 Propagation along Principal Axes

In order to gain better insight into wave propagation through the RTLM cell, the specific case of wave propagation along a principal axis is analysed in this section.
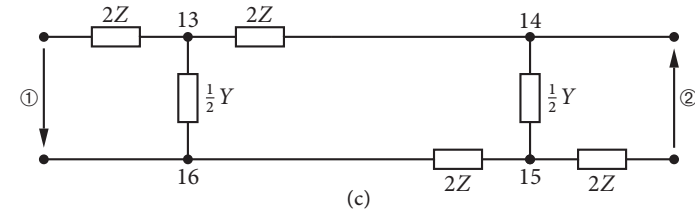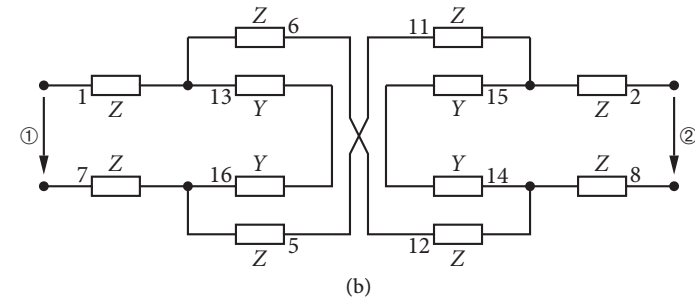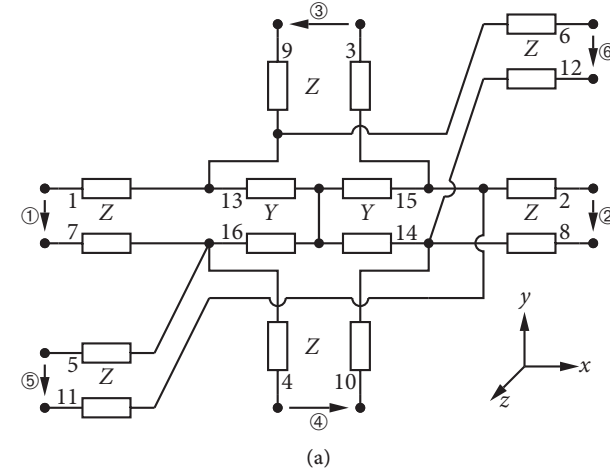

Figure 6.5: Equivalent circuits for the RTLM metamaterial half unit cell. (a) implementation of 'A'-cell. (b) particularised circuit for the case of x-axis propagation following (6.12). (c) simplified equivalent circuit of (b). Note that in figure (c) port ② is flipped.
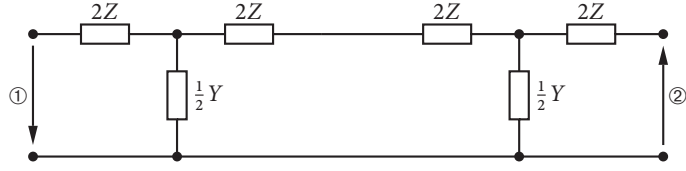
Figure 6.6: Equivalent circuits for the RTLM metamaterial half unit cell for propagation along a principal axis, simplified further from Fig. 6.5(c). Note that port ② is flipped.

In this case the equivalent circuit of Fig 6.5(a) can be simplified as follows: Propagation along the x-direction is assumed, periodic boundary conditions along the y- and z-axis are described by

$$\begin{pmatrix} b_③ \\ b_④ \end{pmatrix} = \begin{pmatrix} 0 & 1 \\ 1 & 0 \end{pmatrix} \begin{pmatrix} a_③ \\ a_④ \end{pmatrix} \qquad \begin{pmatrix} b_⑤ \\ b_⑥ \end{pmatrix} = \begin{pmatrix} 0 & 1 \\ 1 & 0 \end{pmatrix} \begin{pmatrix} a_⑤ \\ a_⑥ \end{pmatrix} \qquad (6.11)$$

with a_i and b_i being the incident and reflected wave amplitudes at port i. The scattering matrices used in (6.11) equal ideal transformers with $1:1$ transformer ratio. If in the network shown in Fig. 6.5(a) ports ③ and ④ as well as ⑤ and ⑥ are connected by ideal transformers, solving Kirchhoff's equations yields

$$i_③ = -i_④ = 0 \qquad (6.12a)$$

$$v_⑤ = v_⑥ = 0 \qquad (6.12b)$$

$$i_{13} + i_{16} = 0 \qquad\qquad i_{14} + i_{15} = 0 \qquad (6.12c)$$

where $i_{13} \dots i_{16}$ denote the currents through the shunt elements Y, the current flow in each is directed towards the symmetry centre which is a virtual ground. Hence ports ③ and ④ are open-circuited, ports ⑤ and ⑥ are short-circuited, and the shunt elements Y decouple. Following (6.12) the equivalent circuit can be particularised to Fig. 6.5(b) that can then be simplified into Fig. 6.5(c). Noting that the impedance matrix of a T-circuit and a flipped T-circuit are equal, a further simplification leads to Fig. 6.5(d). Interestingly, for one-dimensional propagation the circuit resembles that of the ladder circuit shown in Fig. 3.1(b), except that for the RTLM case there are two T-circuits per unit cell and a flip of sign at port ②.

The dispersion relation and Bloch impedance for the structure depicted in Fig. 6.6 may be shown to agree with (6.8) and (6.10), as expected.
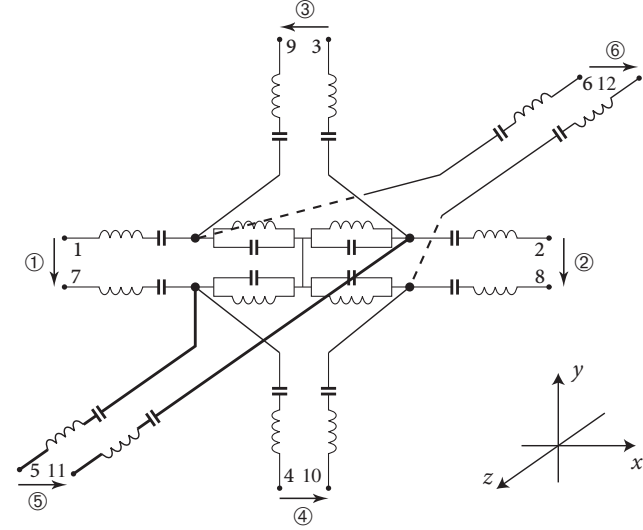

Figure 6.7: RTLM metamaterial half unit cell with Drude dispersion elements.

6.5 Implementation of Dispersion

Due to the fact that the dispersion relation (6.7) is quadratic in ZY one obtains for the RTLM metamaterial a different type of dispersion compared to Sect. 3.1.1. Anyway, in the following the term *Drude elements* will be used in analogy to Chapters 3, 4, and 5, denoting series resonators for Z and parallel resonators for Y. The dispersion diagram for double Drude elements is depicted in Fig. 6.8 for the resonance-balanced and resonance-unbalanced cases, yielding two left-handed and two right-handed bands.

The four bands, obtained by inserting the Drude elements defined in (3.8) and (3.13) into (6.7), are given by

$$\Omega^2 = \tfrac{1}{2}\left(1 + \Omega_{0,\epsilon}^2 + \Omega_{0,\mu}^2 \pm d\right) \pm \sqrt{\tfrac{1}{4}\left(1 + \Omega_{0,\epsilon}^2 + \Omega_{0,\mu}^2 \pm d\right)^2 - \Omega_{0,\epsilon}^2 \Omega_{0,\mu}^2} \quad (6.13)$$

with $d^2 = \tfrac{1}{4}(3 - \cos\chi\cos\eta - \cos\chi\cos\xi - \cos\eta\cos\xi)$. The dispersion diagram[1] to (6.13) is shown in Fig. 6.8 for both the balanced- and unbalanced-resonance cases.

---

1 Appendix A.2 contains an introduction to the concept of the Brillouin zone, Appendix A.3 an introduction on dispersion diagrams describing multi-dimensional structures.
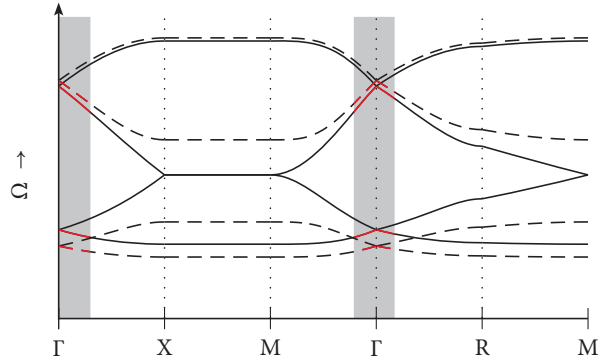
Figure 6.8: Dispersion diagram to (6.13) of the RTLM metamaterial using dou-
ble Drude elements for the balanced-resonance case (solid line) and
unbalanced-resonance (dashed line) case. Areas denoting operation
where the unit cell is small compared to the wavelength are shaded grey.
Dispersion diagram parts with left-handed behaviour are shown by red
lines.

The consequence of the suppressed negative sign in the scattering matrix of
the 'Ā'-cell (see Sect. 6.2) are as follows:

- the unbalanced-resonance gap of the dispersion diagram appears between
  the X and M points and not at the Γ-point like in the one-, two-, and three-
  dimensional scalar cases with double Drude dispersion implementation

- similarly, the frequency-independence of the Bloch impedance may be
  shown to exist near the X/M region, but not near the Γ-point.

This second consequence means that the Bloch impedance is not constant to
first order in the metamaterial frequency range (i. e., around the Γ-point) and that
therefore the bandwidth of the RTLM metamaterial is restricted. This is the conse-
quence for the simplification of the structure avoiding phase shifters in the 'Ā' cell.
This behaviour of the Bloch impedance is shown in Fig. 6.9: While for a balanced-
resonance one-dimensional double Drude structure the Γ-point corresponds to
$\Omega = \Omega_0$ and the Bloch impedance is flat, for the RTLM metamaterial this is not
the case.
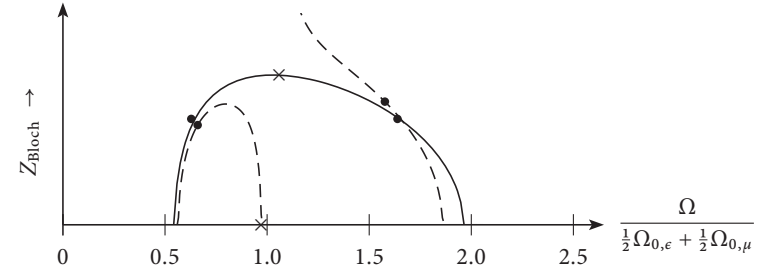

Figure 6.9: Bloch impedance of the RTLM metamaterial cell. Solid line: balanced-
resonance case, dashed line: unbalanced-resonance case. Crosses de-
note Γ-point operation for a one-dimensional double Drude structure,
dots denote Γ-point operation of the RTLM metamaterial.

6.6 Physical Realisation

A maximally symmetric physical realisation of the RTLM metamaterial with Drude
elements, corresponding to the lumped element network of Fig. 6.3 and Fig. 6.7, is
depicted in Fig. 6.10. The series elements Z are implemented by parallel plate ca-
pacitors. Together with their parasitics they form a series resonator as required for
a series Drude element. In Fig. 6.10(a) these capacitor plates are labelled by 'C'. The
capacitor is formed with the plate of the adjacent cell. Shunt elements Y are imple-
mented by wires. The inductance of each wire together with its parasitics yields
a parallel resonator, as required for a shunt Drude element. In Fig. 6.10(a) wires
are labelled by 'L'. Wires join at the centre point labelled 'G', which forms a virtual
ground due to symmetry. Both half cells may be nested with both half unit cells
being galvanically connected at their virtual ground. Two complete unit cells are
shown in Fig. 6.10(b), visualising the capacitive between the plates of adjacent unit
cells. Ports lie in the middle within each parallel plate capacitor and are arranged
diagonally, corresponding to diagonally polarised waves. This can be understood
by inspecting Fig. 6.3. Two series elements Z connect directly, and in this physical
realisation, are implemented as *one* joint capacitor. The ports in Fig. 6.3 lie between
the two series elements Z. Therefore in the physical realisation the port position
is at the plane within the capacitor, cutting it virtually in half. Fig. 6.10(c) shows a
three-dimensional rendering of a cluster of $2 \times 2 \times 2$ unit cells.
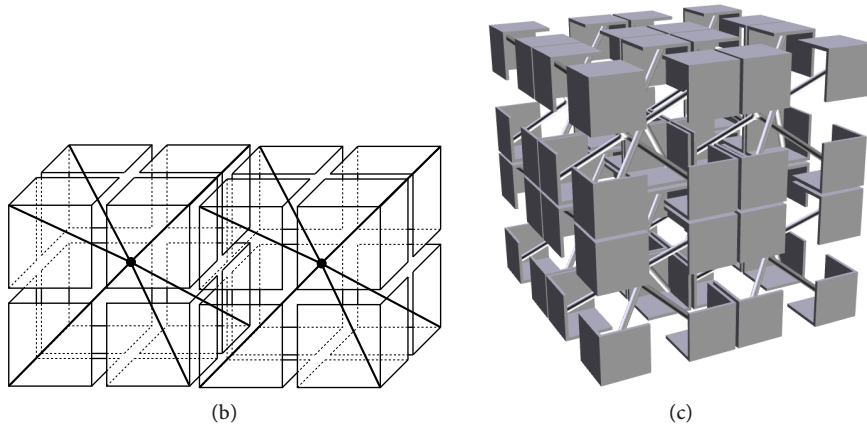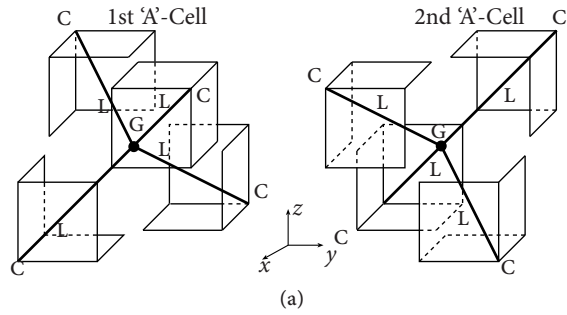
Figure 6.10: Maximally symmetric physical realisation of the RTLM metamaterial containing Drude elements. (a) 'A'-type half unit cells, (b) two nested half unit cells form a complete RTLM unit cell. Two unit cells put next to each other, visualising capacitive coupling between unit cells (c) a complete $2 \times 2 \times 2$ structure.

6.7 Parasitic Modes

Unconnected metamaterial structures may allow wave propagation of an additional mode within the structure, called 'perturbed plane wave mode' [Collin, 1990] or sometimes 'acoustic branch' because of analogy with solid state physics. In order to avoid mode splitting and coupling to this parasitic mode, the unit cell can be scaled appropriately to have the metamaterial mode and the parasitic mode reside at different frequencies [Tsukerman, 2008, Iyer and Eleftheriades, 2008]. This
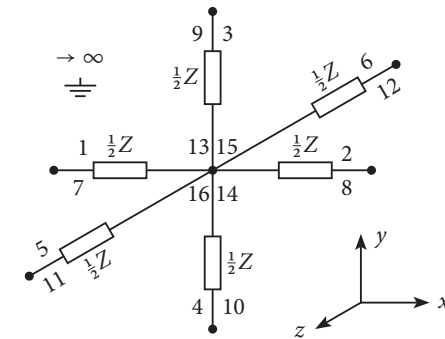

Figure 6.11: Topology of the RTLM metamaterial half unit cell for the common mode. The Node labels $1 \ldots 16$ correspond to the scheme in Fig. 6.5(a).

perturbed plane wave mode is found both in the scalar three-dimensional case as well as the RTLM case, but exists in frequency bands different from the left-handed ones, as can be seen both in Fig. 5.7 and Fig. 7.18. While the existence of this parasitic mode in a different frequency band is sufficient to maintain proper operation of the metamaterial, it would be advantageous to modify the physical realisation to inhibit the parasitic mode. The appropriate modification is so-far unknown for the RTLM metamaterial and the scalar three-dimensional structure, but recently for the two-dimensional metamaterials appropriate modifications have been proposed [Iyer and Eleftheriades, 2008, Stickel et al., 2007].

In addition to the perturbed plane waves another parasitic common mode could possibly exist for the RTLM metamaterial, because the ports in the network topology of Fig. 6.5 are fundamentally differential.

For the common mode the potentials at node n and $(n+6)$ with $1 \leq n \leq 6$ are equal, and all voltages are defined with respect to the potential at infinity. The circuit then simplifies as follows: All shunt elements Y are shorted and the structure is equal to Fig. 6.11. This network only contains one type of element, denoted with $\frac{1}{2}Z$. A network with only one type of element does not support wave propagation: Assuming that Z consists of only inductors, the lack of capacitors forbids propagating waves at all frequencies. Using frequency transformation it can be shown that no common mode exists for other network elements representing Z.
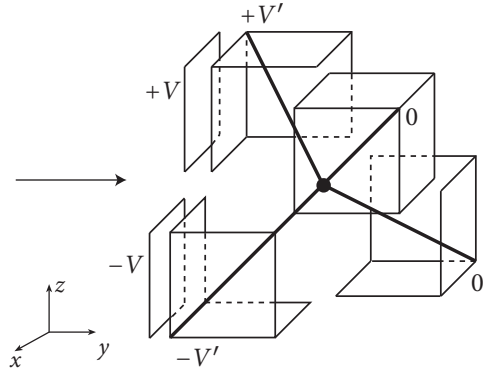
Figure 6.12: Signal propagation through the RTLM cell.

6.8 Signal Propagation through the Cell

The RTLM unit cell is a balanced structure: It has a virtual ground, i. e., a zero voltage point due to the symmetry of the structure instead of connection to a physical ground. It consists of two nested cells, as shown in Fig. 6.10(a). These two cells are electromagnetically decoupled in the sense that they support electromagnetic waves of independent orthogonal polarisations in each direction of space.

To explain wave propagation through the structure, let us consider the example of a $-xz$-polarised (electric field oriented diagonally along the $z = -x$ direction) plane (transverse) wave propagating along the y-direction and incident on the structure at the level of a unit cell.

Take the first 'A' half cell (left-hand side of Fig. 6.10(a)), displayed in Fig. 6.12. In this cell, the incident plane wave produces a symmetric voltage difference ($+V$ and $-V$) between the two patches at the input face of the half cell. These two patches form capacitors with the patches printed on the opposite faces of the thin substrate slabs, which store electric energy and provide the required series capacitance C_L corresponding to negative permeability. Due to these capacitors, the incident transverse electric field becomes locally longitudinal between the two plates of the capacitors. The voltages at the plates inside the structure are $V' = V - Z \cdot I$, where I is the current flowing into the incident port. From this point, the wave 'sees' the wire environment. Due to the symmetry of the structure and due to the symmetrical incident voltages, propagation is prohibited along the straight (y) direction since the field is short-circuited at the centre node (virtual ground), consis-

tently with the fact that the scattering parameter $\tilde{s}_{21}$ is zero in (6.4).

While propagation in axial direction is not allowed, off-axis propagation occurs through the four lateral faces of the unit cell, along the positive and negative x- and z-directions. Fig. 6.12 shows how this is realised in the three-dimensional cell as a result of the symmetry of the structure and the differential voltages leading to the voltage difference $\pm V'$ at the off-axis ports. Since the wave is deflected towards the four lateral faces in the unit cell, the magnetic flux circulates around the two wire branches extending from the corner voltage points to the virtual ground point. This corresponds to magnetic energy storage and generates the required shunt inductance L_L corresponding to negative permittivity. Note that the directions of the fields indicated in Fig. 6.12 correspond to the other four independent scattering parameters of (6.4).

Consider next the second 'A' half cell (right-hand side of Fig. 6.10(a)). In this cell, the incident $-xz$-polarised electric field does not encounter any metallisation at the input plane of the cell, which is therefore transparent to it. The plates with the same polarisation at the output plane belong to the next 'A' half cell.

When many cells are nested, 'A-A' are cascaded along the three directions of space. Plane wave propagation is obtained by meander-like scattering between unit cells, which is in agreement with the scattering-type propagation in the numerical technique TLM.

6.9 Excitation by Gaussian Beams

While Sect. 6.4 treated wave propagation along a principal axis, this section examines a circuit model of waves incident at oblique angles onto a metamaterial slab, specifically illumination by a Gaussian beam.

The circuit simulation setup is shown schematically in Fig 6.13: A super-cell consists of $(2k+1) \times 1 \times 1$ RTLM cells. Along the first direction the top and bottom cells are connected by phase shifters with a value of ϕ. This models periodic continuation of the super-cell. This phase shift can model the oblique incident case as explained below. Along the second direction ideal transformers account for periodic continuation not being capable of oblique incidence. Along the third direction ports are assigned. On one side 'transmission' ports labelled $t_{-k} \ldots t_0 \ldots t_k$, on the opposite side 'receiver' ports $r_{-k} \ldots r_0 \ldots r_k$. With this setup a Gaussian beam incident at angle θ_i onto the super-cell is modelled. Due to the periodic continuation of the super-cell the excitation is also periodically continued. Therefore the beam width must decay sufficiently towards the boundaries of the super-cell.
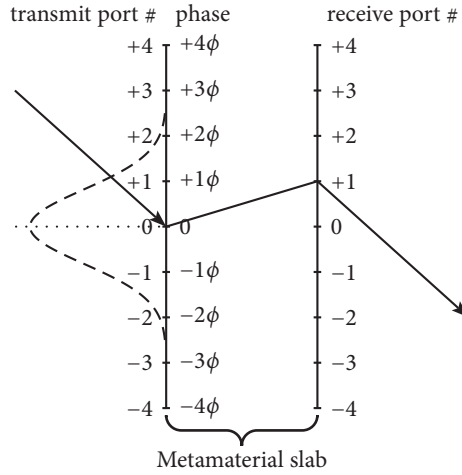
Figure 6.13: Circuit simulation setup for an incident Gaussian beam. Left side: transmission ports, ϕ is the phase shift observed at each port due to oblique incidence of the Gaussian beam. Dashed line: Amplitude of the Gaussian beam.
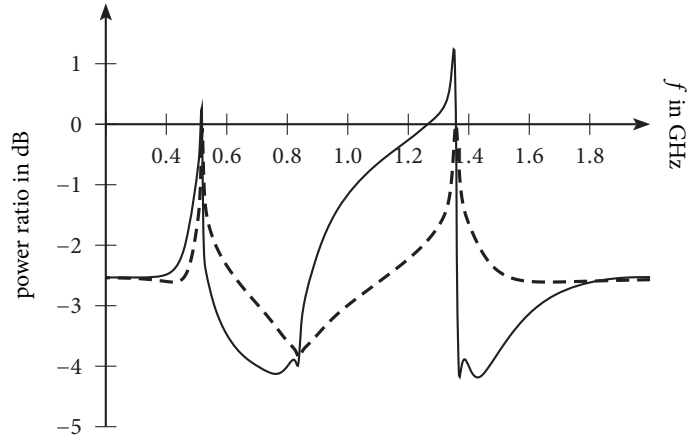

Figure 6.14: Gaussian beam simulation. Power received at port r_i denoted by P_{ri} and thus Solid line: $\frac{P_{r1}}{P_{r0}}$ for $\phi = 45°$, dashed line: $\frac{P_{r1}}{P_{r0}}$ for $\phi = 0°$. Below the Γ-point frequencies the power is directed to ports with positive port number, above the Γ-point frequencies to ports with negative port number.

This setup can be modelled using a scattering parameter simulation: The power at the receiver ports depending on the transmission ports is given by the coefficients of a scattering matrix. Weighting these coefficients with the aperture distribution due to the simulated incident Gaussian beam yields a measure of the power at each receiver port r_i

$$\sum_{n=-k}^{k} s_{r_i, t_n} \exp(-n^2) \exp(jn\phi) \qquad (6.14)$$

The result is shown for a setup with a RTLM metamaterial slab of 9 transmission and 9 receiver ports in Fig. 6.14. The lumped elements were set to $L_L = L_R = 6\,$nH, $C_R = C_L = 6\,$pF giving Γ-point frequencies 516 MHz and 1351 MHz. Below this frequency left-handed operation is expected, above right-handed operation. A phase shift $\phi > 0$ corresponds to a wave incoming from the top left, hence for left-handed operation the maximum of the output power is expected to be observed at one of the ports $r_1 \ldots r_k$, for right-handed operation the maximum of the output power is expected to be observed at one of the ports $r_{-k} \ldots r_{-1}$. Indeed this result can be observed in a simulation: Fig. 6.14 shows for 833 MHz $\leq f \leq$ 1351 MHz the solid line above the dashed line, for $f >$ 1351 MHz the solid line below the dashed line. Hence the expected refractive behaviour of the RTLM metamaterial cell is observed.

6.10 Experimental Verification

Fig. 6.15 shows the unit cell prototype of the RTLM metamaterial. The plate capacitors are realised using printed circuit boards with patches on both sides of the substrate which ensures accurate series capacitor values. The inductors are realised by rigid wires. The unit cell length is 2 cm, the substrate is Rogers 4350B with a thickness of 254 μm. The resulting values for the equivalent circuit of Fig. 6.7 are $L_L \approx 17.3\,$nH, and $C_L \approx 5.4\,$pF.

This prototype was measured using a two-port vector network analyser through baluns (microstrip to parallel-strip transitions) connected at two arbitrary non-aligned ports, while the remaining ports are terminated with $Z_L = 50\,\Omega$ resistors. Note that this excitation appropriately models wave propagation through the structure because the RTLM structure is a network with well-defined ports. For the RTLM metamaterial it suffices to verify experimentally that the metamaterial cell indeed acts like the lumped circuit of Fig. 6.5(a). In this case the behaviour of the entire structure can be inferred from the response of the single unit cell.
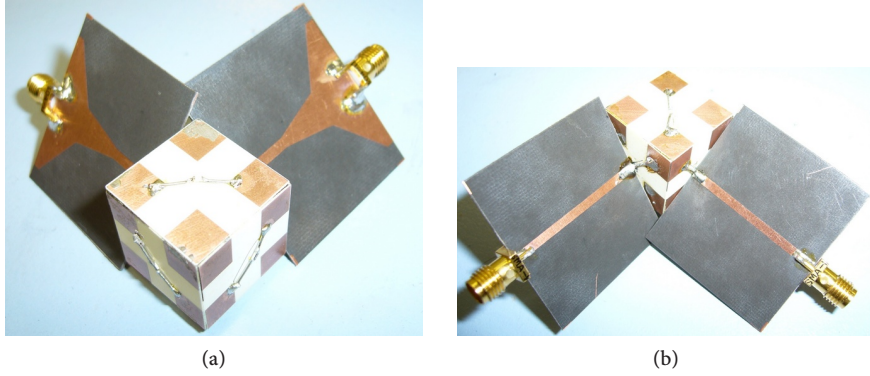
(a)

(b)

Figure 6.15: RTLM metamaterial unit cell with its input and output baluns required for the differential excitation of the measurement setup.

The extraction procedure of the lumped elements Z and Y is derived as follows: Taking the six-port impedance matrix (6.5) of the ideal RTLM cell and terminating the four unconnected ports with a load Z_L

$$V_i = -Z_L \cdot I_i \qquad i \in \{2,3,5,6\} \tag{6.15}$$

yields a symmetric two-port impedance matrix. This can be converted into a scattering matrix $\hat{\mathbf{S}}$ normalised to Z_L with the elements

$$\hat{s}_{11}^{(2\times2)} = \frac{4Z^2Y + 8Z - Z_L^2Y}{(2Z + Z_L)(2ZY + Z_LY + 4)} \tag{6.16a}$$

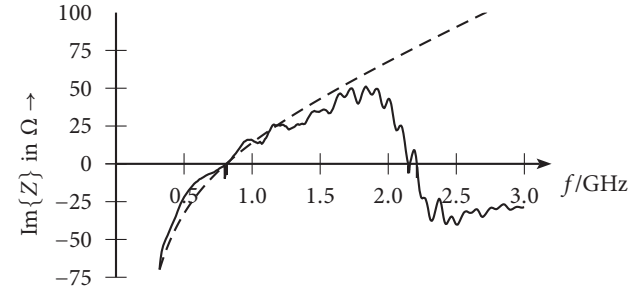$$\hat{s}_{21}^{(2\times2)} = \frac{-2Z_L}{(2Z + Z_L)(2ZY + Z_LY + 4)} \tag{6.16b}$$

Solving for Z and Y yields

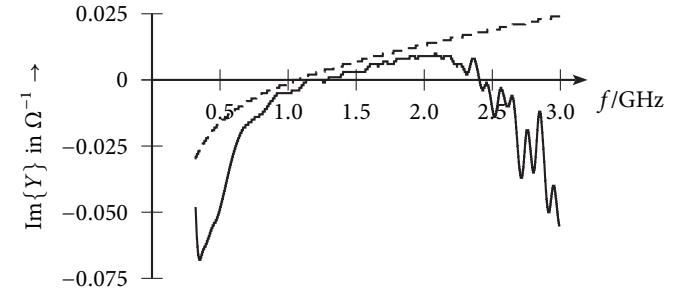$$Z = \frac{Z_L}{2} \cdot \frac{1 + \hat{s}_{11} + 2\hat{s}_{21}}{1 - \hat{s}_{11} - 2\hat{s}_{21}} \tag{6.17a}$$

$$Y = -\frac{(\hat{s}_{11} + 2\hat{s}_{12} - 1)(\hat{s}_{11} - 2\hat{s}_{21} - 1)}{2Z_L\hat{s}_{21}} \tag{6.17b}$$

$$1 + ZY = \frac{\hat{s}_{11}^2 - 4\hat{s}_{21}^2 - 1}{4\hat{s}_{21}} \tag{6.17c}$$

The scattering parameters $\hat{\mathbf{S}}$ are those obtained in the experiment.

(a)

(b)

Figure 6.16: Lumped element frequency dependency extracted from a measurement of the setup shown in Fig. 6.15. Solid line: measurements, dashed line: circuit simulator results using lumped elements only. (a) extraction of Z, (b) extraction of Y.

The dispersion relation for propagation along a principal axis is obtained by combining (6.17c) with (6.8), yielding

$$\sin^2 \tfrac{1}{2}\chi = (1 + ZY)^2 = \left(\frac{\hat{s}_{11}^2 - 4\hat{s}_{21}^2 - 1}{4\hat{s}_{21}} \right)^2 \tag{6.18}$$

The extracted frequency dependency of Z, Y is depicted in Fig. 6.16, showing fairly good agreement with lumped element simulations and thus verifying the assumption that the metamaterial cell acts like the intended lumped element circuit. A comparison of simulation and experimental data for the term $(1+ZY)$ is shown in Fig. 6.17 showing excellent agreement and further validating the lumped element assumption for frequencies up to 2.2 GHz. The reason for the better agreement of
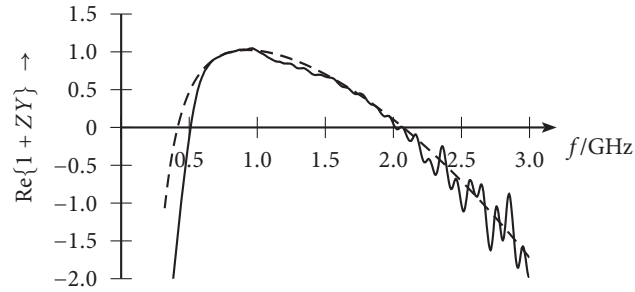
Figure 6.17: Comparison of measured (solid line) and simulated (dashed line) values for $(1 + ZY)$. This term is the frequency determining part of the dispersion relation of the RTLM metamaterial.
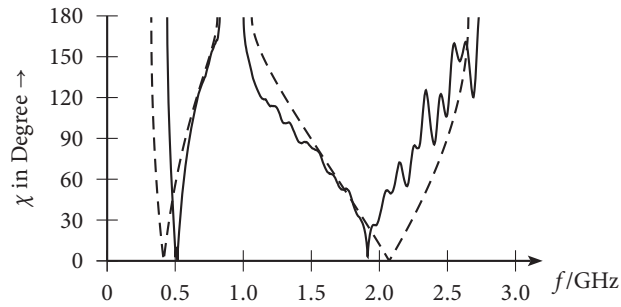

Figure 6.18: Dispersion diagram for propagation along a principal axis extracted from a measurement of the setup shown in Fig. 6.15. Solid line: measurements, dashed line: circuit simulator results using lumped elements only.

Fig. 6.17 compared to Fig. 6.16 is that (6.17c) is more robust compared to (6.17a) and (6.17b). As the term $(1 + ZY)$ is the frequency determining part of the RTLM metamaterial (see Eq. (6.7)), the dispersion diagram depicted in Fig. 6.18 shows also good agreement with circuit simulation results up to 2.2 GHz. The expected two left-handed and two right-handed frequency bands are clearly visible, therefore verifying the behaviour of the RTLM metamaterial.
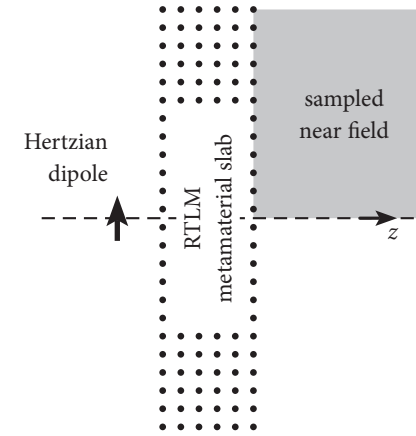

Figure 6.19: Full-wave simulation setup: $24 \times 24 \times 6$ cells illuminated by a Hertzian dipole, the near field is sampled in the imaging plane.

6.11 Full-Wave Simulation

A full-wave simulation of an arrangement of RTLM metamaterial cells needs to discretise both the narrow gap of the series parallel plate capacitors as well as the diagonally arranged wires implementing shunt inductors. This renders three-dimensional Method-of-Moments (MOM) simulation the preferable computational technique for full-wave simulations of such arrangements. A mesh convergence analysis of the 12-port scattering parameters of a single cell was performed, with the result that a coarse discretisation is applicable: Only one wire segment per wire and 48 surface triangles for the capacitor plates are needed, giving a total of 64 MOM unknowns per cell. This low discretisation requirement can be understood to be due to the operation of the unit cell in the quasi-static limit and the usage of parallel plate capacitors. The cell geometry was tuned for a refractive index of $n = -1$ at $f_0 = 2.178$ GHz, a periodicity of $a = 20$ mm and thus $a/\lambda \approx 1/7$, satisfying the metamaterial condition that the unit cell size needs to be small compared to the wavelength.

So far no 3D MOM simulator supporting periodic boundary conditions is commercially available, thus a finite setup of $24 \times 24 \times 6$ cells (giving a total size of $3.5 \times 3.5 \times 0.9$ wavelengths) was computed on a 48 node cluster with the commercial FEKO MOM code. The simulation setup is shown in Fig. 6.19: A Hertzian dipole
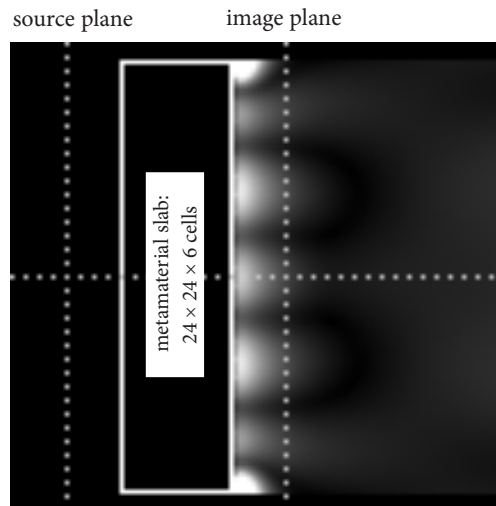
source plane   image plane

metamaterial slab:
24 × 24 × 6 cells

Figure 6.20: Simulation result to the setup of Fig. 6.19, showing the dominant transverse electric field magnitude in linear scale.
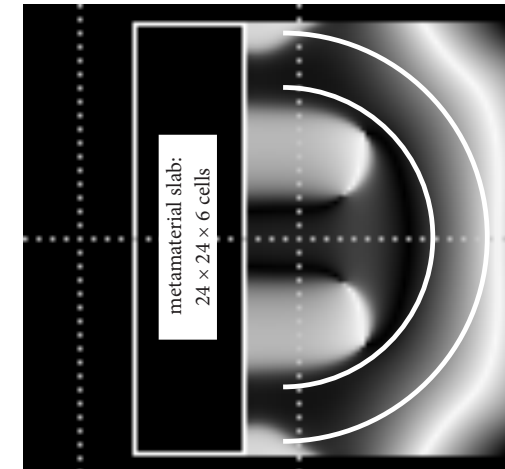

metamaterial slab:
24 × 24 × 6 cells

Figure 6.21: Simulation result to the setup of Fig. 6.19, showing the dominant transverse electric field phase.

excites the finite structure and the near-field is sampled in the imaging plane of the setup. The simulation has 56,000 MOM unknowns taking up 98.7 GB of memory and 13.4 hours runtime on the cluster.

Simulation results are displayed in Fig. 6.20, 6.21, 6.22, grey shades are in linear scale. The excitation and expected focus points reside where the dotted lines intersect. The magnitude of the dominant electric field is shown in Fig. 6.20, showing a surface wave propagating outwards, the voltage standing wave ratio being 2.3. Fig. 6.21 and 6.22 show the phase and instantaneous value of the dominant electric field, respectively, verifying that a spherical wave is originating from where the expected focus point resides. In Fig. 6.22 both the spherical wave front as well as the surface wave can be identified. This behaviour is yet better to see in the video animation of Fig. 6.23. Both the surface wave and the focussing indicate that the cells have a negative refractive index, as expected.
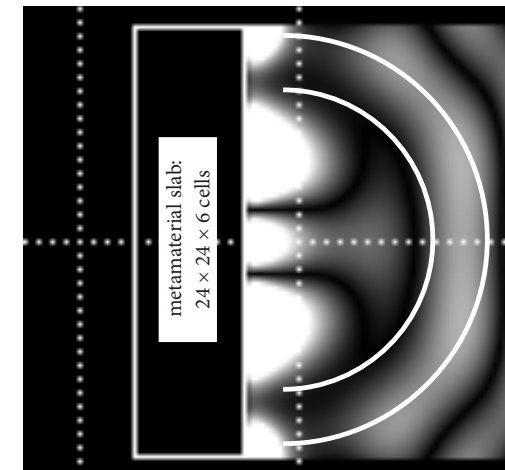

metamaterial slab:
24 × 24 × 6 cells

Figure 6.22: Simulation result to the setup of Fig. 6.19, showing the dominant transverse electric instantaneous field in linear scale.
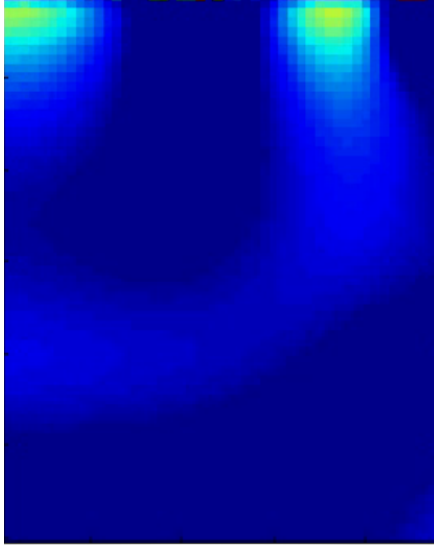
Figure 6.23: Video animation of the full-wave results of Fig. 6.22.

6.12 Efficient Computation of Large Arrangements

The previous section 6.11 showed that full-wave simulations of finite three-dimensional metamaterial structures requires an enormous computational power. In the future numerical codes will certainly become freely or commercially available that are able to efficiently solve arrangements incorporating RTLM metamaterial cells, e. g., based on the low-frequency multi-level fast multi-pole method LF-MLFMM, mode matching, or the domain decomposition/diacoptic approach. In this section a dispersion-model based approach is presented for inclusion into the numerical method SCN-TLM.

The approach can be derived as follows: The impedance matrix of the RTLM half unit cell was given in (6.5). The corresponding scattering matrix, normalised to the free space wave impedance $Z_0 = 376.7\,\Omega$, is

$$\tilde{\mathbf{S}}^{\langle 6 \times 6 \rangle} = \rho \cdot \mathbf{I} + \tau \cdot \mathbf{P} \tag{6.19}$$

with

$$\rho = \frac{8Z + 4Z^2 Y - Z_0^2 Y}{8Z + 4Z_0 + 4Z^2 Y + 4ZZ_0 Y + Z_0^2 Y} \tag{6.20a}$$

$$\tau = \frac{2Z_0}{8Z + 4Z_0 + 4Z^2 Y + 4ZZ_0 Y + Z_0^2 Y}, \tag{6.20b}$$

where ρ and τ are identified as reflection and transmission coefficients, respectively, from their association with the identity matrix $\mathbf{I}$ and the zero-diagonal matrix $\mathbf{P}$ defined in (6.6).

The scattering matrix of the conventional (not rotated) SCN 12-port network and the two scattering matrixes of the two RTLM 6-port half unit cell networks are related by (6.3a),

$$\mathbf{S}^{\langle 12 \times 12 \rangle} = \mathbf{Q}^T \cdot \begin{pmatrix} \tilde{\mathbf{S}}^{\langle 6 \times 6 \rangle} & \mathbf{0} \\ \mathbf{0} & \tilde{\mathbf{S}}^{\langle 6 \times 6 \rangle} \end{pmatrix} \cdot \mathbf{Q} = \rho \cdot \mathbf{I} + \tau \cdot \mathbf{S}_0 \tag{6.21}$$

with $\mathbf{Q}$ defined in (6.3b) and $\mathbf{S}_0$ being

$$\mathbf{S}_0 = \begin{pmatrix} \mathbf{0} & \mathbf{S}_A & \mathbf{S}_A^T \\ \mathbf{S}_A^T & \mathbf{0} & \mathbf{S}_A \\ \mathbf{S}_A & \mathbf{S}_A^T & \mathbf{0} \end{pmatrix} \qquad \mathbf{S}_A = \begin{pmatrix} +1 & +1 & 0 & 0 \\ -1 & -1 & 0 & 0 \\ 0 & 0 & +1 & -1 \\ 0 & 0 & +1 & -1 \end{pmatrix} \tag{6.22}$$

This expression for the conventional scattering matrix is slightly different from the original Johns' matrix [Johns, 1987] in (6.1a), (6.2a): In the latter case ρ equals zero, while here reflection occurs and $\mathbf{S}_0$ has a different structure. This is due to the simplification convenient for the construction of RTLM metamaterials explained in Sect. 6.2.

6.12.1 Bilinear Time-Discretisation

The RTLM scheme of the previous section (already discretised in space) will now be discretised in the time domain also. For this purpose, we first substitute the Laplace complex frequency variable $s = \sigma + j\omega$ into the functions $Z(\omega)$ and $Y(\omega)$ appearing in (6.20), which leads to expressions $\rho(s)$ and $\tau(s)$. Next, we introduce the bilinear transform substitution [Oppenheim and Schäfer, 1999]

$$s \rightarrow K \frac{z-1}{z+1} \tag{6.23}$$

where the parameter K may be set for exact match between the analog and digital responses at the frequency ω_1 as

$$K = \frac{\omega_1}{\tan(\omega_1 \Delta T/2)} = \frac{2}{\Delta T}\left(1 - \Delta T^2 \omega_1^2/12\right) + \mathcal{O}(\omega_1 T)^4 \qquad (6.24)$$

where $1/\Delta T$ is the digital sampling rate. For typical metamaterial space discretisations, $\omega_1 \Delta T/2 \ll 1$, and therefore the zeroth order approximation in this relation can safely be used over the entire frequency range of interest.

In the specific case of double Drude elements as given in (3.8) we have

$$Z(s) = sL_R + \frac{1}{sC_L}, \quad Y(s) = sC_R + \frac{1}{sL_L}. \qquad (6.25)$$

The corresponding scattering matrix $\mathbf{S}^{\langle 12 \times 12 \rangle}$ is then obtained as follows:

- substitute (6.23) into (6.25) with (6.24)

- substitute the resulting expressions $Z(z)$ and $Y(z)$ into (6.20)

- insert the resulting expressions $\rho(z)$ and $\tau(z)$ into (6.21), which yields $\mathbf{S}^{\langle 12 \times 12 \rangle}(z)$

6.12.2 IIR Digital Formulation

In digital signal processing terms, the bilinear transform (6.23) has converted the continuous-time transfer function $\mathbf{S}^{\langle 12 \times 12 \rangle}_{\text{analog}}(s)$ of (6.21) into a discrete-time transfer function $\mathbf{S}^{\langle 12 \times 12 \rangle}_{\text{digital}}(z)$, mapping positions on the $j\omega$ axis in the Laplace plane into the unit circle in the z-plane. Each coefficient of the matrix $\mathbf{S}^{\langle 12 \times 12 \rangle}_{\text{digital}}(z)$ may then be efficiently computed as an infinite impulse response (IIR) filter transfer function [Oppenheim and Schäfer, 1999]

$$s_{\text{digital},ij}(z) = \frac{\sum_{n=1}^{N} b_i z^{-i}}{\sum_{n=1}^{N} a_i z^{-i}}, \qquad (6.26)$$

by using the classical difference equation

$$y(n) = a_1^{-1}[b_1 x(n) + b_2 x(n-1) + \cdots + \\ + \cdots + b_N x(n-N+1) - a_2 y(n-1) - \cdots - a_N y(n-N+1)], \quad (6.27)$$

where n is the discrete-time index, x and y are the input and output signals, respectively, and a and b are the feedback and feed-forward filter coefficients, respectively, which only depend on the constants L_L, L_R, C_L, C_R, and K. Due to the derivation from an analog filter these digital IIR filters are unconditionally stable, i. e., all of their poles lie within the unit circle of the z-plane.

More specifically, by noting the scattering relation corresponding to the scattering matrix (6.21) as

$$[V(n)] = \rho \star \mathbf{I}\left[V(n-1)\right] + \tau \star \mathbf{S}_0 \cdot \left[V(n-1)\right] \\ = \left[V_\rho(n-1)\right] + \mathbf{S}_0\left[V_\tau(n-1)\right] \qquad (6.28)$$

with the star $\star$ denoting convolution. We find out that each scattering function term (corresponding to every unit cell face-to-face transfer function) may be represented by two separate IIR filter outputs, $\left[V_\rho(n-1)\right]$ for reflection and $\left[V_\tau(n-1)\right]$ for transmission. Each component $V_{\rho,i}$ and $V_{\tau,i}$ denotes the output of the reflection and transmission IIR filters at port i, respectively, while V_i denotes the scattered wave at port i of the SCN-TLM node shown in Fig. 6.1(c).

The scattering scheme of (6.28) can then be incorporated into a conventional time-domain TLM simulator [Hoefer and So, 2003] on a per-cell basis, enabling simulation setups with both conventional cells and 3D RTLM cells.

6.12.3 Computational Efficiency

The IIR update equation (6.27) for (6.28) may be computed efficiently by the algorithm [Oppenheim and Schäfer, 1999]

$$y(n) = b_1/a_1 x(n) + z_1(n-1) \qquad (6.29a)$$
$$z_1(n) = b_2/a_1 x(n) + z_2(n-1) - a_2/a_1 y(n) \qquad (6.29b)$$
$$\vdots$$
$$z_5(n) = b_6/a_1 x(n) + z_6(n-1) - a_6/a_1 y(n) \qquad (6.29c)$$
$$z_6(n) = b_7/a_1 x(n) \qquad\quad - a_7/a_1 y(n) \qquad (6.29d)$$

Then, each filter consumes in an update cycle 13 multiply-accumulate (MAC) instructions and 6 additions which for the given algorithm can be calculated by 8 single instruction multiple data (SIMD) instructions on a modern PC. These additional calculations need to be performed for each of the 24 filters compared to the standard SCN TLM scheme.

Assuming that the IIR filters are implemented as canonical *direct form 2 transposed* type filters [Oppenheim and Schäfer, 1999], which consume a minimum amount of memory, the permanent memory storage requirement per metamaterial cell is

$$\text{sizeof(variable)} \quad \times \quad \underbrace{12}_{\text{\# of ports}} \quad \times \quad \underbrace{2}_{\text{\# of IIR filters}} \quad \times \quad \underbrace{6}_{\substack{\text{\# of storage elements} \\ \text{per IIR filter, see Eq. (6.29a)}}} \qquad (6.30)$$

which represents 1152 bytes per metamaterial cell using double-precision arithmetic. Double precision is required due to close proximity of the poles of the transfer functions to the unit circle in the *z*-domain. Compared to 48 bytes for a non-metamaterial cell using single-precision arithmetic, this results in a memory storage increase by a factor of 24. The IIR feedback and feed-forward coefficients corresponding to this algorithm are given in Appendix B.

6.13 Summary

Within this chapter an isotropic three-dimensional metamaterial structure that supports two polarisations was presented. First the SCN-TLM scheme and its variant, the RTLM method were derived using solely symmetry considerations of a general space-discretising cell. In the TLM computational scheme propagation of waves is described according to Huygen's priciple by a continuous scattering of waves. The polarisation of incident and scattered waves are taken as horizontal and vertical within the SCN-TLM scheme, leading to a scattering matrix representation of a fully-coupled 12-port. In the RTLM method instead of horizontal and vertical polarisations one considers diagonal polarisations, leading to a scattering matrix representation of two uncoupled six-ports. These six-ports form the basis of an elementary metamaterial cell. A physical realisation of this metamaterial cell was proposed which fulfills the symmetry group of the simple cubic lattice. Wave propagation through the structure was studied using algebraic analysis, circuit simulation, full-wave simulation and measurements. For the efficient simulation of non-periodic setups containing RTLM metamaterial cells a dispersion-model was derived that can be incorporated into the computational method SCN-TLM.

7 Fabrication of 3D Metamaterials

Three-dimensional metamaterials are challenging to fabricate, on one hand the unit cells are more complex compared to the one- and two-dimensional case, on the other hand the number of cells required for for a setup increases: Assuming ten metamaterial cells per wavelength and a structure size of five wavelength, this yields $50^3 = 125,000$ cells. In order to overcome these problems we present two approaches: decomposition of the unit cell into polyhedra, and topology-invariant planarisation.

7.1 Decomposition into Polyhedra

Three-dimensional metamaterials proposed so far in literature all use cubic cells to discretise space [Mercure et al., 2005, Koschny et al., 2005, Vendik and Gashinova, 2004, Alitalo et al., 2006a, Zedler and Russer, 2006, Zedler et al., 2008a, Grbic and Eleftheriades, 2005a]. These unit cells can be decomposed into polyhedra [Hofmann et al., 2008, Zedler and Russer, 2008] so that all metal parts lie on polyhedron surfaces. These structures can be fabricated with technologies like (2 component)-injection moulding [Murphy, 2002], 3D molded interconnect device technology (3D-MID) [Eberhardt et al., 2006], hot embossing [Pein et al., 2004], plasma activation and printing [Möbius et al., 2008], physical vapour deposition [Forschungsvgg. Räumliche Elektronische Baugruppen 3-D MID e.V., 2004], and laser direct structuring [LPKF Laser & Electronics AG, 2008]. For prototyping 3D printers can be used. As will be shown subsequently, the polyhedra are primarily mechanical supporting structure. Electric field penetration into the polyhedra is low, making the metamaterial behaviour insensitive to substrate losses within the polyhedra. The above mentioned fabricational approaches limit the achievable unit cell size to the order of millimetres, but one may also envision polyhedron decomposition for micro/nanostructuring as well.

In the following we present decomposition into polyhedra for the RTLM structure [Zedler and Russer, 2006], the Kron structure [Grbic and Eleftheriades, 2005a] and the scalar 3D structure in series configuration (see Sect. 5).
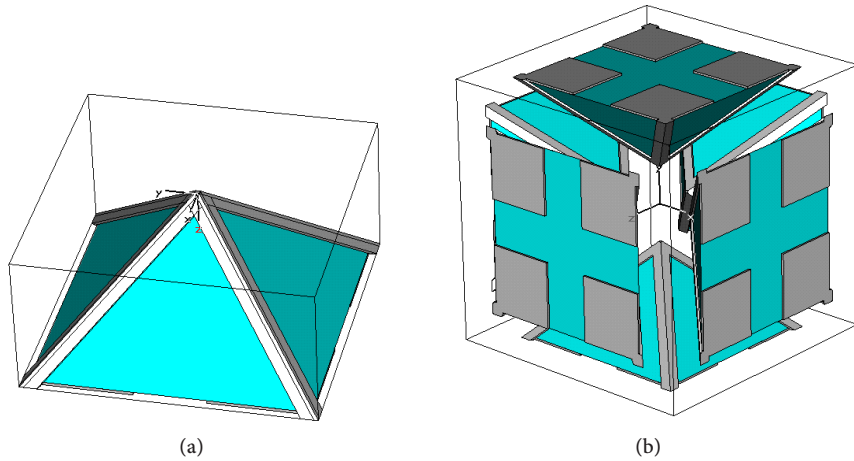
Figure 7.1: Decomposition of a RTLM unit cell into pyramids. Turquoise denotes dielectric, grey metallisation. Spacing between cells is achieved through, e. g., thin dielectric sheets and a mechanical press fit. (a) single pyramid element, (b) six pyramid elements forming a unit cell.

7.1.1 *RTLM Metamaterial Unit Cell*

The unit cell depicted in Fig. 6.10 can be decomposed into pyramids (see Fig. 7.1) and compounds of pyramids (see Fig. 7.2–7.5). Each of these offer specific advantages and disadvantages,

- a single pyramid offers the simplest casting mould, see Fig. 7.1.

- two compound pyramids offer a simple casting mould. Metallisation can be performed using planar metallisation techniques, see Fig. 7.2.

- three compound pyramids forming a half-cell, offering a self aligning structure when two half-cells are set into each other, see Fig. 7.3.

- merging half-cells to form a half-cell line (see Fig. 7.4), with inter-cell capacitive coupling realised using capacitive coupling patches. The latter approach is described in detail in Sect. 7.2.

- merging half-cell lines to half-cell planes, as shown in Fig. 7.5. In this figure the additional dielectric elements compared to Fig. 7.4 are shown in red for
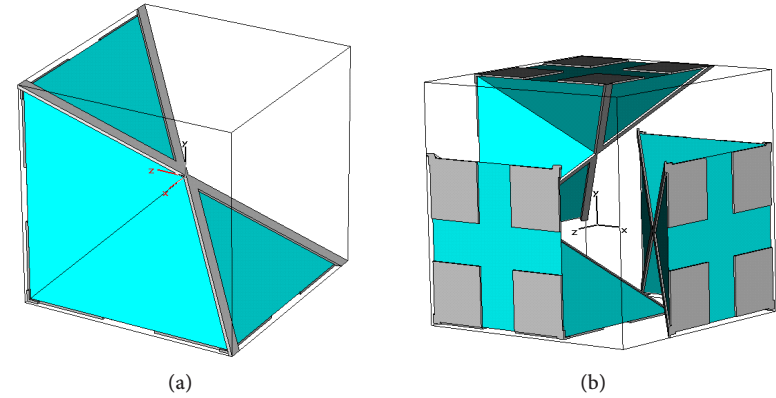

Figure 7.2: Compound polyhedron consisting of two pyramids. (a) single compound polyhedron. Metallisation can be applied using solely planar technology, (b) Three polyhedra forming a unit cell.

clarity. These extra elements only serve mechanical connection purposes.

- inductive connections may be lay out as a meander in order to decrease the magnetic plasmon frequency, see Fig. 7.6.
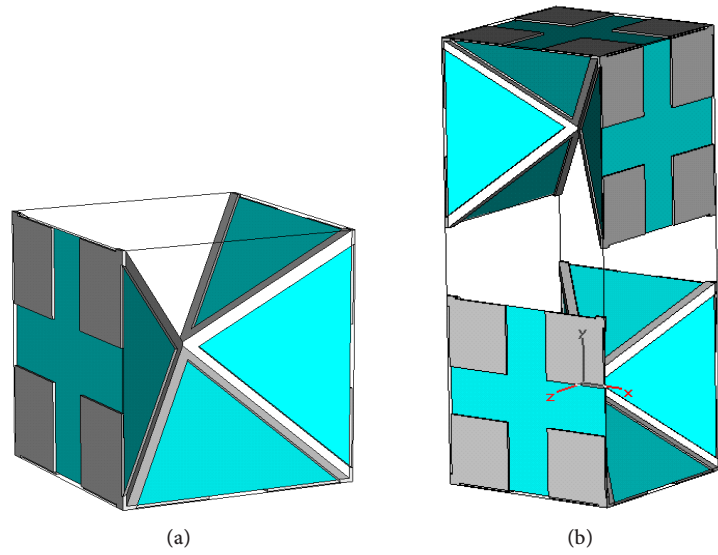
Figure 7.3: (a) Compound polyhedron consisting of three pyramids, (b) Two poly-hedra yield a mechanically self-aligning structure forming the unit cell.
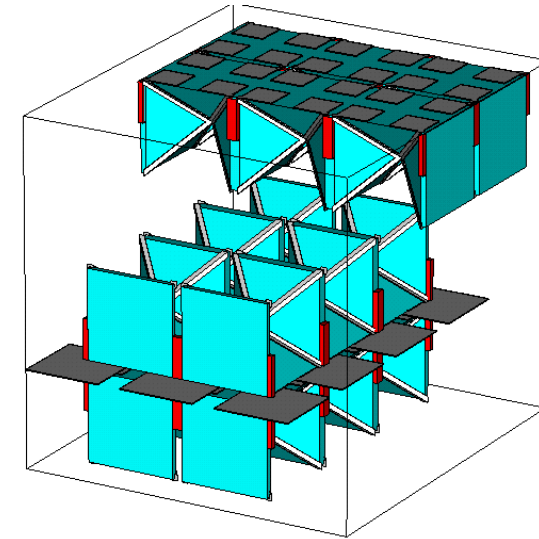

Figure 7.5: Half-cell lines mechanically connected by dielectric (shown in red for clarity) forming a half-cell plane.
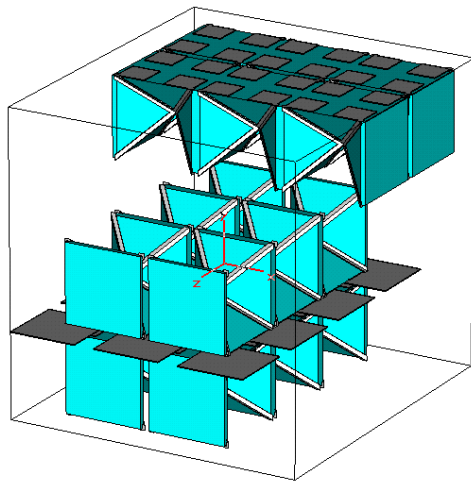

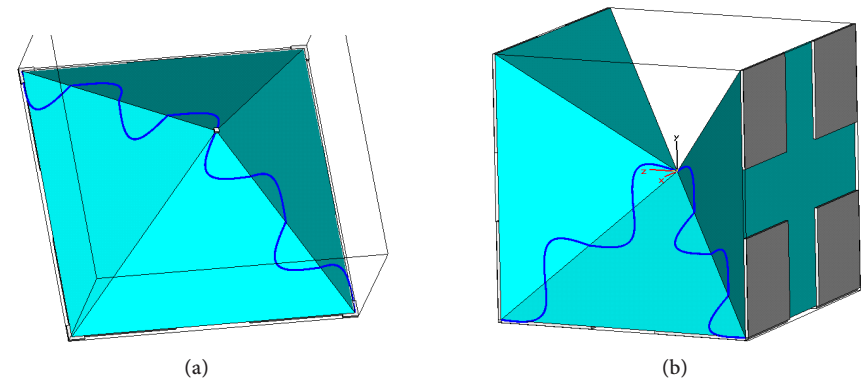Figure 7.4: Merged half-cells as of Fig. 7.3 yielding a half-cell line.

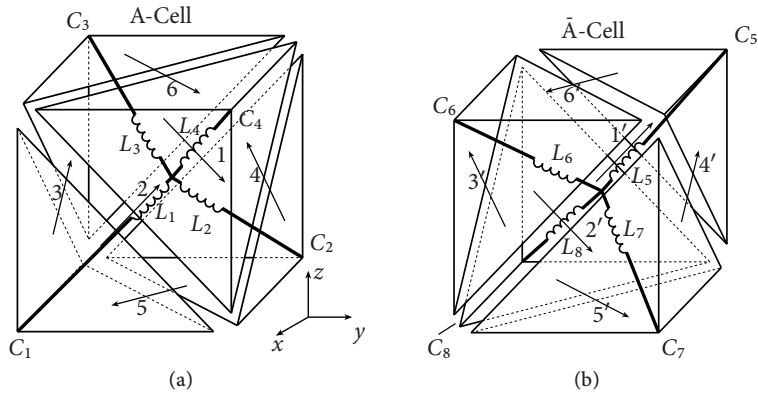Figure 7.6: Variations of inductive connections.

Figure 7.7: Separated half-cells configuration: schematic view.

7.1.2 RTLM *Metamaterial in Half-Cell Configuration*

In Fig. 7.8 a structure implementing the alternating, i. e., non-nested configuration of the RTLM metamaterial cell is shown. Ports run along diagonals and are denoted by 1..6 and $1'..6'$. Wires L_i implement a shunt inductance while metallic plates, together with the plates of the adjacent cell, series capacitors, denoted by C_i. As explained in Sect. 6, a $2 \times 2 \times 2$ cluster of such half-cells implements a complete metamaterial cell. This structure has the advantage of reduced parasitic capacitive coupling between two half-cells and that imperfections in fabrication cannot lead to galvanic coupling at the centre point. The main disadvantage of this structure is that it is more difficult to achieve a unit cell size that is small compared to the wavelength, as a unit cell consists of $2 \times 2 \times 2$ half-cells.

In Fig. 7.8(a) the polyhedron decomposition of a half-cell is shown. This polyhedron corresponds to the Fig. 7.7(b), specifically the rear bottom right part. The polyhedron is a hexahedrons fulfilling the condition that the complete metallisation is on the surface of the hexahedron. With four hexahedrons making up a half-cell and a complete unit cell consisting of 8 half-cells, a complete unit cell needs 32 hexahedrons. An arrangement of unit cells in half-cell configuration is shown in Fig. 7.8(b).
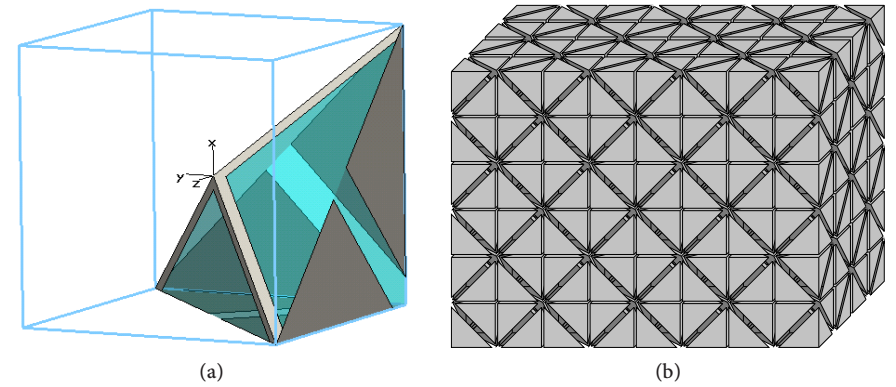

Figure 7.8: (a) Hexahedron decomposition of a half-cell. The shown hexahedrons corresponds to the rear bottom right part of Fig. 7.7(b). (b) Arrangement of unit cells made up of half-cells.
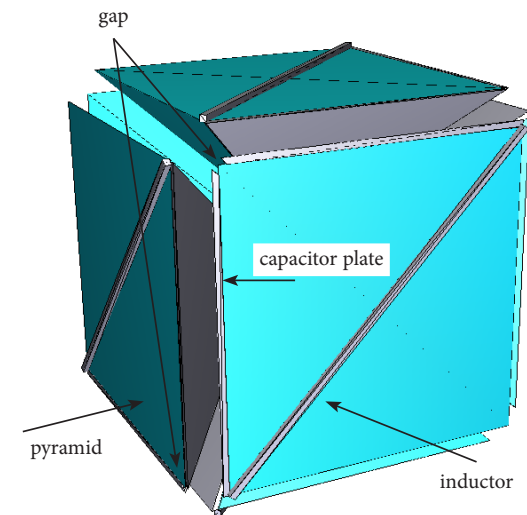

Figure 7.9: Decomposition of the scalar 3D metamaterial cell in series configuration into pyramids.

7.1.3 Scalar 3D Metamaterial Cell in Series Configuration

In Chapter 5 the scalar three-dimensional metamaterial in series configuration was presented. This geometry can be decomposed into pyramids as shown in Fig. 7.9. In contrast to the RTLM structure, six pyramids forming a unit cell need to be assembled with a thin spacer to avoid a short-circuit of the capacitive coupling.

7.1.4 Kron's Unit Cell

Another vectorial metamaterial was proposed in [Grbic and Eleftheriades, 2005a], which is based on Kron's equivalent circuit representation of free space [Kron, 1943]. The inverted configuration yielding left-handed behaviour is shown in Fig. 7.10(a), its physical realisation in Fig. 7.10(b). Wires along the edges of the unit cell implement inductors, which are interconnected by diagonal plate capacitors. While this unit cell is seemingly highly complicated, in fact a shift of the unit cell boundaries by half a cell along all directions yields the simpler appearing structure shown in Fig. 7.10(c). This structure can be decomposed into polyhedra as shown in Fig. 7.10(d), which is a symmetrically cut octahedron. The top and bottom half pyramid faces are metallised but separated by a gap. On the cut face rests an inductive strip, connecting the tips of the half pyramids. Another approach is a surface-metallised octahedron with a drilled metallised hole connecting the tips.

7.2 Topology-Invariant Planarisation

While full three-dimensional fabrication as proposed in Sect. 7.1 offers the highest level of isotropy and design flexibility, planar fabrication techniques are much more common in microwave and photonics engineering. In [Zedler et al., 2007b] topology-invariant planarised geometries of the RTLM metamaterial were proposed, and analysed numerically as well as algebraically, yielding design guidelines for this geometry. These will be presented here and extended to also cover the novel scalar three-dimensional structure described in Sect. 5.

7.2.1 RTLM Metamaterial Unit Cell

Fig. 7.11 shows the cross-sectional view of the planarised RTLM metamaterial cell. Fig. 7.12(a) shows the corresponding metal layers. The layers m_1 and m_5 at the bottom and top correspond to the patches in the cell corners in Fig. 6.10. Layer m_5 is identical with layer m_1 of the overlying cell. Each of the four patches of the
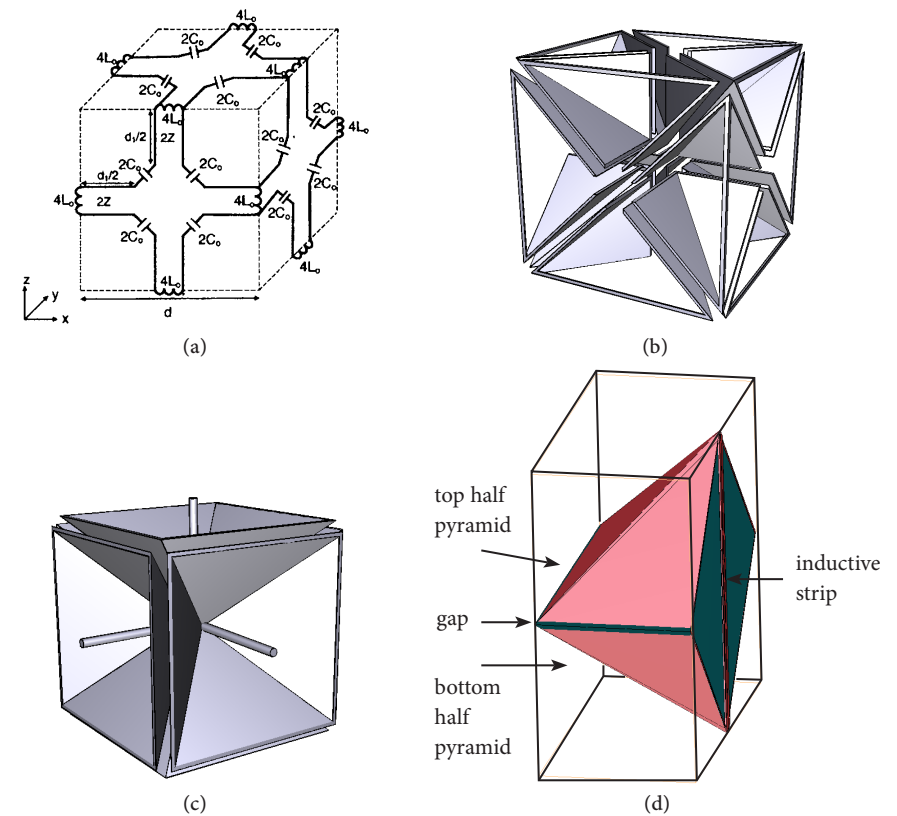
Figure 7.10: Decomposition of Kron's cell into polyhedra. (a) Kron's cell based metamaterial, taken from [Grbic and Eleftheriades, 2005a] with permission, (b) physical implementation of Kron's cell. Inductors along the edges implemented by wires, capacitive coupling between inductors by diagonally oriented plate capacitors, (c) identical structure to Fig. 7.10(b), but unit cell boundaries shifted along all directions by half a cell, (d) decomposition of Kron's unit cell elementary polyhedron consisting of two half pyramids. Red parts denote metallised parts, green side signifies not metallised surface. The inductive strip resembles the wire in Fig. 7.10(c).

Figure 7.11: Cross-sectional view of the planarised RTLM metamaterial cell. ϵ_1: low permittivity; ϵ_2: high permittiv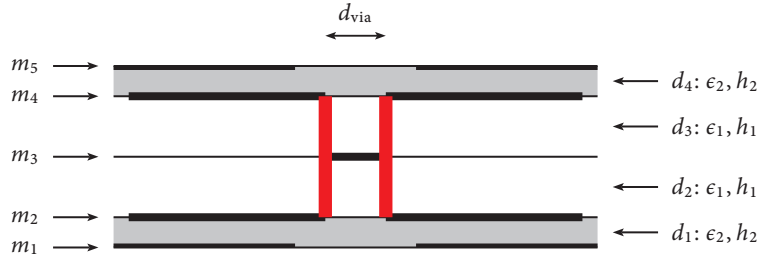ity; h_2 as thin as possible. Vertical thick lines: buried via. Via distance d_{via} as small as possible. m_i denote the metallisation layers in the unit cell. If multiple cells are stacked then the adjacent top and bottom layers m_1 and m_5 can be merged into one layer.

layers m_1 and m_5, is continued into the four neighbouring cells at every corner. These patches ensure the capacitive coupling with the neighbouring cells via the patches of layers m_1 and m_4. In the layers m_2 and m_4 the strips are connected to the patches with insets, which increase the inductance. Together with the through-connections through layers d_2 and d_3 these strips form the required inductive coupling. The vertical capacitive coupling is achieved through two series capacitances $m_4 \rightarrow m_5 \rightarrow m_2'$ (where the prime denotes the next unit cell). In-plane capacitive coupling is achieved through two series capacitances $m_4 \rightarrow m_5 \rightarrow m_4'$.

An alternative configuration requiring no metal-insulator-metal patches is depicted in Fig. 7.12(b): Here the vertical capacitive coupling is $m_4 \rightarrow m_2'$. The in-plane capacitive coupling is achieved by inter-digital capacitors (IDC) $m_4 \rightarrow m_4'$. In addition to the advantage of requiring less layers per unit cell, this configuration also alleviates fabrication tolerances with respect to dielectric layer thicknesses, as the two layers d_1/d_4 are merged into one layer. This advantage comes at a cost; both C_L and L_R of the vertical plate capacitors and the in-plane inter-digital capacitors need to be carefully matched.

7.2.1.1 Parasitic Coupling due to Planarisation

While ideally the network topology of Fig. 7.11–7.15 should equal that of Fig. 6.3 and 6.5(a), unwanted capacitive coupling $m_2 \rightarrow m_4$ needs to be considered. Such parasitic effects couple the otherwise independent two half cells, as shown in Fig. 7.16.
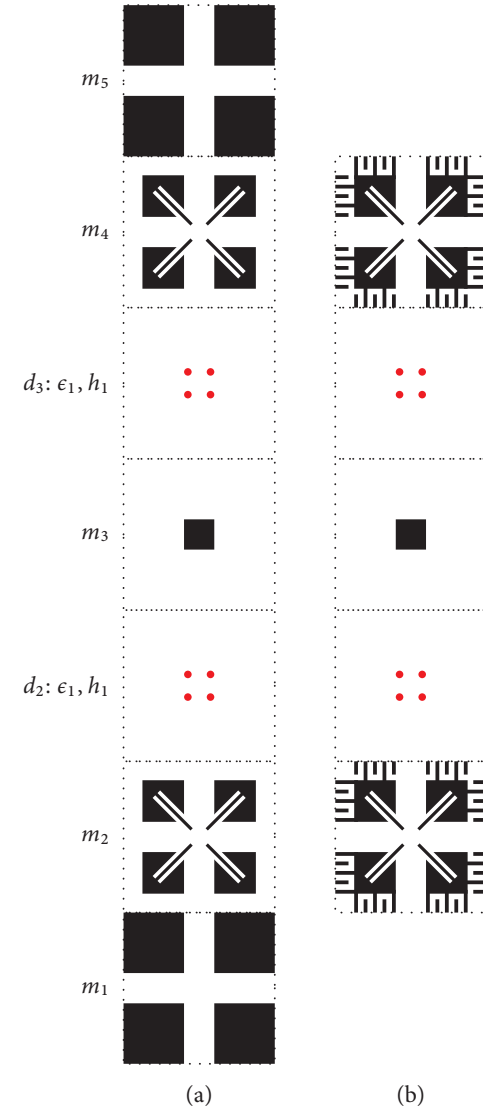

Figure 7.12: Exploded top view on the different metal layers for the structure of Fig. 7.11. (a) parallel plate capacitor implementation, (b) inter-digital capacitor implementation.
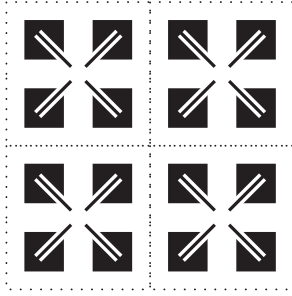
Figure 7.13: Top view of layer m_2/m_4 of 2×2 cells of the structure depicted in Fig. 7.12(a).
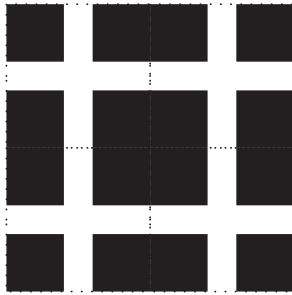
Figure 7.14: Top view of layer m_1/m_5 of 2×2 cells of the structure depicted in Fig. 7.12(a). The coupling patches provide the series capacitive coupling between in-plane adjacent cells.
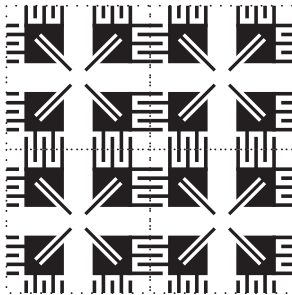
Figure 7.15: Top view of layer m_2/m_4 of 2×2 cells of the structure depicted in Fig. 7.12(b).
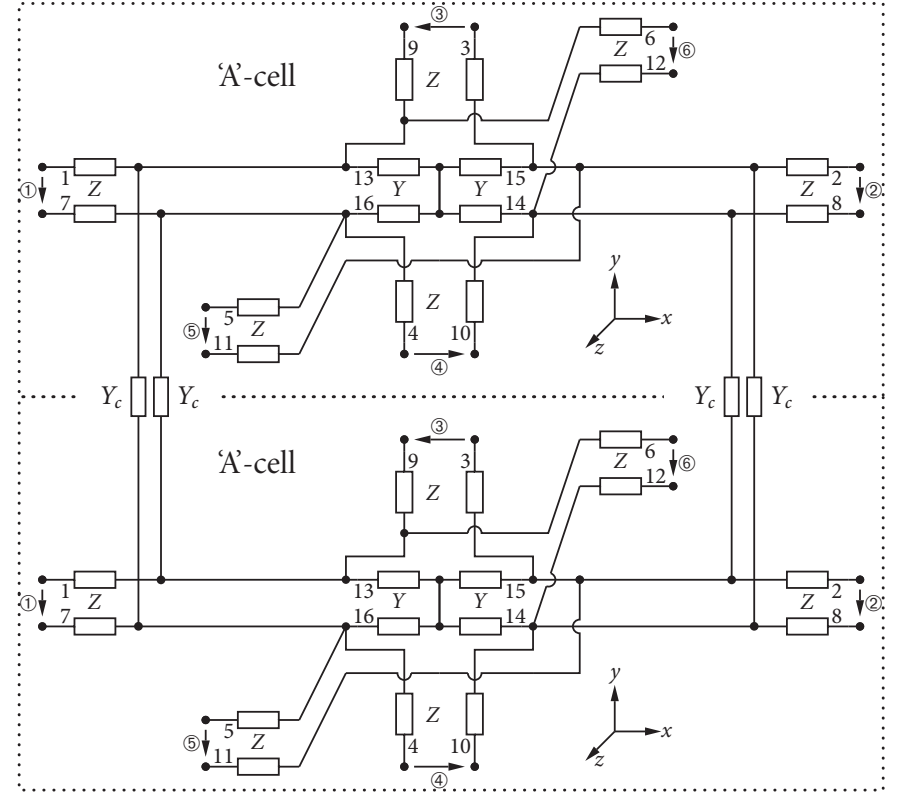
Figure 7.16: Planarised unit cell consisting of two nested 'A' cells with parasitic coupling modelled by Y_c.

In order to obtain the dispersion relation we first calculate the impedance matrix of the 12-port by setting up Kirchhoff's equations. One obtains

$$\mathbf{Z} = \begin{pmatrix} \mathbf{Z}_A & \mathbf{Z}_B \\ \mathbf{Z}_B & \mathbf{Z}_A \end{pmatrix} \tag{7.1}$$

with

$$(Y + 2Y_c) \cdot \mathbf{Z}_A = 2\left(1 + Z(Y + 2Y_c) + Y_c/Y\right) \cdot \mathbf{I} - 2\left(1 + \frac{Y_c}{Y}\right) \cdot \mathbf{P} \tag{7.2}$$

$$(Y + 2Y_c) \cdot \mathbf{Z}_B = 2\frac{Y_c}{Y}(\mathbf{P} - \mathbf{I}) \tag{7.3}$$
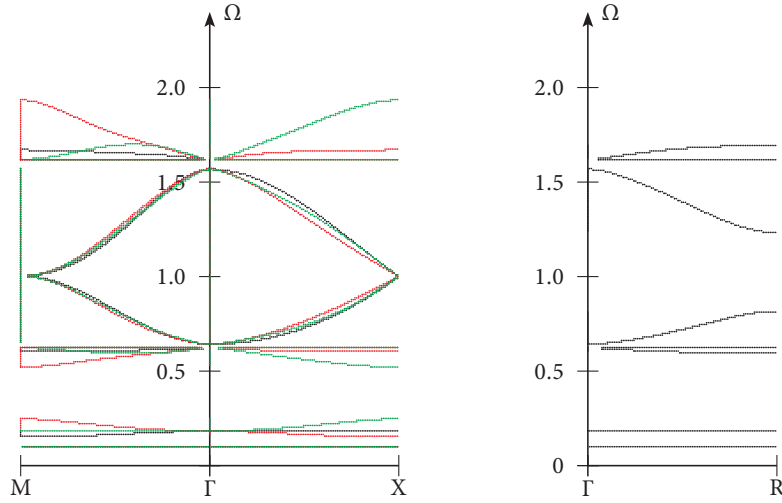
Figure 7.17: Dispersion diagram to (7.4) for a resonance-balanced unit cell with $L_L/L_R = 1$ and $Y_c Z = \frac{1}{5}$. For $\Gamma \to$ X, black represents propagation along χ, red represents propagation along η, green represents propagation along ξ. For $\Gamma \to$ M, black represents propagation along $\chi = \eta$, red represents propagation along $\chi = \xi$, green represents propagation along $\eta = \xi$.

using the matrix $\mathbf{P}$ defined in (6.6).

The dispersion relation is calculated from the impedance matrix (7.1) using the algebraic approach presented in Appendix A.5.3. One obtains

$$\frac{1}{4}(3 - \cos\chi\cos\eta - \cos\chi\cos\xi - \cos\eta\cos\xi) - (1 + ZY)^2 =$$
$$- \frac{Y_c Z}{1 + ZY} \left[\cos\eta\cos\xi + (1 + Z(Y + 2Y_c))(\cos\eta - \cos\xi)\right]$$
$$- \frac{Y_c Z}{1 + ZY} \left[4Y^2 Z^2 + 8ZY + 3 + 4Y_c Z(1 + ZY)\right] \quad (7.4)$$

In the limiting case $Y_c \to 0$ the dispersion relation of the planarised RTLM metamaterial reduces to that of (6.7) because then the right hand side of (7.4) vanishes.

The dispersion diagram corresponding to (7.4) for a resonance-balanced unit with $L_L/L_R = \Omega_0 = 1$ and $ZY_c = \frac{1}{5}$ is plotted in Fig. 7.17. The isotropic behaviour around the Γ-point is approximately maintained. As both Y_c and Z are realised by

plate capacitors (Fig. 7.11), a reasonable corresponding design guideline is

$$h_1 \geq 5 \frac{\epsilon_1}{\epsilon_2} h_2 \qquad (7.5)$$

with respect to Fig. 7.11. In order to satisfy (7.5) several interdependent conditions need to be met:

1. The unit cell size needs to be small compared to the wavelength.

2. The via distance d_{via} plus via diameter need to be small compared to the unit cell size.

3. The via diameter is related to h_1 through the achievable aspect ratio, but (7.5) needs to be fulfilled.

4. The thickness of the thin dielectric layers d_1 and d_4 needs to have very small tolerances in order to assure good control over C_L.

While item 4 can be overcome by using inter-digital capacitors as shown in Fig. 7.12(b) instead of coupling plates, the design of such a double Drude resonance-balanced unit cell is more challenging: Both C_L and L_R of the vertical plate capacitors and the in-plane inter-digital capacitors need to be matched.

7.2.1.2 NUMERICAL CALCULATION OF THE DISPERSION RELATION

Numerical results of the planarised 3D RTLM structure were calculated for a sample with coupling patches in m_1/m_5 using CST MWS and Ansoft HFSS. The unit cell edge length a is 20 mm, and the dielectrics are $h_1 = 5$ mm, $h_2 = 1$ mm, $\epsilon_1 = 1$, and $\epsilon_2 = 10$. The structure's dimensions are summarised in Tab. 7.1. The dispersion diagram for $\Gamma \to$ X along the z-axis is shown in Fig. 7.18, displaying good agreement between CST MWS and Ansoft HFSS. The lower right-handed mode is a perturbed plane-wave mode not described by the network model. It corresponds to artificial dielectrics as described in [Collin, 1990]. The left-handed mode, corresponding to the lower left-handed mode of Fig. 6.8, is clearly visible. The electric field distribution of the left-handed mode for $\chi = \eta = 0$, $\xi = \frac{1}{6}\pi$ is shown in Fig. 7.19. The high confinement of the electric field in the plate capacitors proves the assumption of lumped element behaviour and accordingly the homogeneity requirement of metamaterials as well as the low impact of the parasitic capacitance Y_c for the simulated configuration.

Table 7.1: Geometry parameters for the simulation of the planarised RTLM metamaterial cell.

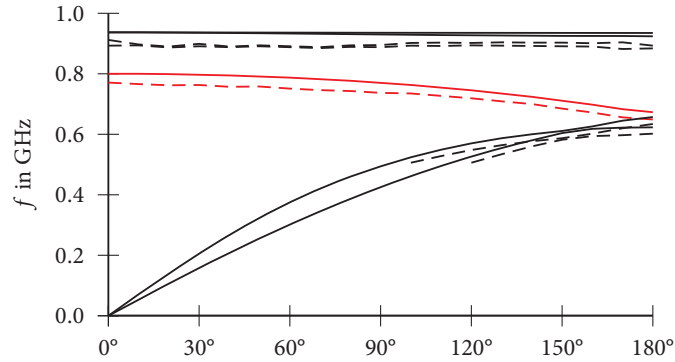| parameter	value in units of $a/64$
via distance	$4\sqrt{2}$
via diameter	1
m_2/m_4 strip inset width	6
m_2/m_4 strip width	1
m_2/m_4 strip length	28
m_2/m_4 patch to cell boundary distance	4
m_2/m_4 patch edge length	20
m_1/m_5 patch edge length	24

Figure 7.18: Numerical calculation of the dispersion diagram of the planarised unit cell for $\Gamma \rightarrow$ X along the z-axis. Solid lines: CST MWS Jacobi-Davidson Eigenmode solver, dashed lines: HFSS eigenmode solver. Left-handed band emphasised by red lines. Sampled every 10°.
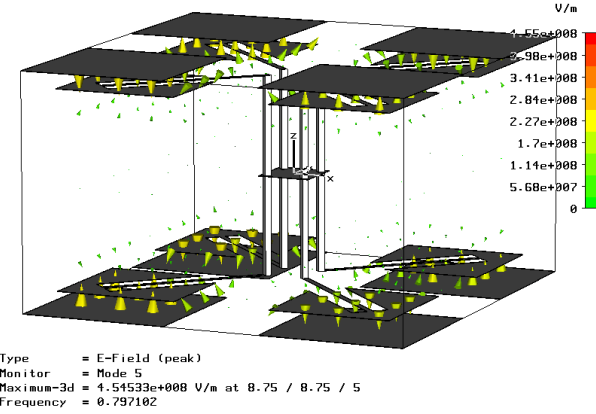

Figure 7.19: Electric Field distribution for $\chi = \eta = 0$, $\xi = \frac{1}{6}\pi$ for the left-handed mode (see Fig. 7.18).

7.2.2 Scalar 3D Metamaterial Cell in Series Configuration

The network topology of the scalar 3D metamaterial in series configuration has been shown in Fig. 5.3. A planarised physical realisation of this topology yielding Drude dispersion for the permeability and permittivity is depicted in Fig. 7.20: Layer m_1 provides the in-plane elements of the 2D scalar series configuration (see also Fig. 4.1b). Black parts denote metallisation, hatches represent inter digital capacitors, and red circles are connection points of vias. The stubs connecting to the edge of the unit cell form half of the shunt inductance, inter-digital capacitors the series capacitance. Two vias located in the bottom left connect to layer m_2, the two vias in the top-right connect to the above's cell layer m_4. In layer m_2 vias connect to metal plates. Together with plates in layer m_3, these form two series plate capacitors. In layer m_3 inductive coupling is implemented by a thin strip, shown in red for clarity. Metallic plates in layer m_4 form a series capacitance with those in layer m_3 towards the cell below. There two vias connect to the next cell's layer m_1 in the top right.

The shape of the metallic layers m_2, m_3, and m_4 can be varied in order to tune the shunt inductance of layer m_3 and the vertical series capacitance. Thus together with the choice of layer dielectrics and layer thicknesses anisotropy of the planarised structure can be well controlled.
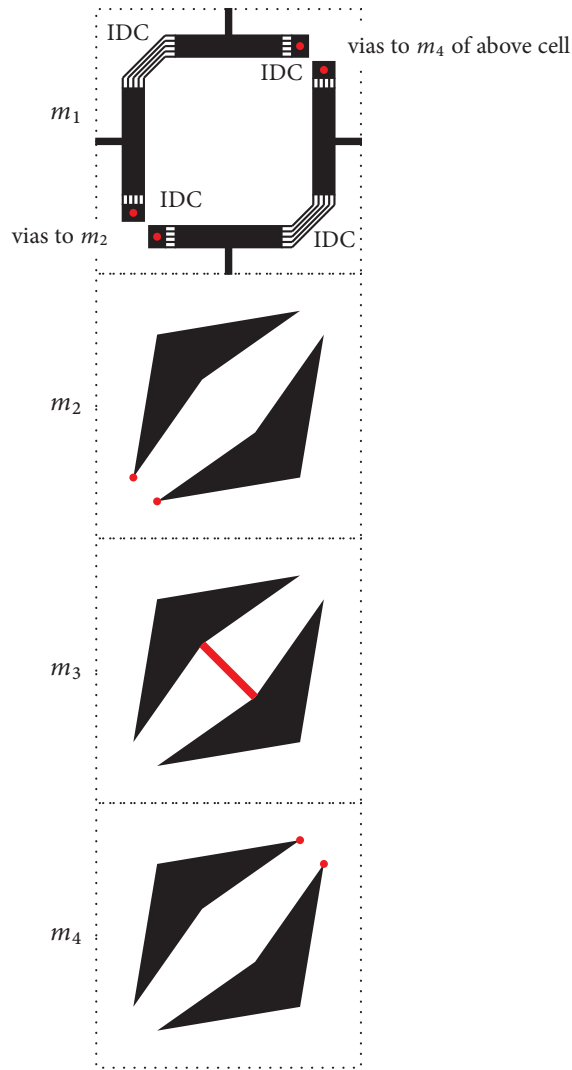
Figure 7.20: Planarised realisation of the scalar 3D metamaterial in series configuration.

8 Conclusion and Outlook

Metamaterials are compound materials exhibiting electromagnetic material parameters not readily found in nature. Several applications relying on these material parameters have been proposed in literature, e. g., novel antenna concepts, improved imaging systems, and also methods for minimising radar cross-sections.

Due to the proposed applications the synthesis of metamaterials has attracted high attention both among physicists as well as electrical engineers over the last ten years. Three main directions of research within the metamaterial synthesis field can be identified: broadband metamaterials, metamaterials operating at very high frequencies aiming for the optical spectral range, and multi-dimensional metamaterials.

In this thesis a systematic approach to the synthesis of metamaterials is presented. Group theory cannot be used for the synthesis of metamaterials, as it solely addresses the level of symmetry of a structure, but it does not determine the structure's constituents. This information can be obtained from *topological* analysis: A metamaterial is composed of cells that are small compared to the wavelength and are usually periodically continued. In general, any structure of arbitrary electrical size can be represented by a network, hence also a metamaterial unit cell. It is shown that the topologies of network representations of metamaterial cells can be derived from discretisation schemes of one-, two-, and three-dimensional space. Such schemes are commonly employed in full-wave simulators in order to *approximate* space with cells that are small compared to the wavelength, i. e., a mesh. In analogy, a metamaterial *physically realises* space that has special properties using electrically small cells. Once the network topology is determined by a space-discretising scheme, the network elements are chosen such that the desired dispersion behaviour of the metamaterial is obtained. Having a complete network description of a unit cell, physical realisations can then be designed. These can be based on lumped or distributed elements, or a combination of both. A maximally symmetric physical realisation yields isotropic behaviour, otherwise the effective material parameters are anisotropic.

Several structures presented in literature are compactly and comprehensively explained using this approach, including split-ring/wire grid setups and so-called

transmission-line metamaterial setups, both in the one-dimensional and multi-dimensional cases.

In addition, this method is used as a means of synthesis to two new types of three-dimensional metamaterials: One structure is based on the three-dimensional extension of the two-dimensional space-discretising transmission line matrix (TLM) method. This structure is of scalar nature, i. e., it yields metamaterial behaviour for one polarisation only. The second structure is based on a variation of the three-dimensional space-discretising scheme symmetrical condensed node TLM, denoted as rotated TLM (RTLM) method in literature. This RTLM metamaterial is vectorial, i. e., it achieves metamaterial behaviour for two polarisations.

A maximally symmetric physical realisation and a planar physical realisation are proposed for both the scalar and the vectorial three-dimensional metamaterial. The maximally symmetric realisations offer isotropic behaviour. They can be fabricated by standard three-dimensional techniques like injection moulding or rapid prototyping by decomposing the unit cells into polyhedra such that all metallisations lie on the polyhedra's surfaces. The planar physical realisation can be fabricated using processes common in microwave and optical engineering, but the effective material parameters are anisotropic. The proposed structures are analysed algebraically and by circuit-simulations. Full-wave simulations and experiments show that both structures have relative bandwidths of left-handed operation exceeding 20 %.

In addition to the close relation between numerical space-discretising techniques and metamaterial synthesis also an *application* proposed in literature for metamaterials has a link to numerical techniques. The geometry transformation approach which is a method suggested for the reduction of radar cross-sections is used within the FEM and FDTD methods for mesh deformations. Like in metamaterial synthesis, a numerical technique is moulded into physical realisations within this application. These two links to computational techniques suggest that further analogies could be investigated, physical realisations of *perfectly matched layers* being one of the possibilities.

A Analysis of Periodic Structures

In this appendix an introduction to the analysis of periodic structures is given. Starting from the eigenvalue problem in the case of continuous translation symmetry an analogy to periodic structures is drawn. The common framework for the analysis of multi-dimensional structures is presented, including a description of reciprocal space and an explanation of dispersion diagrams. The concept of structure functions is introduced which relates the field description (i. e., modes) to a network description. Algebraic approaches to the analysis of periodic structures based on this network description are also presented.

A.1 Formulation as an Eigenvalue Problem

This section gives a short introduction to periodic structures, emphasising the analogy between the eigenvalue problem in the continuous case and the periodic case. First, let us re-capture the essential steps to calculate wave propagation in well-known structures, specifically free space and the hollow waveguide. The steps for the analysis of a structure with *continuous translation symmetry* are, using the nabla operator $\nabla = (\partial_x, \partial_y, \partial_z)$,

Step 1: Take the homogeneous Helmholtz equation $(\nabla^2 + k^2)\Psi = 0$ or the telegrapher's equation $(\partial_{zz}^2 + k^2)\Psi = 0$. The quantity Ψ is either a field, a scalar potential, or a vector potential. 'Homogeneous' refers to the fact that no excitation terms are considered and hence an eigenvalue problem is to be solved.

Step 2: Use the ansatz that the field/potential is proportional to $\exp(-\gamma z)$ for wave propagation along z. This implies continuous translational symmetry of the problem: If the solution Ψ_0 is known at a certain plane $z_0 = 0$ then the solution at any other plane z is $\exp(-\gamma z)\Psi_0$.

Step 3: Solve the eigenvalue problem including any boundary conditions, e. g., by *separation of variables* and exploit symmetry where possible.

Step 4: Derive the dispersion relation $\gamma(\omega)$ from the eigenvalues and the characteristic impedance $Z_0(\omega)$ as the ratio of the transverse electric and magnetic field from the eigenmodes.

We will now apply these steps to a couple of example problems.

Plane wave in free space: Let us consider the trivial case of free space first.

Step 1: The Helmholtz equation for the electric field is $(\nabla^2 + k_0^2)E = 0$.

Step 2: The wave propagation ansatz yields $\partial_{zz}^2 E_0 \, \exp(-\gamma z) = -k^2 E_0 \exp(-\gamma z)$. There are no additional boundary conditions.

Step 3: For an x-polarised wave the solution is $E_x = E_{x,0} \exp(-kz)$. The related magnetic field is $H_y = H_{y,0} \exp(-kz) = E_{x,0} Z_{F0}^{-1} \exp(-kz)$ with $Z_F^2 = Z_{F0}^2 = \mu_0/\epsilon_0$.

Step 4: The dispersion relation is $\gamma(\omega) = \mathrm{j}\omega/c_0$. The characteristic impedance is $Z_F = Z_{F0}$.

Hollow waveguide: After the trivial example of a plane wave in free space let us consider TE modes in a hollow waveguide. Perfect electric walls are at $x = \pm\frac{1}{2}a$ and $y = \pm\frac{1}{2}b$. The transverse nabla operator is given by $\nabla_t = (\partial_x, \partial_y, 0)$.

Step 1: The Helmholtz equation for the magnetic field is $(\nabla^2 + k_0^2)H = 0$.

Step 2: The wave propagation ansatz together with the assumption of a TE mode yields the eigenvalue equation $\nabla_t^2 H_z = (-\gamma^2 - k_0^2)H_z$ in the longitudinal component of the magnetic field H_z. This example has boundary conditions for the electric and magnetic field at the hollow waveguide walls.

Step 3: The fundamental solution is $H_z = H_0 \sin(\pi x a^{-1}) \cdot \exp(-\gamma z)$. The transverse magnetic field components are obtained by $\gamma k_0^{-2} \nabla_t H_z$, the electric field is $E = (\mathrm{j}\omega\epsilon)^{-1} \nabla \times H$.

Step 4: The dispersion relation is $\gamma^2(\omega) = (2a)^{-2} - \omega^2 c_0^{-2}$. The characteristic impedance is $Z_0(\omega)^2 = Z_{F0}^2/(1 - (2a\omega/c_0)^{-2})$.
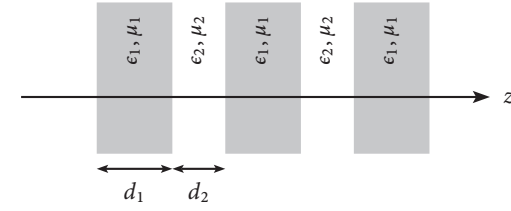

Figure A.1: Bragg lattice consisting of two materials.

Bragg lattice: Following the examples for structures with continuous translational symmetry, let us now consider periodic structures with *discrete* translational symmetry. For these, step 2 needs to be modified. In a one-dimensional periodic structure of unit cell size a the *Floquet ansatz* is used:

$$\Psi(z + a) = \Psi(a) \, \exp(-\gamma z) \tag{A.1}$$

Depending on the boundary conditions, also the derivatives of Ψ must satisfy (A.1).

We will now use a Bragg structure as an example. Here, the one-dimensional unit cell shown in Fig. A.1 consists of two materials, material i having the material parameters ϵ_i, μ_i and length d_i. The unit cell size is $a = d_1 + d_2$. Let us assume for simplicity $\omega\sqrt{\mu_1\epsilon_1}d_1/c_0 = \omega\sqrt{\mu_2\epsilon_2}d_2/c_0 = \phi$ and let us denote $Z_i^2 = \mu_i/\epsilon_i$.

Step 1: The Helmholtz equation is $(\nabla^2 + k_0^2)E = 0$.

Step 2: The Floquet ansatz is $E(z + a) = E(z) \cdot \exp(-\gamma z)$. Assuming in each medium i the field $E = u_i(z) \cdot \exp(-\gamma z)$ this yields the eigenvalue equations $u_i'' - 2\gamma u_i' + (\omega^2 c_0^{-2}\epsilon_i\mu_i + \gamma^2)u_i = 0$.

Step 3: u_i are solved for the boundary conditions $u_1(\pm\frac{1}{2}d_1) = u_2(\pm\frac{1}{2}d_1)$ and accordingly for the derivatives u_i' denoting the transverse magnetic field $u_1'(\pm\frac{1}{2}d_1) = u_2'(\pm\frac{1}{2}d_1)$.

Step 4: The non-trivial solution to the system of equations yields the dispersion relation $\left|\sin\frac{1}{2}\chi\right| = \frac{1}{2}\frac{Z_1+Z_2}{\sqrt{Z_1 Z_2}}\left|\sin\phi\right|$. The ratio of the components of the associated eigenvector yields the Bloch impedance $Z_{\mathrm{Bloch}}^2 = Z_1^2 \frac{\cos\phi - \frac{Z_1-Z_2}{Z_1+Z_2}}{\cos\phi + \frac{Z_1-Z_2}{Z_1+Z_2}}$.

As can be seen from the above example, the essential steps for calculating wave propagation behaviour remain unchanged for the periodic case[1].

In this section we assumed periodicity along the direction of propagation. The next section extends the analysis to multi-dimensional periodic structures.

A.2 Bravais Lattices and the Brillouin Zone

The geometry of a periodic structure can be described by an elementary unit cell (Wigner-Seitz cell), which can be used to reconstruct the periodic structure by translation.

These translations can be described as operations on a periodic arrangement of points in space, the so-called *Bravais lattice*. In the three-dimensional case a Bravais lattice is defined by the vector[2] $\boldsymbol{R}$

$$\boldsymbol{R} = l\boldsymbol{a}_1 + m\boldsymbol{a}_2 + n\boldsymbol{a}_3 \qquad l, m, n \in \mathbb{Z} \tag{A.2}$$

where $\boldsymbol{a}_1$, $\boldsymbol{a}_2$, $\boldsymbol{a}_3$ are vectors with $|\boldsymbol{a}_1, \boldsymbol{a}_2, \boldsymbol{a}_3| \neq 0$, i. e., these vectors span a volume. For the propagation of a plane wave through the lattice the *reciprocal lattice* vector $\boldsymbol{G}$ is of interest, defined by

$$e^{j\langle \boldsymbol{G}, \boldsymbol{R}\rangle} = 1 \tag{A.3}$$

where angle brackets denote the scalar product. Eq. (A.3) is fulfilled for

$$\langle \boldsymbol{G}, \boldsymbol{R}\rangle = 2\pi N \qquad N \in \mathbb{Z} \tag{A.4}$$

yielding

$$\boldsymbol{G} = l'\boldsymbol{b}_1 + m'\boldsymbol{b}_2 + n'\boldsymbol{b}_3 \qquad l', m', n' \in \mathbb{Z} \tag{A.5}$$

with the basis vectors of reciprocal space

$$\boldsymbol{b}_1 = 2\pi \frac{\boldsymbol{a}_2 \times \boldsymbol{a}_3}{\langle \boldsymbol{a}_1, \boldsymbol{a}_2 \times \boldsymbol{a}_3\rangle} \qquad \boldsymbol{b}_2 = 2\pi \frac{\boldsymbol{a}_3 \times \boldsymbol{a}_1}{\langle \boldsymbol{a}_1, \boldsymbol{a}_2 \times \boldsymbol{a}_3\rangle} \qquad \boldsymbol{b}_3 = 2\pi \frac{\boldsymbol{a}_1 \times \boldsymbol{a}_2}{\langle \boldsymbol{a}_1, \boldsymbol{a}_2 \times \boldsymbol{a}_3\rangle} \tag{A.6}$$

The Wigner-Seitz cell of reciprocal space is called *Brillouin zone*. Considering mirror symmetries, rotation symmetries, and inversion symmetry the volume of the Brillouin zone can be reduced to a minimum volume, the *irreducible Brillouin zone*.

---

1 A Bragg grating having sinusoidal variation of the material parameters instead of discontinuities leads to solutions in terms of *complex Mathieu functions*, see, e. g., [Affolter and Kneubühl, 1976, Russer, 2006].

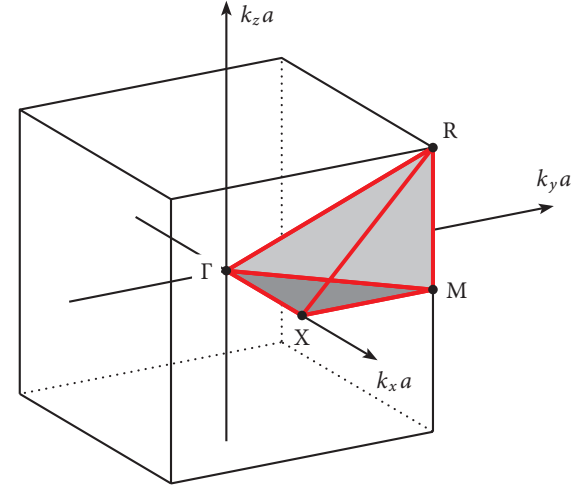2 In this subsection only, vectors are denoted by bold italics.

Figure A.2: Brillouin zone and irreducible Brillouin zone of a unit cell having simple cubic symmetry (O_h point group in Schönflies notation).

For the complete description of wave propagation in a unit cell the solutions of the wave equation for each point of the irreducible Brillouin zone is needed, i. e., a complete volume of reciprocal space needs to be sampled. In contrast, only the solutions on the edges between the vertices of the irreducible Brillouin zone are needed to describe the essential features of the structure [Ashcroft, 1988, Joannopoulos et al., 1995].

Let us consider the simple cubic lattice of edge length a. In this case the space vector $\boldsymbol{R}$ is given by (A.2)

$$\boldsymbol{R} = a \cdot \left[l\,(1,0,0) + m\,(0,1,0) + n\,(0,0,1)\right] \qquad l, m, n \in \mathbb{Z} \tag{A.7}$$

The reciprocal lattice is

$$\boldsymbol{G} = \frac{2\pi}{a} \cdot \left[l'(1,0,0) + m'(0,1,0) + n'(0,0,1)\right] \qquad l', m', n' \in \mathbb{Z} \tag{A.8}$$

The Brillouin zone and the irreducible Brillouin zone are depicted in Fig. A.2. The former is a cube of edge length 2π placed symmetrically about the Γ-point, defined by

$$\Gamma \triangleq (0,0,0) \qquad X \triangleq (\pi, 0, 0) \qquad M \triangleq (\pi, \pi, 0) \qquad R \triangleq (\pi, \pi, \pi) \tag{A.9}$$

section	χ	η	ξ
$\Gamma \to X$	$0 \to \pi$	0	0
$X \to M$	π	$0 \to \pi$	0
$M \to \Gamma$	$\pi \to 0$	$\pi \to 0$	0
$\Gamma \to R$	$0 \to \pi$	$0 \to \pi$	$0 \to \pi$
$R \to M$	π	π	$\pi \to 0$

(a)   (b)
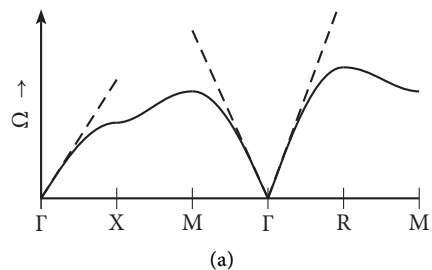
Figure A.3: (a) Showcase dispersion diagram for a simple cubic lattice (O_h point group in Schönflies notation). Solid line: dispersion relation. Dashed line: light line $\omega = |k|c_0$. (b) Edges of the irreducible Brillouin zone in a simple cubic lattice denoted by points of symmetry and the respective point in reciprocal space.

The irreducible Brillouin zone is a tetrahedron with the vertices given by (A.9). Its edges are highlighted in red in Fig. A.2.

Since each point in the Brillouin zone corresponds to a specific phase shift between opposite faces of the unit cell, a sweep of the phase shifts will sample the edges of the Brillouin zone.

A.3 Graphical Representation of the Dispersion Relation

In Sect. A.1 it was derived that the solution to the homogeneous Helmholtz equation under boundary conditions yields the dispersion relation which relates the wave vector k to frequency. In the one-dimensional case k is a scalar and therefore a graphical representation shows the scalar k versus the scalar ω. In the multidimensional case k is a vector. While for the two-dimensional case one can graphically visualise the full dispersion relation using a 3D plot, the full graphical visualisation of the dispersion relation of a three-dimensional structure would require a four-dimensional plot. The derivations made in Sect. A.2 give a solution to this visualisation problem. As it suffices to analyse only the edges between points of high symmetry in the irreducible Brillouin zone, a graphical representation of the dispersion relation can be made, called *dispersion diagram*.

As an example Fig. A.3(a) shows the dispersion diagram to the dispersion relation

$$\cos \chi + \cos \eta + \cos \xi = 3 + \tfrac{1}{2}\Omega^2 \tag{A.10}$$

with χ, η, and ξ denoting the phase shifts of a wave travelling in a unit cell along the x-, y-, and z-direction, respectively, i.e., in a simple cubic lattice. In terminology of the reciprocal lattice each point (χ, η, ξ) is element of the Brillouin zone and has an associated eigenspectrum. Solving (A.10) for Ω gives:

$$\Omega = \sqrt{2}\sqrt{3 - \cos \chi - \cos \eta - \cos \xi} \tag{A.11}$$

Calculating the eigenfrequencies for all edges (see table A.3(b)) between points of symmetry for the Brillouin zone gives the dispersion diagram shown in Fig A.3(a).

In addition to the eigenfrequencies the *light line* is denoted by a dashed line in Fig A.3(a). It is defined by $\omega = |k|c_0$ with the free-space speed of light c_0. In Fig. A.3(a) all modes are below the light line, i.e, their phase velocity is smaller than c_0. Such modes are called *guided modes*. Modes above the light line, i.e., with a phase velocity larger than c_0, radiate if the structure is open to free space. Such modes are called *leaky waves*, or, because this requires a complex propagation coefficient, *complex waves* [Ishimaru, 1991].

In order to illustrate the behaviour of guided modes and leaky modes let us consider the case of slits in a hollow waveguide and in a coaxial cable. In the former arrangement the slits lead to radiation because the phase velocity of the fundamental mode is larger than the free-space velocity. In the coaxial cable case the radiation due to the slit is smaller by orders of magnitude because the phase velocity of the fundamental mode is smaller or equal to c_0.

In closed structures no leaky modes exist. For two-dimensional arrangements a closed structure was proposed in [Stickel et al., 2007]. Three-dimensional infinitely periodic arrangements are by definition always closed.

A.4 Structure Functions

This section provides an introduction to *structure functions* which allow to rigorously relate the field description of the Helmholtz eigensolutions to a network description. Such network descriptions will prove useful for the analysis of periodic structures as can be seen in the following Sect. A.5. See [Brand, 1970, Felsen and Marcuvitz, 1994, Russer, 2006] for more information.

This approach considers each eigenmode separately. For each mode the transverse field distribution is formally factored into a *structure function* denoted by e, h, which depend on the transverse coordinates and a *generalised voltage V* and *generalised current I* which depend on the longitudinal direction. Assuming propagation in the $+z$-direction this formal separation is

$$E_t = V(z) \cdot e(x, y) \qquad\qquad H_t = I(z) \cdot h(x, y) \qquad (A.12)$$

with the structure functions $e(x, y)$ and $h(x, y)$ being vector functions having an x- and a y-component and the subscript t denoting the transverse components. The structure functions are normalised such that

$$\tfrac{1}{2} \iint E \times H^* \, \mathrm{d}A = \tfrac{1}{2} Z_F^{-1} \iint |E_t|^2 \, \mathrm{d}A = \tfrac{1}{2} Z_F \iint |H_t|^2 \, \mathrm{d}A$$
$$= \tfrac{1}{2} V \cdot I^* = \tfrac{1}{2} Z_F^{-1} |V|^2 = \tfrac{1}{2} Z_F |I|^2 \quad (A.13)$$

is satisfied with Z_F being the characteristic wave impedance of the mode and A being the transverse area of the structure under investigation. This normalisation implies that the power flows in the field description and network description match. The ratio of the generalised voltages and currents $Z_F = V(z)/I(z)$ is the wave impedance of the mode. In the case of a TEM mode one can compute the characteristic impedance $Z_0 = \sqrt{L'/C'}$ from the structure functions by

$$L' = \mu \int_{C_1} h_x \, \mathrm{d}y - h_y \, \mathrm{d}x \qquad\qquad C' = \epsilon \oint_{C_2} e_x \, \mathrm{d}y - e_y \, \mathrm{d}x \qquad (A.14)$$

with C_1 being an integration path connecting two conductors, and C_2 being an integration path encircling one conductor.

Eigenmodes to the Helmholtz equation are orthogonal[1] and therefore so are the structure functions. Together with the normalisation of structure functions expressed in (A.13) one obtains that the set of structure functions for all modes forms a bi-orthogonal basis.

In order to obtain a network description the longitudinal fields are expressed in terms of the transverse fields, i. e., generalised voltages and currents. Then Maxwell's equations transform into the transmission line equations

$$\partial_z V(z) = -Z' \cdot I(z) \qquad\qquad \partial_z I(z) = -Y' \cdot V(z) \qquad (A.15)$$

---

1 Eigenmodes are orthogonal if the operator in the eigenvalue problem is hermitian. For the Helmholtz equation this is solely possible in the loss-less case. As losses are commonly treated using a perturbation approach then eigenmodes remain orthogonal within the bounds of the approximation.

exhibiting an effective impedance per length Z' and an effective admittance per length Y'. These effective parameters fulfill for the characteristic impedance $Z_0^2 = Z'/Y'$ and for the propagation coefficient $\gamma^2 = Z'Y'$. In other words, if the expressions for the wave impedance and the propagation coefficient of a mode are known, then the network elements Z', Y' obey and thus can be alternatively computed by

$$Z' = \gamma \cdot Z_F \qquad\qquad Y' = \gamma/Z_F \qquad (A.16)$$

In case of an x-polarised plane wave propagating in free space the structure functions reduce to $e_x(x, y) = h_y(x, y) = 1$, the area of integration is the unit area and one obtains $Z' = \mathrm{j}\omega\mu$ and $Y' = \mathrm{j}\omega\epsilon$.

In order to illustrate this transformation of the field description to a network description let us consider as an example the fields of the TE$_{10}$ mode in a hollow rectangular waveguide of transverse direction $a \times b$ with the longer length a aligned with the y-axis. The fields for a wave propagating in the $+z$-direction are

$$H_x = 0 \qquad H_y = A \, \sin \frac{\pi x}{a} \, \mathrm{e}^{-\mathrm{j}kz} \qquad H_z = -\mathrm{j}\frac{\pi}{ka} A \, \cos \frac{\pi x}{a} \, \mathrm{e}^{-\mathrm{j}kz} \qquad (A.17a)$$

$$E_x = Z_{\mathrm{TE}} \, H_y \qquad E_y = 0 \qquad\qquad E_z = 0 \qquad (A.17b)$$

After defining the structure functions

$$e_x(x, y) = h_y(x, y) = \sqrt{\frac{2}{ab}} \, \sin \frac{\pi y}{a} \qquad (A.18)$$

the transverse fields can be expressed by the generalised voltage $V(z)$ and the generalised current $I(z)$ by

$$E_x = V(z) \cdot e_y(x, y) \qquad\qquad H_y = I(z) \cdot h_x(x, y) \qquad (A.19)$$

Due to the structure function definition in (A.18) the characteristic impedance relates generalised voltage to generalised current by

$$V(z) = Z_{\mathrm{TE}} \cdot I(z) \qquad (A.20)$$

Power transmission in the field description and the generalised voltage/current formulations are equal, i. e.,

$$P(z) = \tfrac{1}{2} Z_0 \iint |H_y|^2 \, \mathrm{d}A = \tfrac{1}{4} Z_{\mathrm{TE}} ab |A|^2 = \tfrac{1}{2} Z_{\mathrm{TE}} |I(z)|^2 \qquad (A.21)$$

Next the longitudinal fields need to be expressed by the generalised voltage/current. With all fields expressed by generalised voltages and currents Maxwell's equations

transform into the transmission line equations. Maxwell's equations are, in a per-component representation in Cartesian coordinates

Faraday's law:

$$(\nabla \times E)_x = \partial_y E_z - \partial_z E_y \ = -j\omega\mu H_x \tag{A.22a}$$

$$(\nabla \times E)_y = \partial_z E_x - \partial_x E_z \ = -j\omega\mu H_y \tag{A.22b}$$

$$(\nabla \times E)_z = \partial_x E_y - \partial_y E_x \ = -j\omega\mu H_z \tag{A.22c}$$

Ampère's law:

$$(\nabla \times H)_x = \partial_y H_z - \partial_z H_y \ = \ j\omega\epsilon E_x \tag{A.22d}$$

$$(\nabla \times H)_y = \partial_z H_x - \partial_x H_z \ = \ j\omega\epsilon E_y \tag{A.22e}$$

$$(\nabla \times H)_z = \partial_x H_y - \partial_y H_x \ = \ j\omega\epsilon E_z \tag{A.22f}$$

The longitudinal magnetic field H_z is related to the generalised voltage by considering the z-component of Faraday's law (A.22c), yielding

$$-\partial_y E_x = -j\omega\mu H_z \quad \rightarrow \quad H_z = V(z)\frac{j\pi}{\omega\mu a}\sqrt{\frac{2}{ab}}\cos\frac{\pi y}{a} \tag{A.23}$$

The y-component of Faraday's law (A.22b) and the x-component of Ampère's law (A.22d) yield equations of the transmission line type

$$\partial_z E_x = -j\omega\mu H_y \quad \rightarrow \quad \partial_z V(z) = -j\omega\mu I(z) \tag{A.24a}$$

$$\partial_y H_z - \partial_z H_y = \ j\omega\epsilon E_x \quad \rightarrow \quad \partial_z I(z) = -\left(j\omega\epsilon + \frac{1}{j\omega\mu(a/\pi)^2}\right)V(z) \tag{A.24b}$$

Note that in (A.24b) the H_z field is expressed in terms of the generalised voltage as determined in (A.23). By equating (A.24) and (A.15) one obtains

$$Z' = j\omega\mu \qquad\qquad Y' = j\omega\epsilon + \frac{1}{j\omega\mu(a/\pi)^2} \tag{A.25}$$

A finite segment of the rectangular hollow waveguide of length Δz can therefore be modelled by the equivalent circuit shown in Fig. A.4. Alternatively the network elements can be obtained by taking the propagation coefficient and wave impedance
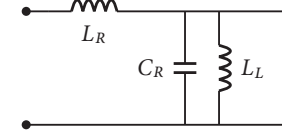

Figure A.4: Equivalent circuit of a hollow waveguide segment of length Δz in TE$_{10}$ mode with transverse dimensions $a \times b$, $a > b$. $L_R = \mu\Delta z$, $C_R = \epsilon\Delta z$, $L_L = \mu(a/\pi)^2/\Delta z$. Note that the resonance frequency of the parallel resonator matches the cut-off frequency of the mode.

of the TE$_{10}$ mode

$$\gamma = \frac{\omega}{c}\sqrt{1 - \frac{\omega_c^2}{\omega^2}} \qquad\qquad Z_F = Z_{F0}\Big/\sqrt{1 - \frac{\omega_c^2}{\omega^2}} \tag{A.26}$$

with $\omega_c = \frac{\pi}{a\sqrt{\mu\epsilon}}$ and using (A.16) in order to obtain the same network elements like in (A.25)

$$Z' = \gamma \cdot Z_F = j\omega\mu \qquad Y' = \gamma/Z_F = j\omega\epsilon + \frac{1}{j\omega\mu(a/\pi)^2} \tag{A.27}$$

A.5 Algebraic Analysis

In this section algebraic approaches to the analysis of the dispersion relation and the Bloch impedance are presented. We assume the network description of the behaviour of a single unit cell is known. While for the structures discussed within this thesis a network description is easily obtained, the situation may be more challenging in multidimensional structures including both lumped elements and distributed elements. See [Russer, 1994] for a systematic calculation approach to this general case.

In network description, one-dimensional periodic structures can be viewed as a two-port. Its chain matrix representation allows for general expressions of both the dispersion relation and the Bloch impedance. Other network representations of the unit cell can be converted into chain matrix representation. For multidimensional structures an approach based on impedance or admittance matrix based representations is suitable. Dispersion calculation in connection networks is convenient to analyse using scattering matrix representation.
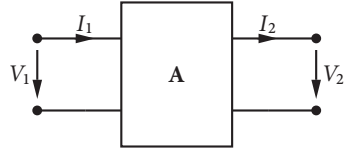
Figure A.5: Chain matrix representation of a two-port.

A.5.1 Chain Matrix based Analysis of Unit Cell Two-Ports

For the calculation of the dispersion relation of a *two-port* the representation of a *chain matrix*[1] [Matthaei et al., 1980, Russer, 2006, Pozar, 2005] is convenient. A chain matrix $\mathbf{A}$ relates voltages and currents of a two-port by

$$\begin{pmatrix} V_1 \\ I_1 \end{pmatrix} = \mathbf{A} \cdot \begin{pmatrix} V_2 \\ I_2 \end{pmatrix} \tag{A.28}$$

This two-port is depicted in Fig. A.5 with the definition of the orientation of the voltages and currents. It shall be emphasised that the current I_1 is assumed to flow into the circuit while the current I_2 is assumed to flow out of the circuit. Due to the definition of the chain matrix a concatenation of different elements can be accounted for by multiplication of their respective chain matrices. The chain matrices for a series element Z, a shunt element Y, and a piece of transmission line with characteristic impedance Z_0 and electrical length ϕ are, respectively,

$$\mathbf{A}_{\text{series}} = \begin{pmatrix} 1 & Z \\ 0 & 1 \end{pmatrix} \quad \mathbf{A}_{\text{shunt}} = \begin{pmatrix} 1 & 0 \\ Y & 1 \end{pmatrix} \quad \mathbf{A}_{\text{trans}} = \begin{pmatrix} \cos\phi & jZ_0 \sin\phi \\ jZ_0^{-1} \sin\phi & \cos\phi \end{pmatrix} \tag{A.29}$$

While reciprocal two-ports result in symmetric impedance, admittance, and scattering matrices, in chain matrix representation the condition for reciprocity is

$$|\mathbf{A}| = A_{11}A_{22} - A_{12}A_{21} = 1 \tag{A.30}$$

---

[1] Depending on the field of study other names for the chain matrix representation are 'ABCD matrix' or 'transfer matrix', sometimes even 'transmission matrix'. In particular terminology between 'transfer matrix' and 'transmission matrix' is varying among authors. Let us use the definition of the transmission matrix $\mathbf{T}$ relating wave amplitudes a_i, b_i by $\begin{pmatrix} b_1 \\ a_1 \end{pmatrix} = \mathbf{T} \cdot \begin{pmatrix} a_2 \\ b_2 \end{pmatrix}$. Then the dispersion relation can be inferred from the eigenvalues of $\mathbf{T}$. This is in analogy to the eigenvalues to the chain matrix, as will be shown within this section.

The chain matrix representation can be computed from impedance and admittance representations by

$$\mathbf{A} = \begin{pmatrix} -1 & Z_{11} \\ 0 & Z_{21} \end{pmatrix}^{-1} \begin{pmatrix} 0 & Z_{12} \\ 1 & Z_{22} \end{pmatrix} = \begin{pmatrix} Y_{11} & -1 \\ -Y_{21} & 0 \end{pmatrix}^{-1} \begin{pmatrix} Y_{12} & 0 \\ -Y_{22} & -1 \end{pmatrix} \tag{A.31}$$

If a two-port described by a chain matrix $\mathbf{A}$ is periodically continued then $\mathbf{A}$ describes a unit cell. Assuming wave propagation in this structure with a complex propagation constant γ and the unit cell size having the physical thickness a, then the Floquet ansatz is

$$\begin{pmatrix} V_1 \\ I_1 \end{pmatrix} = e^{\gamma a} \begin{pmatrix} V_2 \\ I_2 \end{pmatrix} = \mathbf{A} \begin{pmatrix} V_2 \\ I_2 \end{pmatrix} \tag{A.32}$$

Eq. (A.32) is an eigenvalue problem with the eigenvalue $\lambda = \exp(\gamma a)$. The characteristic polynomial of $\mathbf{A}$ is

$$\lambda^2 - \lambda\left(A_{11} + A_{22}\right) + A_{11}A_{22} - A_{12}A_{21} = 0 \tag{A.33}$$

Due to (A.30) it reads for the reciprocal case

$$\lambda^2 - \lambda\left(A_{11} + A_{22}\right) + 1 = 0 \tag{A.34}$$

The roots of the characteristic polynomial are the eigenvalues $\lambda^{(\pm)}$. These constitute the dispersion relation

$$\lambda^{(\pm)} = \exp(\gamma^{(\pm)}a) = \tfrac{1}{2}(A_{11} + A_{22}) \pm \sqrt{\tfrac{1}{4}(A_{11} + A_{22})^2 - 1} \tag{A.35}$$

Considering the definition of hyperbolic functions one obtains for both eigensolutions

$$\cosh\gamma a = \tfrac{1}{2}(A_{11} + A_{22}) \tag{A.36a}$$

or, equivalently

$$\sinh^2(\tfrac{1}{2}\gamma a) = \tfrac{1}{4}(A_{11} + A_{22}) - \tfrac{1}{2} \tag{A.36b}$$

The latter expression for the dispersion relation may in some cases be more useful and is used in chapters 3, 4, and 5. The corresponding two eigenvectors to $\lambda^{(\pm)}$ are $(V_{\lambda^{(\pm)}}, I_{\lambda^{(\pm)}})$. The ratio $V_{\lambda^{(\pm)}}/I_{\lambda^{(\pm)}}$ is called the *Bloch impedance*. Its values are

$$Z_{\text{Bloch}}^{(+)} = \frac{V_{\lambda^{(+)}}}{I_{\lambda^{(+)}}} = \frac{A_{12}}{\tfrac{1}{2}(A_{22} - A_{11}) + \sqrt{\tfrac{1}{4}(A_{11} + A_{22})^2 - 1}} \tag{A.37a}$$

$$Z_{\text{Bloch}}^{(-)} = \frac{V_{\lambda^{(-)}}}{-I_{\lambda^{(-)}}} = \frac{-A_{12}}{\tfrac{1}{2}(A_{22} - A_{11}) - \sqrt{\tfrac{1}{4}(A_{11} + A_{22})^2 - 1}} \tag{A.37b}$$

The definition of the Bloch impedance for the $\lambda^{(-)}$ eigensolution takes a negative current due to the definition of currents in Fig. A.5.

In case of a symmetric unit cell the chain matrix satisfies $A_{11} = A_{22}$. The dispersion relation (A.35) and Bloch impedance (A.37) then simplify to

$$\exp(\gamma^{(\pm)} a) = A_{11} \pm \sqrt{A_{11}^2 - 1} \qquad \rightarrow \qquad \cosh \gamma a = A_{11} \tag{A.38a}$$

$$Z_{\mathrm{Bloch}}^{(\pm)} = \frac{A_{12}}{\sqrt{A_{11}^2 - 1}} = \sqrt{\frac{A_{12}}{A_{21}}} \tag{A.38b}$$

The physical interpretation of the above derivations is as follows: The Floquet ansatz transforms the problem into an eigenvalue problem. The eigenvalue yields the propagation coefficient γ and thus the dispersion relation, the corresponding eigenvector denotes the associated voltage and current waves. Their ratio, the *Bloch impedance*, is the analogon to the characteristic impedance for a continuous transmission line. In fact, describing a piece of transmission line by $\mathbf{A}_{\mathrm{trans}}$ as denoted in (A.29), the Bloch impedance equals the characteristic impedance, $Z_{\mathrm{Bloch}} = \sqrt{A_{12}/A_{21}} = Z_0$. Thus one can consider the Bloch impedance not only an analogon to the characteristic impedance, but a generalisation for the case of *arbitrary* translational symmetry.

In the loss-less case the propagation constant is either purely real or purely imaginary. While the former case describes a stop-band, i. e., evanescent waves, the latter describes a pass-band, i. e., propagating waves. For the pass-band case one obtains

$$\cosh \gamma a = \cosh \mathrm{j} \chi = \cos \chi = \tfrac{1}{2}(A_{11} + A_{22}) \tag{A.39a}$$

$$\sinh^2\left(\tfrac{1}{2}\gamma a\right) = \sinh^2\left(\mathrm{j}\tfrac{1}{2}\chi\right) = -\sin^2 \tfrac{1}{2}\chi = \tfrac{1}{4}\left(A_{11} + A_{22}\right) - \tfrac{1}{2} \tag{A.39b}$$

The edges of the pass-band are determined by $|\cos \chi| = 1$, within the pass-band one has $|\cos \chi| = \tfrac{1}{2}|A_{11} + A_{22}| < 1$.

It has to be noted that the Bloch impedance is different for the two eigensolutions for the general case of an asymmetric cell, i. e., one observes a different voltage to current ratio for waves propagating in opposite directions. On the other hand, in case of a symmetric cell the Bloch impedance is independent on the direction of wave propagation. If such a unit cell is terminated on one side with the Bloch impedance, then the resulting input impedance is also the Bloch impedance. This effect is called *image impedance* in filter theory and shown in Fig. A.6.

$$V_1/I_1 = Z_{\mathrm{Bloch}} \overset{!}{=} \frac{A_{11} Z_{\mathrm{Bloch}} + A_{12}}{A_{21} Z_{\mathrm{Bloch}} + A_{11}} \qquad \rightarrow \qquad Z_{\mathrm{Bloch}} = \sqrt{\frac{A_{12}}{A_{21}}} \tag{A.40}$$
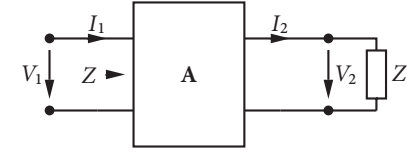

Figure A.6: Image impedance principle: Termination of a symmetric two-port $\mathbf{A}$ by the impedance Z_L. For termination with the Bloch impedance, $Z_L = Z_{\mathrm{Bloch}}$ the input impedance equals the terminating Bloch impedance, $Z = Z_{\mathrm{Bloch}}$.
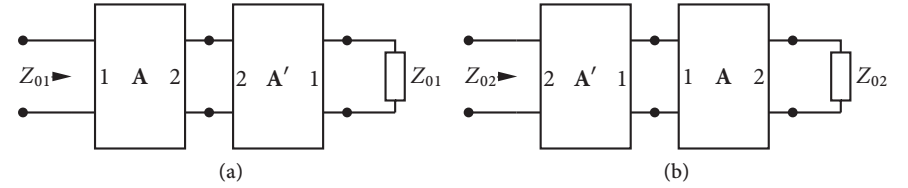

Figure A.7: Concatenation of an asymmetric unit cell with its mirrored unit cell yielding a symmetric cell. (a) Concatenation at port 2, and (b) concatenation at port 1.

The expressions for the Bloch impedance in (A.40) and (A.38b) match. For wave propagation along a structure with continuous translational symmetry the situation is equivalent: If a transmission line is terminated with its characteristic impedance then the input impedance again matches the characteristic impedance.

While the equation for the Bloch impedance in the asymmetric case of (A.37) equals the result presented in [Pozar, 2005] – albeit derived using another approach – in some publications the case of asymmetric cells is treated differently, e. g., in [Matthaei et al., 1980, Schüßler, 1990, Russer, 2006]. There the asymmetric unit cell is symmetrised: A new unit cell – which describes a different topology – is considered which consists of the asymmetric unit cell and its mirrored unit cell $\mathbf{A}'$ (i. e., the two-port we obtain by exchanging the two ports). The two possibilities for the resulting symmetrised unit cells are shown in Fig. A.7. Periodically continuing both types of symmetrised unit cells shows that the resulting topologies are the same but the port terminals are situated at different reference planes. As the Bloch impedance depends on the reference plane one yields the Bloch impedances
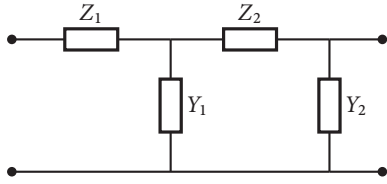
Figure A.8: Example of an asymmetric unit cell that cannot be symmetrised.

for each case

$$Z_{01} = \sqrt{\frac{A_{11}A_{12}}{A_{21}A_{22}}} \qquad\qquad Z_{02} = \sqrt{\frac{A_{22}A_{12}}{A_{21}A_{11}}} \qquad (A.41a)$$

It shall be noted that the impedances in (A.41) differ from (A.37) because essentially different unit cells are considered. An example of a topology where this symmetrisation not only yields a shift of reference planes but also a different topology is shown in Fig. A.8.

A.5.2 Scattering Matrix based Analysis of Unit Cell Two-Ports

In microwave engineering a port-based description of device behaviour is often based on scattering parameters, both in simulations and measurements. In this section it is assumed that the scattering parameters of a single unit cell are known and periodic continuation can be described by coupling of adjacent cells through ports. In this case the dispersion relation and the Bloch impedance can be inferred from the scattering parameters of a single unit cell. As was shown in Sect. A.5.1, these two quantities can be expressed in terms of chain matrix parameters of a single unit cell. Therefore here conversion of scattering parameters to chain matrix parameters is proposed. The chain matrix representation can be obtained from the scattering matrix by

$$\mathbf{A} = -\begin{pmatrix} (1-s_{11})g_1^{-1} & -(1+s_{11})g_1 \\ -s_{21}g_1^{-1} & -s_{21}g_1 \end{pmatrix}^{-1} \cdot \begin{pmatrix} -s_{12}g_2^{-1} & s_{12}g_2 \\ (1-s_{22})g_2^{-1} & (1+s_{22})g_2 \end{pmatrix} \quad (A.42)$$

with g_i describing the square root of the normalisation impedance at port i. Assuming equal port normalisation impedances $g_1^2 = g_2^2$ as well as reciprocity, i. e., $s_{12} = s_{21}$, then the expressions for the dispersion relation and Bloch impedance

are

$$\cos\chi = \tfrac{1}{2}(A_{11} + A_{22}) = \frac{1 + s_{21}^2 - s_{11}s_{22}}{2s_{21}} \qquad (A.43a)$$

$$\sin^2\tfrac{1}{2}\chi = \tfrac{1}{2} - \tfrac{1}{4}(A_{11} + A_{22}) = \frac{s_{11}s_{22} - (1 - s_{21})^2}{4s_{21}} \qquad (A.43b)$$

$$Z_{\text{Bloch}}^{(\pm)}/Z_0 = \frac{\pm A_{12}}{\tfrac{1}{2}(A_{22} - A_{11}) \pm \sqrt{\tfrac{1}{4}(A_{11} + A_{22})^2 - 1}}$$

$$= \frac{1 - s_{21}^2 + s_{11} + s_{22} + s_{11}s_{22}}{s_{22} - s_{11} \pm \sqrt{(1 + s_{21})^2 - s_{11}s_{22}}\sqrt{(1 - s_{21})^2 - s_{11}s_{22}}} \qquad (A.43c)$$

with $Z_0 = g_i^2$ being the normalisation impedance of the scattering parameters. For the symmetric case, i. e., $s_{11} = s_{22}$, one obtains

$$\cos\chi = A_{11} = \frac{1 + s_{21}^2 - s_{11}^2}{2s_{21}} \qquad (A.44a)$$

$$\sin^2\tfrac{1}{2}\chi = \tfrac{1}{2}(1 - A_{11}) = \frac{s_{11}^2 - (1 - s_{21})^2}{4s_{21}} \qquad (A.44b)$$

$$Z_{\text{Bloch}}/Z_0 = \sqrt{\frac{A_{12}}{A_{21}}} = \frac{\sqrt{(s_{11} + 1)^2 - s_{21}^2}}{\sqrt{(s_{11} - 1)^2 - s_{21}^2}} \qquad (A.44c)$$

The scattering parameters s_{ij} in (A.43) and (A.44) are those obtained from measurement or simulation, so the normalisation impedance Z_0 is usually 50 Ω.

Relating scattering parameters to the dispersion relation and to the Bloch impedance has been frequently proposed in literature, e. g., in [Smith et al., 2002a, Chen et al., 2004]. These derivations directly tackle the transmission line equations. This slightly less abstract point of view leads to lengthy derivations that are usually restricted to the symmetric case in order to keep a compact representation of intermediate expressions. The ambiguity of the complex exponential due to $\exp(j2\pi) = 1$ further complicates this derivation. On the other hand, the chain matrix derivation and its subsequent transformation to scattering parameters avoids these ambiguities while keeping a compact representation.

A.5.3 Impedance/Admittance Matrix based Analysis of Unit Cell Multi-Ports

In the Secs. A.5.1 and A.5.2 eigenvalue problems for one-dimensional structures were treated. Eigenvalue problems for a multi-dimensional periodic structure with

lumped elements are most easily solved with an impedance matrix $\mathbf{Z}$ or admittance matrix $\mathbf{Y}$. Here, only the former will be used.

The impedance matrix relates currents to voltages at the ports of the unit cell by

$$V = \mathbf{Z} \cdot I \qquad (A.45)$$

Assuming that two ports representing negative and positive directions of space have port numbers i and $i + n$, the Floquet ansatz is

$$V_i = \begin{cases} v_i \; \exp(+\frac{1}{2}k_i a_i) & \text{for } 1 \leq i \leq n \\ v_{i-n} \; \exp(-\frac{1}{2}k_{i-n} a_{i-n}) & \text{for } n+1 \leq i \leq 2n \end{cases} \qquad (A.46a)$$

$$I_i = \begin{cases} i_i \; \exp(+\frac{1}{2}k_i a_i) & \text{for } 1 \leq i \leq n \\ -i_{i-n} \; \exp(-\frac{1}{2}k_{i-n} a_{i-n}) & \text{for } n+1 \leq i \leq 2n \end{cases} \qquad (A.46b)$$

The unit cell size in direction i is denoted by a_i. Inserting (A.46) into (A.45) yields a homogeneous system of equations in v_i and i_i of dimension $2n$. Solving for the non-trivial solution of this system one obtains the dispersion relation. The non-trivial solution can be obtained by re-writing the system of equations into a system in v_i, i_i. Setting the determinant to this system equal to zero yields the non-trivial solution. Within the scope of this thesis the following abbreviations are used

$$k_1 a_1 = \chi \qquad\qquad k_2 a_2 = \eta \qquad\qquad k_3 a_3 = \xi \qquad (A.47)$$

The physical meaning of χ, η, ξ are the phase shifts of a wave travelling through the structure.

The above derivations can be performed for the admittance based description of a unit cell by inserting the Floquet ansatz (A.46) into $I = \mathbf{Y} \cdot U$ and then solving likewise for the non-trivial solution in v_i, i_i.

As an example let us consider the one-dimensional case of the symmetric one-port depicted in Fig. 3.1(b). Its impedance matrix is

$$\mathbf{Z} = \tfrac{1}{2}Z \cdot \mathbf{I} + \frac{1}{Y} \cdot \mathbf{1} \qquad (A.48)$$

as denoted in (3.31a). The Floquet ansatz (A.46) in this one-dimensional case is

$$V_1 = v_1 \exp(\tfrac{1}{2}\chi) \qquad\qquad V_2 = v_1 \; \exp(-\tfrac{1}{2}\chi) \qquad (A.49a)$$
$$I_1 = i_1 \exp(\tfrac{1}{2}\chi) \qquad\qquad I_2 = -i_1 \; \exp(-\tfrac{1}{2}\chi) \qquad (A.49b)$$

The system of equations in v_1, i_1 resulting from $V = \mathbf{Z} \cdot I$ is

$$\begin{pmatrix} \exp(-\frac{1}{2}\chi) & +\frac{1}{2}Z\exp(-\frac{1}{2}\chi) - Y^{-1}[\exp(+\frac{1}{2}\chi) - \exp(-\frac{1}{2}\chi)] \\ \exp(+\frac{1}{2}\chi) & -\frac{1}{2}Z\exp(+\frac{1}{2}\chi) - Y^{-1}[\exp(+\frac{1}{2}\chi) - \exp(-\frac{1}{2}\chi)] \end{pmatrix} \cdot \begin{pmatrix} v_1 \\ i_1 \end{pmatrix} = 0 \quad (A.50)$$

The determinant to (A.50) is

$$-Z - Y^{-1}[2 - \exp(+\chi) - \exp(-\chi)] = -Z - 2Y^{-1}(1 - \cos\chi) \qquad (A.51)$$

Setting this determinant to zero solves for the non-trivial solution and yields

$$\cos\chi = 1 + \tfrac{1}{2}ZY \qquad\qquad \sin^2\tfrac{1}{2}\chi = -\tfrac{1}{4}ZY \qquad (A.52)$$

This is the same result as (3.5) which was obtained by chain matrix analysis.

As the determinant of a system of equations is equal to the product of its eigenvalues, the dispersion relation forces the eigenvalues to zero. Like in Sect. A.5.1 the corresponding eigenvectors yield the associated voltage and current with their ratio being equal to the Bloch impedance.

A.5.4 Scattering Matrix based Analysis of Unit Cell Multi-Ports

In pure connection networks no impedance/admittance matrix is available: Their scattering matrix representation $\mathbf{S}$ has eigenvalues ± 1, and hence the term $(\mathbf{S}\pm 1)^{-1}$ which is needed for conversion to impedance or admittance matrix representation is singular, see [Russer, 2006].

In order to calculate the dispersion relation from the scattering matrix the *connection matrix* $\mathbf{\Gamma}$ needs to be set up, which accounts for the periodic boundary conditions. As the name suggests, the connection matrix determines which ports connect to adjacent cells upon periodic continuation. For a rectilinear unit cell with port m being connected to port n we have

$$\mathbf{\Gamma}_{mn} = \exp(+jk_i a_i) \qquad\qquad \mathbf{\Gamma}_{nm} = \exp(-jk_i a_i) \qquad (A.53)$$

Other elements of the connection matrix are zero. The eigenvalues of the product $\mathbf{S\Gamma}$ determine the dispersion relation, similar to the chain matrix based analysis presented in Sect. A.5.1.

As an example let us consider the dispersion of the two-dimensional TLM node [Krumpholz and Russer, 1994] described by (4.1) and repeated here for convenience

$$\mathbf{S} = \tfrac{1}{2}\exp(-j\phi) \; (\mathbf{1} - 2\cdot\mathbf{I}) \qquad (A.54)$$

The connection matrix

$$\Gamma = \begin{pmatrix} 0 & \exp(+j\chi) & 0 & 0 \\ \exp(-j\chi) & 0 & 0 & 0 \\ 0 & 0 & \exp(+j\eta) & 0 \\ 0 & 0 & 0 & \exp(-j\eta) \end{pmatrix} \tag{A.55}$$

states that port 1 is connected to port 2, and port 3 to port 4. The eigenvalues λ of $\mathbf{S}\Gamma$ are

$$\lambda_1 = +1 \qquad\qquad \lambda_2 = -1 \tag{A.56a}$$

$$\lambda_3 = \exp(+j\phi) \qquad\qquad \lambda_4 = \exp(-j\phi) \tag{A.56b}$$

with

$$\cos\phi = \tfrac{1}{2}\cos\chi + \tfrac{1}{2}\cos\eta = \cos\tfrac{1}{2}(x+y)\ \cos\tfrac{1}{2}(x-y) \tag{A.57}$$

The solutions λ_1 in (A.56a) represent the magneto-static case, while λ_2 is a spurious and oscillating solution. The solutions in (A.56b) and therefore (A.57) describe the sought dispersion relation with the phase shift being a function of frequency.

Assuming right-handed behaviour, we obtain $\phi \propto \omega$. A Taylor series of the cosine terms in (A.57) yields

$$\frac{\omega^2}{c^2} = k_x^2 + k_y^2 \tag{A.58}$$

which is the two-dimensional wave equation with phase velocity c.

B IIR Filter Coefficients

The feedback and feed-forward IIR coefficients in (6.26) are found by identification of the coefficients of z^{-i} in the numerator and denominator of the expressions $V_{\rho,i}(z)$ and $V_{\tau,i}(z)$. The required calculations are tedious, but are straightforward algebraic manipulations. One obtains for the backward coefficients of both the reflection and transmission filters

$$\begin{pmatrix} a_1 \\ a_2 \\ a_3 \\ a_4 \\ a_5 \\ a_6 \\ a_7 \end{pmatrix} = \begin{pmatrix} 4 & 4 & 1 & 4 & 1 & 4 & 4 \\ 24 & 16 & 2 & 0 & -2 & -16 & -24 \\ 60 & 20 & -1 & -12 & -1 & 20 & 60 \\ 80 & 0 & -4 & 0 & 4 & 0 & -80 \\ 60 & -20 & -1 & 12 & -1 & -20 & 60 \\ 24 & -16 & 2 & 0 & -2 & 16 & -24 \\ 4 & -4 & 1 & -4 & 1 & -4 & 4 \end{pmatrix} \cdot \begin{pmatrix} 1 \\ f_1 k \\ f_2 k^2 \\ f_3 k^3 \\ f_4 k^4 \\ f_5 k^5 \\ f_6 k^6 \end{pmatrix}, \tag{B.1}$$

with the abbreviations

$$f_1 = Z_0 C_L \tag{B.2a}$$

$$f_2 = 8C_L L_L + 8L_R C_L + Z_0^2 C_L^2 + 4C_R L_L \tag{B.2b}$$

$$f_3 = Z_0 C_L^2 L_R + Z_0 C_L C_R L_L + Z_0 C_L^2 L_L \tag{B.2c}$$

$$f_4 = C_L \left(8 L_L L_R (C_R + C_L) + 4L_R^2 C_L + Z_0^2 L_L C_L C_R \right) \tag{B.2d}$$

$$f_5 = Z_0 C_L^2 L_R C_R L_L \tag{B.2e}$$

$$f_6 = L_R^2 C_L^2 C_R L_L \tag{B.2f}$$

The forward reflection coefficients are found as

$$\begin{pmatrix} b_{r,1} \\ b_{r,2} \\ b_{r,3} \\ b_{r,4} \\ b_{r,5} \\ b_{r,6} \\ b_{r,7} \end{pmatrix} = \begin{pmatrix} 4 & 1 & 1 & 4 \\ 24 & 2 & -2 & -24 \\ 60 & -1 & -1 & 60 \\ 80 & -4 & 4 & -80 \\ 60 & -1 & -1 & 60 \\ 24 & 2 & -2 & -24 \\ 4 & 1 & 1 & 4 \end{pmatrix} \cdot \begin{pmatrix} 1 \\ g_2 k^2 \\ g_4 k^4 \\ g_6 k^6 \end{pmatrix}, \tag{B.3}$$

with the abbreviations

$$g_2 = 8L_R C_L - Z_0^2 C_L^2 + 8C_L L_L + 4C_R L_L \qquad \text{(B.4a)}$$

$$g_4 = -Z_0^2 C_L^2 C_R L_L + 4L_R^2 C_L^2 + 8L_L L_R C_L (C_R + C_L) \qquad \text{(B.4b)}$$

$$g_6 = L_R^2 L_L C_L^2 C_R \qquad \text{(B.4c)}$$

The forward transmission coefficients $b_{t,i}$ are found as

$$b_{t,1} = -\tfrac{1}{3} b_{t,3} = \tfrac{1}{3} b_{t,5} = -b_{t,7} = 2Z_0 k^3 C_L^2 L_L \qquad \text{(B.5a)}$$

$$b_{t,2} = b_{t,4} = b_{t,6} = 0. \qquad \text{(B.5b)}$$

List of Symbols

Symbol	Description
a	incident wave amplitude vector
b	scattered wave amplitude vector
B	magnetic flux density vector
C	capacitance
c_0	Free space speed of light
c_{phase}	phase velocity
c_{group}	group velocity
D	electric flux density vector
E	electric field vector
e	electric structure function
f	frequency
H	magnetic field vector
h	magnetic structure function
I	current
J	current density vector
J_A	surface current density vector
g	characteristic impedance square root
k	wave vector
L	inductance
$M_{e,A}$	electric surface polarisation
$M_{m,A}$	magnetic surface polarisation
n	refractive index
P	power
S	Poynting vector
V	voltage
W	energy
Y	admittance
Z_0	characteristic impedance
Z_{Bloch}	Bloch impedance
Z_F	wave impdeance
Z_{F0}	free-space wave impdeance

ϵ	permittivity
ϵ_r	relative permittivity
ϵ_{eff}	effective relative permittivity
ϵ_∞	relative permittivity for $\omega \to \infty$
γ	complex propagation coefficient
λ	wavelength
μ	permeability
μ_r	relative permeability
μ_{eff}	effective relative permeability
μ_∞	relative permeability for $\omega \to \infty$
ω	angular frequency
$\omega_{0,\epsilon}$	angular electric plasmon frequency
$\omega_{0,\mu}$	angular magnetic plasmon frequency
Ω	normalised angular frequency
Ω_0	normalised angular plasmon frequency in the resonance-balanced case
$\Omega_{0,\epsilon}$	normalised angular electric plasmon frequency
$\Omega_{0,\mu}$	normalised angular magnetic plasmon frequency
Ω_L	normalised angular lower cut-off frequency in a double Drude medium
Ω_R	normalised angular upper cut-off frequency in a double Drude medium
ϕ	phase angle
ρ_A	electric area charge density
θ	angle
χ, η, ξ	phase shifts of a plane wave across a unit cell
χ_Γ	phase shift along a principal direction for the vicinity of the Γ-point
P	off-diagonal impedance matrix elements of the RTLM cell
Q	basis change matrix
S	scattering matrix
Y	admittance matrix
Z	impedance matrix
0	null matrix
1	matrix with all elements equal to one
I	identitymatrix
∂_v	derivation with respect to v
∇	nabla operator
∇_t	transverse nabla operator
$\langle a, b \rangle$	scalar product of a and b
$\times$	vector product
$\star$	convolution operator

List of Figures

Bibliography

[Affolter and Kneubühl, 1976] Affolter, E. and Kneubühl, F. (1976). Theory of distributed feedback lasers on the basis of the complex mathieu equation. *Zeitschrift für Angewandte Mathematik und Physik*, 27(4):512–516.

[Alitalo et al., 2006a] Alitalo, P., Maslovski, S., and Tretyakov, S. (2006a). Experimental verification of the key properties of a three-dimensional isotropic transmission-line superlens. *J. Appl. Physics*, 99:124910–1–124910–6.

[Alitalo et al., 2006b] Alitalo, P., Maslovski, S., and Tretyakov, S. (2006b). Near-field enhancement and imaging in double planar polariton-resonant structures: Enlarging superlens. *Phys. Lett. A*, 357:397.

[Alitalo et al., 2006c] Alitalo, P., Maslovski, S., and Tretyakov, S. (2006c). Three-dimensional isotropic perfect lens based on LC-loaded transmission lines. *J. Appl. Physics*, 99:064912–1–064912–8.

[Alù and Engheta, 2005] Alù, A. and Engheta, N. (2005). Achieving transparency with plasmonic coatings. *Phys. Rev. B*, 72:016623.

[Armenta and Sarris, 2008] Armenta, R. A. and Sarris, C. D. (2008). A general method for introducing nonuniform grids into high-order FDTD methods: Formulation and microwave applications. *2008 Int. Microwave Symposium Digest, Atlanta, Georgia*, pages 1365–1368.

[Ashcroft, 1988] Ashcroft, N. W. (1988). *Solid State Physics*. Aaunders College.

[Baena et al., 2005] Baena, J. D., Bonache, J., Martín, F., Marqués-Sillero, R., Falcone, F., Lopetegi, T., Laso, M. A. G., García-García, J., Gil, I., Flores-Portillo, M., and Sorolla, M. (2005). Equivalent-circuit models for split-ring resonators and complementary split-ring resonators coupled to planar transmission lines. *IEEE Microwave Theory & Techniques*, 53(4):1451–1460.

[Baena et al., 2007] Baena, J. D., Jelinek, L., and Marqués, R. (2007). Towards a systematic design of isotropic bulk magnetic metamaterials using the cubic point groups of symmetry. *Phys. Rev. B*, 76(24):245115.

[Balmain et al., 2003] Balmain, K. G., Lüttgen, A. A. E., and Kremer, P. C. (2003). Power flow for resonance cone phenomenon in planar anisotropic metamaterials. *IEEE Trans. Antennas Propagat.*, 51(10):2612.

[Belevitch, 1968] Belevitch, V. (1968). *Classical network theory*. Holden-Day, San Francisco, California.

[Beruete et al., 2007] Beruete, M., Campillo, I., Navarro-Cía, M., Falcone, F., and Ayza, M. S. (2007). Molding left- or right-handed metamaterials by stacked cutoff metallic hole arrays. *IEEE Trans. Microw. Theory Tech.*, 55(6):1514–1521.

[Born et al., 1999] Born, M., Wolf, W., and Bhatia, A. B. (1999). *Principles of Optics: Electromagnetic Theory of Propagation, Interference and Diffraction of Light*. Cambridge University Press, 7 edition.

[Brand, 1970] Brand, H. (1970). *Schaltungslehre linearer Mikrowellennetze*. Hirzel, Stuttgart.

[Brillouin, 1953] Brillouin, L. (1953). *Wave Propagation in Periodic Structures*. Dover, New York.

[Cai et al., 2007] Cai, W., Chettiar, U. K., Kildishev, A. V., and Shalaev, V. M. (2007). Nonmagnetic cloak with minimized scattering. *Appl. Phys. Lett.*, 91:111105.

[Caloz and Itoh, 2002] Caloz, C. and Itoh, T. (2002). Application of the transmission line theory of lefthanded (LH) materials to the realization of a microstrip LH transmission line. *IEEE AP-S Int. Symp. Dig.*, 2:412.

[Caloz and Itoh, 2006] Caloz, C. and Itoh, T. (2006). *Electromagnetic Metamaterials*. Wiley.

[Caloz et al., 2003] Caloz, C., Sanada, A., and Itoh, T. (2003). A novel composite right/left-handed coupled-line directional coupler with arbitrary coupling level and broad bandwidth. *IEEE Trans. Microw. Theory Tech.*, 52(3):980.

[Casse et al., 2006] Casse, B. D. F., Moser, H. O., Jian, L. K., Bahou, M., Wilhelmi, O., Saw, B. T., and Gu, P. D. (2006). Fabrication of 2d and 3d electromagnetic metamaterials for the terahertz range. *Journal of Physics: Conference Series*, 34:885.

[Cauer, 1954] Cauer, W. (1954). *Theorie der linearen Wechselstromschaltungen*. Akademie-Verlag, Berlin.

[Chen and Chan, 2007] Chen, H. and Chan, C. T. (2007). Acoustic cloaking in three dimensions using acoustic metamaterials. *Appl. Phys. Lett.*, 91:183518.

[Chen et al., 2004] Chen, X., Grzegorczyk, T. M., Wu, B. I., Pacheco, J., and Kong, J. A. (2004). Robust method to retrieve the constitutive effective parameters of metamaterials. *Phys. Rev. E*, 70:016608.

[Collin, 1990] Collin, R. E. (1990). *Field Theory of Guided Waves*. IEEE Press, 2 edition.

[Culhaoglu et al., 2008] Culhaoglu, A. E., Zedler, M., Hoefer, W. J. R., Osipov, A., and Russer, P. (2008). Full-wave numerical simulation of a finite 3d metamaterial lens. *Proc. ACES, Niagara Falls, Canada*, pages 989–994.

[Cummer et al., 2006] Cummer, S. A., Popa, B. I., Schurig, D., and Smith, D. R. (2006). Full-wave simulations of electromagnetic cloaking structures. *Phys. Rev. E*, 74:036621.

[Cummer and Schurig, 2006] Cummer, S. A. and Schurig, D. (2006). One path to acoustic cloaking. *New Journal of Physics*, 9(45):1–8.

[Damm et al., 2007] Damm, C., Frese, J., Schüßler, M., and Jakoby, R. (2007). Electrically controllable artificial transmission line transformer for matching purposes. *IEEE Trans. Microw. Theory Tech.*, 55(6):accepted for publication.

[Dollinger et al., 2007] Dollinger, G., Wegener, M., Soukoulis, G. M., and Linden, S. (2007). Negative-index metamaterial at 780 nm wavelength. *Optics Letters*, 32:53.

[Eberhardt et al., 2006] Eberhardt, W., Ahrendt, D., Keßler, U., Warkentin, D., and Kück, H. (2006). Polymer based multifunctional 3d-packages for microsystems. *Proceedings of the 2nd International Conference on Multi-Material Micro Manufacture (4M)*.

[Eleftheriades and Balmain, 2005] Eleftheriades, G. and Balmain, K., editors (2005). *Negative-Refraction Metamaterials*. Wiley.

[Eleftheriades et al., 2002] Eleftheriades, G. V., Iyer, A. K., and Kremer, P. C. (2002). Planar negative refractive index media using periodically L-C loaded transmission lines. *IEEE Trans. Microw. Theory Tech.*, 50(12):2702.

[Eleftheriades and Siddiqui, 2005] Eleftheriades, G. V. and Siddiqui, O. F. (2005). Negative refraction and focussing in hyperbolic transmission-line periodic grids. *IEEE Trans. Microwave Theory Techn.*, 53:396.

[Engheta and Ziolkowski, 2005] Engheta, N. and Ziolkowski, R. W. (2005). A positive future for double-negative metamaterials. *IEEE Trans. Microwave Theory Tech, Special Issue on Metamaterial Structures, Phenomena, and Applications*, 53:1535.

[Engheta and Ziolkowski, 2006] Engheta, N. and Ziolkowski, R. W. (2006). *Electromagnetic Metamaterials*. Wiley.

[Fang et al., 2005] Fang, N., Lee, H., Sun, C., and Zhang, X. (2005). Sub-diffraction-limited optical imaging with a silver superlens. *Science Magazine*, 308:534.

[Felsen and Marcuvitz, 1994] Felsen, L. B. and Marcuvitz, N. (1994). *Radiation and Scattering of Waves*. IEEE Press.

[Forschungsvgg. Räumliche Elektronische Baugruppen 3-D MID e.V., 2004] Forschungsvgg. Räumliche Elektronische Baugruppen 3-D MID e.V., editor (2004). *3D-MID Technologie, Räumliche elektronische Baugruppen*. Hanser, Munich.

[French et al., 2006] French, O., Hopcraft, K., and Jakeman, E. (2006). Perturbation on the perfect lens: the near-perfect lens. *New Journal of Physics*, 8(271):1–12.

[Gaillot et al., 2008] Gaillot, D. P., Croenne, C., and Lippens, D. (2008). An all-dielectric route for terahertz cloaking. *Optics Express*, 16(6):3986.

[Grbic and Eleftheriades, 2005a] Grbic, A. and Eleftheriades, G. V. (2005a). An isotropic three-dimensional negative-refractive-index transmission-line metamaterial. *J. Appl. Physics*, 98:043106–1–043106–5.

[Grbic and Eleftheriades, 2005b] Grbic, A. and Eleftheriades, G. V. (2005b). Practical limitations of subwavelength resolution using negative-refractive-index transmission-line lenses. *IEEE Trans. Microwave Theory Techn.*, 53:3201.

[Gupta and Caloz, 2007] Gupta, S. and Caloz, C. (2007). Dark and bright solitons in left-handed nonlinear transmission line metamaterials. *IEEE MTT-S Int. Microwave Symp Dig*, pages 979–982.

[Hoefer et al., 2005] Hoefer, W., So, P., Thompson, D., and Tentzeris, M. (2005). Topology and design of wide-band 3D metamaterials made of periodically loaded transmission lines. *2005 Int. Microwave Symposium Digest, Long Beach*, pages 1443–1446.

[Hoefer, 1989] Hoefer, W. J. R. (1989). The transmission line matrix (TLM) method. In Itoh, T., editor, *Numerical Techniques for Microwave and Millimeter Wave Passive Structures*, pages 496–591. Wiley, New York.

[Hoefer and So, 2003] Hoefer, W. J. R. and So, P. (2003). A time-domain virtual electromagnetics laboratory for microwave engineering education. *IEEE Trans. Microw. Theory Tech.*, 51:1318–1325.

[Hofmann et al., 2008] Hofmann, P., Zedler, M., and Russer, P. (2008). Dekomposition dreidimensionaler Metamaterialien in Polyeder und Verfahren zu deren Herstellung. Patent filed.

[Ishimaru, 1991] Ishimaru, A. (1991). *Electromagnetic Wave Propagation, Radiation, and Scattering*. Prentice Hall.

[Islam and Eleftheriades, 2004] Islam, R. and Eleftheriades, G. V. (2004). Phase-agile branch-line couplers using metamaterial line. *IEEE Microw. Compon. Lett*, 14(7):340.

[Itoh, 1989] Itoh, T. (1989). *Numerical Techniques for Microwave and Millimeter-Wave Passive Structures*. Wiley.

[Iyer and Eleftheriades, 2002] Iyer, A. K. and Eleftheriades, G. V. (2002). Negative refractive index metamaterials supporting 2-d waves. *IEEE MTT-S Int. Microwave Symp Dig*, 2:1067.

[Iyer and Eleftheriades, 2006] Iyer, A. K. and Eleftheriades, G. V. (2006). A volumetric layered transmission-line metamaterial exhibiting a negative refractive index. *Journal of the Optical Society of America (JOSA-B)*, 23:553.

[Iyer and Eleftheriades, 2008] Iyer, A. K. and Eleftheriades, G. V. (2008). Mechanism of subdiffraction free-space imaging using transmission-line metamaterial superlens: An experimental verification. *Appl. Phys. Lett.*, 92:131105.

[Joannopoulos et al., 1995] Joannopoulos, J. D., Meade, R. D., and Winn, J. N. (1995). *Photonic Crystals – Molding the Flow of Light*. Princeton.

[Johns, 1987] Johns, P. B. (1987). A symmetrical condensed node for the tlm method. *IEEE Trans. Microwave Theory Techn.*, 35:370–377.

[Kildal et al., 2007] Kildal, P. S., Kishk, A., and Sipus, Z. (2007). RF invisibility using metamaterials: Harry Potter's cloak or the emperor's new clothes. *2007 Int. Antennas and Propagation Society Symposium Digest*.

[Koschny et al., 2005] Koschny, T., Zhang, L., and Soukoulis, C. M. (2005). Isotropic three-dimensional left-handed metamaterials. *Physical Review B*, 71:121103–1–121103–4.

[Kron, 1943] Kron, G. (1943). Equivalent circuits to represent the electromagnetic field equations. *Physical Review*, 64(3):126–128.

[Krumpholz and Russer, 1994] Krumpholz, M. and Russer, P. (1994). On the dispersion in TLM and FDTD. *IEEE Trans. Microwave Theory Techn.*, 42(7):1275–1279.

[Landau et al., 1984] Landau, L. D., Lifshitz, E. M., and Pitaevskii, L. P. (1984). *Electrodynamics of Continuous Media*. Butterworth-Heinemann, 2 edition.

[Lim et al., 2005] Lim, S., Caloz, C., and Itoh, T. (2005). Metamaterial-based electronically-controlled transmission line structure as a novel leaky-wave antenna with tunable radiation angle and beamwidth. *IEEE Trans. Microw. Theory Tech.*, 53(1):161.

[LPKF Laser & Electronics AG, 2008] LPKF Laser & Electronics AG (2008). LDS process description. Technical report, http://www.lpkfusa.com/datasheets/mid/lds.pdf.

[Mandelshtam, 1947] Mandelshtam, L. I. (1947). Polnoe sobranie trudov v. 2,5. *Akademiia nauk SSSR*.

[Marqués et al., 2008] Marqués, R., Martín, F., and Sorolla, M. (2008). *Metamaterials with Negative Parameters: Theory, Design, and Microwave Applications*. Wiley.

[Maslovski et al., 2004] Maslovski, S., Tretyakov, S., and Alitalo, P. (2004). Near-field enhancement and imaging in double planar polariton-resonant structures. *J. Appl. Physics*, 96(3):1293.

[Matthaei et al., 1980] Matthaei, G., Young, L., and Jones, E. M. T. (1980). *Microwave Filters, Impedance-Matching Networks, and Coupling Structures*. Artech House.

[Mercure et al., 2005] Mercure, P. K., Haley, R. P., Bogle, A., and Kempel, L. (2005). Three-dimensional isotropic meta-materials. *2005 Int. Antennas and Propagation Society Symposium Digest*, pages 623–626.

[Möbius et al., 2008] Möbius, A., Elbick, D., Weidlich, E. R., Feldmann, K., Schüßler, F., Borris, J., Thomas, M., Zänker, A., and Klages, C. P. (2008). Plasma-printing and galvanic metallization hand in hand – a new technology for the cost-efficient manufacture of flexible printed circuits. *Electrochimica Special Issue of the Euro-Interfinish 2007, Athens*, page accepted for publication.

[Munk, 2000] Munk, B. (2000). *Frequency Selective Surfaces*. Wiley.

[Murphy, 2002] Murphy, K. (2002). Development of integrated electrical and mechanical assemblies using two shot moulding and selective metallization technique. *5. International Congress Molded Interconnect Devices*, pages 35–39.

[Oliner, 2002] Oliner, A. A. (2002). A periodic-structure negative-refractive-index medium without resonant elements. *USNC/URSI Nat. Radio Science Meeting*, page 41.

[Oppenheim and Schäfer, 1999] Oppenheim, A. V. and Schäfer, R. W. (1999). *Discrete Time Signal Processing*. Prentice Hall, 2 edition.

[Padilla, 2007] Padilla, W. J. (2007). Group theoretical description of artificial electromagnetic metamaterials. *Optics Express*, 15(4):1639–1646.

[Pein et al., 2004] Pein, C., Eberhardt, W., and Kück, H. (2004). Process optimization for hot embossing. *6. International Congress Molded Interconnect Devices*, pages 241–245.

[Pendry, 2000] Pendry, J. B. (2000). Negative refraction makes a perfect lens. *Phys. Rev. Lett.*, 85:3966–3969.

[Pendry, 2004] Pendry, J. B. (2004). A chiral route to negative refraction. *Science*, 306:1353.

[Pendry et al., 2006] Pendry, J. B., Schurig, D., and Smith, D. R. (2006). Controlling electromagnetic fields. *Science*, 312:1780–1782.

[Pozar, 2005] Pozar, D. M. (2005). *Microwave Engineering*. Wiley, 3 edition.

[Russer et al., 2007] Russer, J. A., Sumant, P. S., and Cangellaris, A. C. (2007). A Lagrangian approach for the handling of curved boundaries in the finite difference time-domain method. *IEEE MTT-S Int. Microwave Symp Dig*, pages 717–720.

[Russer, 1994] Russer, P. (1994). Evaluation of the S-matrix of microwave circuits with general topology. *Archiv für Elektronik und Übertragungstechnik*, 48:347.

[Russer, 1996] Russer, P. (1996). The alternating rotated transmission line matrix (ARTLM) scheme. *Electromagnetics*, 16(5):537–551.

[Russer, 2006] Russer, P. (2006). *Electromagnetics, Microwave Circuit and Antenna Design for Communications Engineering*. Artech House, Boston, 2nd edition.

[Salandrino and Engheta, 2006] Salandrino, A. and Engheta, N. (2006). Far-field subdiffraction optical microscopy using metamaterial crystals: Theory and simulations. *Phys. Rev. B*, 74:075103.

[Sanada et al., 2003] Sanada, A., Caloz, C., and Itoh, T. (2003). Zeroth-order resonance in composite right/left-handed transmission line resonators. *Asia-Pacific Microwave Conference*, 3:1588.

[Schurig et al., 2006] Schurig, D., Mock, J. J., Justice, B. J., Cummer, S. A., Pendry, J. B., Starr, A. F., and Smith, D. R. (2006). Metamaterial electromagnetic cloak at microwave frequencies. *Science*, 314:977–980.

[Schurig and Smith, 2004] Schurig, D. and Smith, D. R. (2004). Negative index lens aberrations. *Phys. Rev. E*, 70(6):065601.

[Schüßler, 1990] Schüßler, H. W. (1990). *Netzwerke, Signale und Systeme 1*. Springer, 3 edition.

[Schüßler et al., 2004] Schüßler, M., Frese, J., and Jakoby, R. (2004). Design of compact planar antennas using LH-transmission lines. *IEEE MTT-S Int. Microwave Symp Dig*, page 209.

[Shamonina et al., 2002] Shamonina, E., Kalinin, V. A., Ringhofer, K. H., and Solymar, L. (2002). Magnetoinductive waves in one, two, and three dimensions. *J. Appl. Physics*, 92:6252.

[Shelby et al., 2001] Shelby, R. A., Smith, D. R., and Schultz, S. (2001). Experimental verification of a negative index of refraction. *Science*, 292:77–79.

[Siddiqui and Eleftheriades, 2006] Siddiqui, O. F. and Eleftheriades, G. V. (2006). Spatial-filtering microwave devices using metallic anisotropic grids over ground. *Proc. 36th European Microwave Conference, Manchester*, page 933.

[Sievenpiper et al., 1999] Sievenpiper, D., Zhang, L., Jimenez-Broas, R., Alexópolous, N., and Yablonovitch, E. (1999). High-impedance electromagnetic surfaces with a forbidden frequency band. *IEEE Trans. Microwave Theory Techn.*, 47:2059.

[Sievenpiper et al., 2003] Sievenpiper, D. F., Schaffner, J. H., Song, H. J., Loo, R. Y., and Tangonan, G. (2003). Two-dimensional beam steering using an electrically tunable impedance surface. *IEEE Trans. Antennas Propagat.*, 51(10):2713.

[Smith et al., 2000] Smith, D. R., Padilla, W. J., Vier, D. C., Nemat-Nasser, S. C., and Schultz, S. (2000). Composite medium with simultaneously negative permeability and permittivity. *Phys. Rev. Lett.*, 84:4184–4187.

[Smith et al., 2002a] Smith, D. R., Schulz, S., Markos, P., and Soukoulis, C. M. (2002a). Determination of effective permittivity and permeability of metamaterials from reflection and transmission coefficients. *Phys. Rev. B*, 65:195104.

[Smith et al., 2002b] Smith, D. R., Schurig, D., Rosenbluth, M., Schultz, S., Ramakrishna, S. A., and Pendry, J. B. (2002b). Limitations on sub-diffraction imaging with a negative refractive index slab. *Appl. Phys. Lett.*, 82:1506.

[Smolyaninov et al., 2007] Smolyaninov, I. I., Hung, Y. J., and Davis, C. C. (2007). Magnifying superlens in the visible frequency range. *Science Magazine*, 315:1699.

[Stickel et al., 2007] Stickel, M., Elek, F., Zhu, J., and Eleftheriades, G. V. (2007). Volumetric negative-refraction-index metamaterials based upon the shunt-node transmission-line configuration. *J. Appl. Physics*, 102:094903.

[Tretyakov, 2003] Tretyakov, S. (2003). *Analytical Modeling in Applied Electromagnetics*. Artech House.

[Tretyakov et al., 2003] Tretyakov, S., Nefedov, I., Sihvola, A., Maslovski, S., and Simovski, C. (2003). Waves and energy in chiral nihility. *Journal of Electromagnetic Waves and Applications*, 17:695.

[Tsukerman, 2008] Tsukerman, I. (2008). Negative refraction and the minimum lattice cell size. *J. Opt. Soc. Am. B*, 25:927–936.

[Ueda et al., 2007] Ueda, T., Lai, A., and Itoh, T. (2007). Demonstration of negative refraction in a cutoff parallel-plate waveguide loaded with 2-d square lattice of dielectric resonators. *IEEE Trans. Microw. Theory Tech.*, 55(6):1280–1287.

[Vendik and Gashinova, 2004] Vendik, O. G. and Gashinova, M. S. (2004). Artificial double negative (DNG) media composed by two different dielectric sphere lattices embedded in a dielectric matrix. *Proc. European Microwave Conf., Amsterdam, The Netherlands*, pages 1209–1212.

[Veselago, 1968] Veselago, V. G. (1968). The electrodynamics of substances with simultaneously negative values of ϵ and μ. *Sov. Phys. Usp.*, pages 509–514.

[Veselago et al., 2006] Veselago, V. G., Braginsky, L., Shklover, V., and Hafner, C. (2006). Negative refractive index materials. *J. Computational and Theoretical Nanoscience*, 3:1–30.

[Wang et al., 2007] Wang, G., Fang, J., and Dong, X. (2007). Resolution of near-field microwave target detection and imaging by using flat LHM lens. *IEEE Trans. Antennas Propagat.*, 55(12):3534–3541.

[Ward and Pendry, 1996] Ward, A. J. and Pendry, J. B. (1996). Refraction and geometry in maxwell's equations. *Jrnl. Mod. Opt.*, 43:773–793.

[Ward and Pendry, 1998] Ward, A. J. and Pendry, J. B. (1998). Calculating photonic green's functions using a nonorthogonal finite-difference time-domain method. *Phys. Rev. B*, 58:7252–7259.

[Weitsch and Eibert, 2007] Weitsch, Y. and Eibert, T. F. (2007). A left-handed/right-handed leaky-wave antenna derived from slotted rectangular hollow waveguide. *European Microwave Conference, Munich*.

[Wlodarczyk, 1992] Wlodarczyk, A. J. (1992). Representation of symmetrical condensed TLM node. *Electronics Letters*, 28(18):1686–1687.

[Zedler et al., 2007a] Zedler, M., Caloz, C., and Russer, P. (2007a). 3D composite right-left handed metamaterials with Lorentz-type dispersive elements. *ISSSE 2007, Montréal, Canada*.

[Zedler et al., 2007b] Zedler, M., Caloz, C., and Russer, P. (2007b). A 3D isotropic left-handed metamaterial based on the rotated transmission line matrix (TLM) scheme. *IEEE Trans. Microwave Theory Tech, IMS Special Issue*, 55(12):2930–2941.

[Zedler et al., 2007c] Zedler, M., Caloz, C., and Russer, P. (2007c). Circuital and experimental demonstration of a 3D isotropic LH metamaterial based on the rotated TLM scheme. *2007 Int. Microwave Symposium Digest, Honolulu, Hawaii*, pages 1827–1830.

[Zedler et al., 2008a] Zedler, M., Hofmann, S., and Russer, P. (submitted, 2008a). Three-dimensional isotropic scalar metamaterial with Drude dispersion for the permittivity and permeability. *Appl. Phys. Lett.*

[Zedler and Russer, 2006] Zedler, M. and Russer, P. (2006). Investigation on the dispersion relation of a 3D LC-based metamaterial with an omnidirectional left-handed frequency band. *2006 Int. Microwave Symposium Digest, San Francisco*, pages 1477–1480.

[Zedler and Russer, 2007] Zedler, M. and Russer, P. (2007). Three-dimensional CRLH metamaterials for microwave applications. *Proc. of the European Microwave Association*, 3:151–162.

[Zedler and Russer, 2008] Zedler, M. and Russer, P. (2008). *Handbook of Artificial Materials*, chapter "Network Topology Derived Metamaterials: Scalar and Vectorial 3D Configurations and their Fabrication". Taylor & Francis.

[Zedler et al., 2008b] Zedler, M., Siart, U., and Russer, P. (2008b). Circuit theory unifying description for metamaterials. *Proc. URSI GA 2008, Chicago*, page accepted for publication.

[Ziolkowski and Heyman, 2001] Ziolkowski, R. W. and Heyman, E. (2001). Wave propagation in media having negative permittivity and permeability. *Phys. Rev. E*, 64:056625.

Publications by the Author

Journal Publications

1. M. Zedler, S. Hofmann, and P. Russer, "Three-dimensional isotropic scalar metamaterial with Drude dispersion for the permittivity and permeability," *Appl. Phys. Lett.*, submitted, 2008.

2. M. Zedler and P. Russer, "A three-dimensional left-handed metamaterial based on the rotated TLM method," *Proc. of SPIE*, vol. 6987, no. 58, pp. 69 871M1–69 871M14, 2008.

3. M. Zedler, C. Caloz, and P. Russer, "A 3D isotropic left-handed metamaterial based on the rotated transmission line matrix (TLM) scheme," *IEEE Trans. Microwave Theory Tech, IMS Special Issue*, vol. 55, no. 12, pp. 2930–2941, 2007.

4. M. Zedler and P. Russer, "Three-dimensional CRLH metamaterials for microwave applications," *Proc. European Microwave Association*, vol. 3, pp. 151–162, 2007.

5. M. Zedler, C. Janke, P. Haring-Bolivar, H. Kurz, and H. Künzel, "Improved coherent terahertz emission by modification of the dielectric environment," *Appl. Phys. Lett.*, vol. 83, no. 20, pp. 4196–4198, 2003.

Book Chapters

6. M. Zedler and P. Russer, *Handbook of Artificial Materials*. Taylor & Francis, 2008, ch. "Network Topology Derived Metamaterials: Scalar and Vectorial 3D Configurations and their Fabrication".

7. M. Zedler, C. Caloz, and P. Russer, *Time domain methods in modern engineering electrodynamics*. Springer, 2008, ch. "A 3D Isotropic Left-Handed Metamaterial based on the rotated TLM Scheme".

Conference Contributions

8. M. Zedler, S, Hofmann, U. Siart, and P. Russer, "Topological Description of Metamaterials," *Proc. 2nd Int. Cong. Adv. Electromagnetic Materials, Pamplona, Spain*, submitted, 2008.

9. M. Zedler, U. Siart, and P. Russer, "Circuit theory unifying description for metamaterials," *Proc. URSI GA 2008, Chicago*, accepted for publication, 2008.

10. M. Zedler and P. Russer, "Full-wave simulation of a finite 3D metamaterial slab consisting of rotated tlm metamaterial cells," *Proc. of the Metamaterials Week 2008, Barcelona*, 2008.

11. A. Culhaoglu, M. Zedler, W. Hoefer, A. Osipov, and P. Russer, "Full-wave numerical simulation of a finite 3D metamaterial lens," *Proc. ACES, Niagara Falls, Canada*, p. 989–994, 2008.

12. M. Zedler, P. So, C. Caloz, and P. Russer, "IIR approach for the efficient computation of large-scale 3D RTLM CRLH metamaterials," *Proc. ACES, Niagara Falls, Canada*, p. 978–983, 2008.

13. M. Zedler and P. Russer, "A three-dimensional left-handed metamaterial based on the rotated TLM method," *Proc. SPIE Photonics Europe, Strasbourg, France*, invited paper, 2008.

14. M. Zedler, C. Caloz, and P. Russer, "Circuital and experimental demonstration of a 3D isotropic LH metamaterial based on the rotated TLM scheme," *Time-Domain Methods in Modern Engineering Electromagnetics, Technische Universität München*, May 2007.

15. M. Zedler, C. Caloz, and P. Russer, "Numerical analysis of a planarized 3D isotropic LH metamaterial based on the rotated TLM scheme," *Proc. Eurocon, Warsaw*, pp. 24–27, 2007.

16. M. Zedler, C. Caloz, and P. Russer, "Analysis of a planarized 3D isotropic LH metamaterial based on the rotated TLM scheme," *Proc. EuMC, Munich*, 2007.

17. M. Zedler, C. Caloz, and P. Russer, "3D composite right-left handed metamaterials with lorentz-type dispersive elements," *ISSSE 2007, Montréal, Canada*, 2007.

18. M. Zedler, C. Caloz, and P. Russer, "Circuital and experimental demonstration of a 3D isotropic LH metamaterial based on the rotated TLM scheme," *2007 Int. Microwave Symposium Digest, Honolulu, Hawaii*, pp. 1827–1830, 2007.

19. M. Zedler and P. Russer, "Investigation on the dispersion relation of a 3D LC-based metamaterial with an omnidirectional left-handed frequency band," *2006 Int. Microwave Symposium Digest, San Francisco*, pp. 1477–1480, 2006.

20. Y. Kuznetsov, A. Baev, T. Shevgunov, M. Zedler, and P. Russer, "Transfer function representation of passive electromagnetic structures," *2005 Int. Microwave Symposium Digest, Long Beach*, pp. 183–186, 2005.

21. M. Zedler and P. Russer, "UC-PBG antenna on thick dielectric substrate," *18th General Assembly of the URSI*, 2005.

22. C. Janke, M. Zedler, P. Haring-Bolivar, and H. Kurz, "Improved coherent terahertz emission by modification of the dielectric environment," *Proc. Quantum Electronics and Laser Science QELS*, p. QWB5, 2004.

Workshop Contributions

23. M. Zedler and P. Russer, "3D LH metamaterials based on rotated TLM cells," *IMS Workshop on Metamaterials*, 2008.

24. M. Zedler, C. Caloz, and P. Russer, "Fundamental structures of two- and three-dimensional metamaterials," *IMS Workshop on Metamaterials*, 2007.

25. P. Russer and M. Zedler, "Three-dimensional metamaterials," *Proc. IV. Int. Workshop on Electromagnetic Wave Scattering, Gezbe, Turkey*, 2006.

Patents

26. P. Hofmann, M. Zedler, and P. Russer, "Dekomposition dreidimensionaler Metamaterialien in Polyeder und Verfahren zu deren Herstellung," Patent filed, 2008.

27. M. Zedler and P. Russer, "Planares dreidimensionales Metamaterial," Patent filed, 2007.

28. M. Zedler and P. Russer, "Base unit and device for the transfer of electromagnetic fields," Patent wo 2007/073716A1, 2007.

Curriculum Vitae

Personal Data

Name	Michael Zedler
E-mail	michael.zedler@mytum.de
Place and date of birth	Cologne, Germany on June 1st, 1976
Maritial status	single
Nationality	German

Education

10/2008 –	Post-Doc fellow at Dept. of Electrical and Computer Engineering, University of Toronto, Canada
08/2006 – 12/2006	Visiting research assistant at PolyGrames institute, École Polytechnique de Montréal, Quebec, Canada
06/2002 – 09/2008	Research assistant at Dept. of RF Engineering, TU München, Germany, leading to the present thesis
10/1996 – 03/2002	Diplom (Master) studies in Electrical Engineering at RWTH Aachen, Germany. *Thesis title:* "Fabrication and time-domain characterisation of photonic crystals operating in the THz frequency regime"
10/1997 – 09/1999	Additional studies in Physics at RWTH Aachen, leading to the Vordiplom (≈ Bachelor) in Physics
06/1995 – 06/1996	Military service in telecommunications division
08/1985 – 06/1995	Gymnasium Rodenkirchen, Cologne, Germany Graduating with Abitur (German A-levels)

Honours

07/2007	Winner of the 4th prize at the *Best Student Paper Competition* at the International Microwave Symposium, Honolulu, Hawaii